

NUMERICAL METHODS FOR NONLINEAR WAVE PROPAGATION IN ULTRASOUND

by

Gianmarco F. Pinton

Department of Biomedical Engineering
Duke University

Date: _____

Approved:

Gregg E. Trahey, Ph.D., Supervisor

Kathryn R. Nightingale, Ph.D.

John Trangenstein, Ph.D.

Craig Henriquez, Ph.D.

Salim Idriss, M.D., Ph.D.

Dissertation submitted in partial fulfillment of the
requirements for the degree of Doctor of Philosophy
in the Department of Biomedical Engineering
in the Graduate School of
Duke University

2007

ABSTRACT

NUMERICAL METHODS FOR NONLINEAR WAVE
PROPAGATION IN ULTRASOUND

by

Gianmarco F. Pinton

Department of Biomedical Engineering
Duke University

Date: _____

Approved:

Gregg E. Trahey, Ph.D., Supervisor

Kathryn R. Nightingale, Ph.D.

John Trangenstein, Ph.D.

Craig Henriquez, Ph.D.

Salim Idriss, M.D., Ph.D.

An abstract of a dissertation submitted in partial fulfillment of the
requirements for the degree of Doctor of Philosophy
in the Department of Biomedical Engineering
in the Graduate School of
Duke University

2007

Copyright © 2007 by Gianmarco F. Pinton
All rights reserved

Abstract

The intensities associated with the propagation of diagnostic and therapeutic ultrasound pulses are large enough to require a nonlinear description. As a nonlinear wave propagates it distorts, creating harmonics and eventually acoustic shocks. Harmonics can be used to generate images with improved spatial resolution and less clutter. The energy from nonlinear waves is deposited in a different way than in the linear case which modifies predictions for *in situ* acoustic exposure. Tissue heating and radiation force depend on this intensity. High intensity shock waves are essential for stone comminution with lithotripsy because it depends on the shear gradients caused by the pressure differentials and on the peak negative pressures for cavitation. The work presented in this dissertation investigates numerical simulations that solve nonlinear ultrasonic wave propagation in both the strongly nonlinear regime, where shocks develop, and the weakly nonlinear regime, where the acoustic attenuation prevents the formation of pressure discontinuities.

The Rankine-Hugoniot relation for shock wave propagation describes the shock speed of a nonlinear wave. This dissertation investigates time domain numerical methods that solve the nonlinear parabolic wave equation, or the Khokhlov-Zabolotskaya-Kuznetsov (KZK) equation, and the conditions they require to satisfy the Rankine-Hugoniot relation. Two numerical methods commonly used in hyperbolic conservation laws are adapted to solve the KZK equation: Godunov's method and the monotonic upwind scheme for conservation laws (MUSCL). It is shown that they satisfy the Rankine-Hugoniot relation regardless of attenuation. These two methods are compared with the current implicit solution based method. When the attenuation is small, such as in water, the current method requires a degree of grid refinement that is computationally impractical. All three numerical methods are compared in

simulations for lithotripters and high intensity focused ultrasound (HIFU) where the attenuation is small compared to the nonlinearity because much of the propagation occurs in water. The simulations are performed on grid sizes that are consistent with present-day computational resources but are not sufficiently refined for the current method to satisfy the Rankine-Hugoniot condition. It is shown that satisfying the Rankine-Hugoniot conditions has a significant impact on metrics relevant to lithotripsy (such as peak pressures), and HIFU (intensity). Because the Godunov and MUSCL schemes satisfy the Rankine-Hugoniot conditions on coarse grids they are particularly advantageous for three dimensional simulations.

The propagation of focused and intense ultrasound beams is determined by nonlinearity, diffraction, and absorption. Most descriptions of nonlinear wave propagation in ultrasound, such as the KZK equation, rely on quadratic nonlinearity. At diagnostic and some therapeutic amplitudes the quadratic, or B/A , term dominates the nonlinear term. However, when the amplitudes are sufficiently large, such as in shock wave lithotripsy, the cubic, or C/A , term becomes significant. Conventionally the parabolic wave equation has only included the quadratic terms. This dissertation establishes a time domain numerical method that solves the parabolic wave equation with cubic nonlinearity in an attenuating medium. The differences between solutions of the quadratic and cubic equations for a focused lithotripter in a water bath are investigated.

A study of numerical solutions to the linear full-wave equation and the KZK or parabolic wave equation is presented. Finite difference time domain methods are used to calculate the acoustic field emitted from a diagnostic ultrasound transducer. Results are compared to Field II, a simulation package that has been used extensively to linearly model transducers in ultrasound. The simulation of the parabolic equation can accurately predict the lateral beamplot for large F-numbers but exhibits errors

for small F-numbers. It also overestimates the depth at which the focus occurs. It is shown that the finite difference solution of the full-wave equation is accurate for small and large F-numbers. The lateral beamplots and axial intensities are in excellent agreement with the Field II simulations. For these reasons the KZK equation is abandoned in favor of the full-wave equation to describe nonlinear propagation for ultrasound imaging.

A full-wave equation that describes nonlinear propagation in a heterogeneous attenuating medium is solved numerically with finite differences in the time domain (FDTD). Three dimensional solutions of the equation are verified with water tank measurements of a commercial diagnostic ultrasound transducer and are shown to be in excellent agreement in terms of the fundamental and harmonic acoustic fields, and the power spectrum at the focus. The linear and nonlinear components of the algorithm are also verified independently. In the linear non-attenuating regime solutions match simulations from Field II to within 0.3 dB. Nonlinear plane wave propagation is shown to closely match results from the Galerkin method up to four times the fundamental frequency. In addition to thermoviscous attenuation we present a numerical solution of the relaxation attenuation laws that allows modeling of arbitrary frequency dependent attenuation, such as that observed in tissue. A perfectly matched layer (PML) is implemented at the boundaries with a novel numerical implementation that allows the PML to be used with high order discretizations. A -78 dB reduction in the reflected amplitude is demonstrated. The numerical algorithm is used to simulate a diagnostic ultrasound pulse propagating through a histologically measured representation of human abdominal wall with spatial variation in the speed of sound, attenuation, nonlinearity, and density. An ultrasound image is created in silico using the same physical and algorithmic process used in an ultrasound scanner: a series of pulses are transmitted through heterogeneous scattering tissue and

the received echoes are used in a delay-and-sum beamforming algorithm to generate images. The resulting harmonic image exhibits characteristic improvement in lesion boundary definition and contrast when compared to the fundamental image. We demonstrate a mechanism of harmonic image quality improvement by showing that the harmonic point spread function is less sensitive to reverberation clutter.

Numerical solutions of the nonlinear full-wave equation in a heterogeneous attenuating medium are used to simulate the propagation of diagnostic ultrasound pulses through a measured representation of the human abdomen with heterogeneities in speed of sound, attenuation, density, and nonlinearity. Conventional delay-and-sum beamforming is used to generate point spread functions (PSF) from a point target located at the focus. These PSFs reveal that, for the particular imaging system considered, the primary source of degradation in fundamental imaging is due to reverberation from near-field structures. Compared to the harmonic PSF the mean magnitude of the reverberation clutter in the fundamental PSF is 26 dB higher. An artificial medium with uniform velocity but unchanged impedance characteristics is used to show that for the fundamental PSF the primary source of degradation is phase aberration. Ultrasound images are created *in silico* and these beamformed images are compared to images obtained from convolution of the PSF with a scatterer field to demonstrate that a very large portion of the PSF must be used to accurately represent the clutter observed in conventional imaging.

Conventional delay-and-sum beamforming is used to generate images of an anechoic lesion located beneath the abdominal layer for various transducer configurations. Point spread functions (PSF) and estimates of the contrast to noise ratio (CNR) are used to quantify and determine the sources of improvement between harmonic and fundamental imaging. Simulations indicate that reducing the pressure amplitude at the transducer surface has no discernible effect on image quality. It is

shown that when the aperture is reduced there is an increase in the image degradation due to reverberation clutter in the fundamental and an increase in the effects of reverberation and phase aberration in the harmonic. A doubling of the transmit frequency shows that the harmonic lesion CNR becomes worse than the fundamental CNR due to increases in pulse lengthening and phase aberration.

Acoustic Radiation Force Impulse (ARFI) imaging uses brief, high intensity, focused ultrasound pulses to generate a radiation force that displaces tissue. Nonlinear propagation of acoustic pulses transfers energy to higher frequencies where it is preferentially absorbed by tissue. The radiation force is proportional to the absorbed energy. This dissertation examines the effects of nonlinearity on the displacements induced by radiation force with various ultrasound transducer configurations. A three dimensional numerical method that simulates nonlinear acoustic propagation is used to calculate the intensity and absorption losses for typical ARFI pulses. It is demonstrated that nonlinearity has a relatively small effect on the intensity but increases estimates of the loss by up to a factor of 20. The intensity fields obtained from the acoustic simulations are used as an input to a finite element method (FEM) model of the mechanical tissue response to a radiation force excitation. These simulations show that including nonlinearity in the acoustic intensity significantly reduces predictions of the displacement without having a significant impact on the lateral and elevation resolution.

Acknowledgements

I would like to thank Dr. Gregg Trahey for being a superb advisor and for his unflagging support of my research. I would also like to thank Dr. John Trangenstein for always supplying new ideas and paths to explore. I thank the other members of my dissertation committee for their thoughtful insights and guidance throughout my graduate studies.

My thesis work was greatly enhanced by the insights and efforts of my fellow students, especially Jeremy Dahl and Mark Palmeri. The models developed throughout this thesis presented considerable computational challenges that would not have been overcome without the technical assistance of Joshua Baker-LePain.

Most importantly, none of this would have been possible without the support of my family.

Contents

Abstract	iv
Acknowledgements	ix
List of Tables	xvi
List of Figures	xvii
Glossary of Symbols	xxiii
1 Background	1
1.0.1 Clinical Motivation	1
1.0.2 Physical motivation and B/A	4
1.0.3 Imaging with a Nonlinear Beam	5
1.0.4 Burgers Equation	7
1.0.5 Propagation of Discontinuities	11
1.0.6 KZK equation	11
1.0.7 Absorption	13
2 Numerical solutions of the Khokhlov-Zabolotskaya-Kuznetsov equation satisfying the Rankine-Hugoniot condition	15
2.1 Introduction	15
2.2 Basic equations	17
2.2.1 KZK equation	17
2.2.2 Rankine-Hugoniot condition	19
2.3 Numerical methods	19
2.3.1 Implicit solution based method	20

2.3.2	Godunov’s method	21
2.3.3	MUSCL scheme	22
2.3.4	Diffraction	22
2.3.5	Absorption	22
2.3.6	Computational requirements	24
2.4	Results	24
2.4.1	Solutions of the inviscid Burgers’ equation	24
2.4.2	Solutions of the viscid Burgers’ equation	26
2.4.3	Lithotripsy	28
2.4.4	HIFU	31
2.5	Summary and Conclusions	34
2.6	Acknowledgments	36
3	Numerical solution of the parabolic wave equation with cubic nonlinearity	37
3.1	Introduction	37
3.2	Model Description	38
3.2.1	Acoustic Equation	38
3.2.2	Numerical Method	40
3.3	Results	43
3.4	Conclusions	46
3.5	Acknowledgments	47
4	A comparison of time domain solutions for the full-wave equation and the parabolic wave equation for diagnostic ultrasound transducers	48
4.1	Introduction	48

4.2	Equations	49
4.3	Methods	50
4.4	Results	53
4.5	Conclusion	58
4.6	Acknowledgments	59
5	A heterogeneous nonlinear attenuating full-wave model of ultrasound	60
5.1	Introduction	60
5.2	Methods	63
5.2.1	Acoustic Equation	63
5.2.2	Diffraction	64
5.2.3	Temporal terms and density	66
5.2.4	Relaxation mechanisms	67
5.2.5	Perfectly matched layer	68
5.2.6	Hydrophone measurements	71
5.2.7	Field II	71
5.3	Results	73
5.3.1	Stencil parameters	73
5.3.2	Relaxation mechanisms	73
5.3.3	Perfectly matched layers	74
5.3.4	Clinical transducer in a linear homogeneous non-attenuating medium	76
5.3.5	Nonlinear plane wave	79
5.3.6	Experimental verification	80
5.3.7	Ultrasonic imaging	84

5.4	Discussion	88
5.4.1	Computation	88
5.4.2	Perfectly matched layer	89
5.4.3	Nonlinear plane wave	90
5.4.4	Experimental verification	90
5.4.5	Ultrasonic Imaging	91
5.5	Summary and Conclusions	93
5.6	Acknowledgments	94
6	Sources of image degradation in fundamental and harmonic ultrasound imaging	95
6.1	Introduction	95
6.2	Methods and Results	99
6.2.1	Backscatter	100
6.2.2	Heterogeneous propagation	101
6.2.3	Point spread functions	103
6.2.4	Ultrasonic Imaging	108
6.3	Discussion	111
6.3.1	Point source brightness	111
6.3.2	Sources of PSF degradation	112
6.3.3	Reverberation clutter	112
6.3.4	Phase aberration	113
6.3.5	Validity of convolution	114
6.4	Summary and Conclusions	114
6.5	Acknowledgments	115

7	Numerical nonlinear ultrasonic imaging in heterogeneous media	116
7.1	Introduction	116
7.2	Methods	119
7.3	Results	122
7.4	Discussion	130
7.5	Conclusion	131
7.6	Acknowledgments	131
8	The effects of nonlinearity on displacements induced by acoustic radiation force in tissue	132
8.1	Introduction	132
8.2	Methods	134
8.3	Results	136
8.3.1	Acoustic simulations	136
8.3.2	FEM model	142
8.4	Discussion	145
8.5	Conclusion	146
8.6	Acknowledgments	147
9	Conclusions and Future Work	148
9.1	Conclusions	148
9.2	Future Work	151
9.2.1	Three dimensional PSFs	151
9.2.2	Effect of scatterer brightness and non-Rayleigh distribution	151
9.2.3	The effects of nonlinearity on tissue heating	151
A	Derivation of B/A	152

B Derivation of the KZK equation	154
C Cole-Hopf Transformation	156
D Spectral methods	157
E Kramers-Krönig Relation	159
Bibliography	160
Biography	171

List of Tables

1.1	Typical B/A and attenuation values.	5
1.2	Plane wave shock propagation distances in liver	10
2.1	A comparison of the lithotripter peak pressures.	29
5.1	Relaxation parameters	74
5.2	Conductivity profiles	75
5.3	Acoustic parameters for tissue	85
6.1	Acoustic parameters for tissue	102
6.2	Mean dB values for three regions of PSFs	105
6.3	CNR for varying PSF kernel size	110
7.1	Typical acoustic parameters for tissue	122
7.2	Contrast to noise ratios for images of the anechoic lesion.	124
7.3	Mean dB values for three regions of PSFs	127

List of Figures

1.1	Harmonic imaging demonstrates increased visibility of septation and a mural nodule within the cyst when compared to the noisier fundamental image.	3
1.2	Time sequence illustrating the nonlinear propagation of a wave. . . .	6
1.3	A schematic of the relative intensity of the fundamental and harmonic components as they propagate through tissue.	6
1.4	Plane wave shock formation described by Burgers' equation.	9
2.1	A comparison of the analytic solution of the inviscid Burgers' equation to the numerical solutions in one spatial dimension. Godunov's method and the MUSCL scheme satisfy the Rankine-Hugoniot condition whereas the implicit solution based method does not, in this case.	26
2.2	Number of grid points required to correctly predict the shock wave speed as a function of attenuation.	27
2.3	Nondimensionalized pressure at the focus for numerical solutions of the KZK equation with implicit based, Godunov, and MUSCL schemes.	29
2.4	Peak positive and peak negative nondimensionalized pressure as a function of depth.	30
2.5	Nondimensionalized HIFU pressure at the focus for numerical solutions of the KZK equation for propagation in water from a circular transducer.	31
2.6	Nondimensionalized I_{SPTA} intensity as a function of depth for propagation in water from a circular transducer.	32
2.7	Nondimensionalized HIFU pressure at the focus for numerical solutions of the KZK equation with stationary and Rankine-Hugoniot shock speeds. Propagation is in tissue from a rectangular transducer.	33
2.8	Nondimensionalized intensity as a function of depth for propagation in tissue from a rectangular transducer.	34

3.1	Nondimensionalized pressure at the focus for numerical solutions of the parabolic wave equation with quadratic and cubic nonlinearity.	44
3.2	Peak positive nondimensionalized pressure as a function of depth for quadratic and cubic nonlinearity.	45
3.3	Peak positive nondimensionalized pressure as a function of grid refinement for quadratic and cubic nonlinearity.	46
4.1	Lateral contour plots for simulations of a diagnostic ultrasound transducer with an $f/1.5$ using Field II (left), finite differences applied to the full-wave equation (center), and finite differences applied to the parabolic wave equation (right). The slice is at the center of the elevation plane	54
4.2	The normalized axial intensity for simulations of a diagnostic ultrasound transducer with an $f/1.5$ using Field II (solid), finite differences applied to the full-wave equation (dash-dotted), and finite differences applied to the parabolic wave equation (dashed).	55
4.3	The lateral beamplot for simulations of a diagnostic ultrasound transducer with an $f/1.5$ taken at the center of the elevation plane.	56
4.4	The lateral beamplot for simulations of a diagnostic ultrasound transducer with an $f/5$ taken at the center of the elevation plane.	57
4.5	The normalized axial intensity for simulations of a diagnostic ultrasound transducer with an $f/5$	58
5.1	Directions of the stencil for the linear wave equation in the positive quadrant.	65
5.2	Relaxation model for frequency dependent attenuation laws in tissue and water. A two parameter model is sufficient to closely fit the attenuation laws across a wide frequency range.	74
5.3	Transmitted and reflected waves from the perfectly matched layer with 100 layers (or a 1.25 mm thickness).	75
5.4	A comparison of the intensity of the acoustic field as calculated by Field II and the linear inviscid FDTD nonlinear full-wave method for a commercial clinical ultrasound transducer. The lateral plane is shown.	77

5.5	A comparison of the lateral beamplot at the focus for the Field II and the linear inviscid nonlinear full-wave simulations.	78
5.6	A comparison of the axial intensity for the Field II and the linear inviscid nonlinear full-wave simulations.	78
5.7	Nonlinear propagation of a plane wave as calculated by the FDTD nonlinear full-wave algorithm and the Galerkin scheme. A time domain waveform is shown on the left and the power spectrum is shown on the right.	80
5.8	Experimental and simulated PSFs for the fundamental and harmonic beams.	82
5.9	A comparison of measured and simulated lateral and elevation beamplots for the fundamental and harmonic PSFs shown in Fig. 5.8. . . .	83
5.10	A comparison of the experimental and simulated power spectrum at the focus.	84
5.11	On the left, a graphical representation of the variation in the speed of sound for the abdominal layer (not shown are spatial variations in attenuation, nonlinearity, and density). On the right, the acoustic field of a diagnostic pulse at the focus.	85
5.12	Simulated fundamental and harmonic ultrasound images of an anechoic region below an abdominal using a transmit-receive beamformation process.	86
5.13	Point spread functions with clutter from propagation through a representation of the abdominal wall. The fundamental and harmonic PSFs are shown without any processing and with reverberation clutter removed.	88
6.1	A comparison of the theoretical and simulated power spectrum of the backscatter from a field of randomly distributed scatterers in the Rayleigh regime.	101
6.2	On the left, a graphical representation of the variation in the speed of sound for the abdominal layer (not shown are spatial variations in attenuation, nonlinearity, and density). On the right, the acoustic field of a diagnostic pulse at the focus.	102

6.3	Transmit receive PSFs from an unapodized transducer in a homogeneous medium. The fundamental and harmonic PSFs are shown normalized relative to their peak.	103
6.4	Point spread functions with clutter from propagation through a representation of the abdominal wall. The fundamental and harmonic PSFs are shown.	104
6.5	Point spread functions of the reverberation clutter from propagation through a representation of the abdominal wall. The fundamental and harmonic PSFs are shown without any signal from a point target. . .	106
6.6	Point spread functions without reverberation clutter obtained by subtracted the reverberation clutter PSF (Fig. 6.5) from the abdominal PSF (Fig. 6.4).	107
6.7	Point spread functions without aberration obtained propagating the ultrasonic pulse through a medium with no variations in the speed of sound but with an unchanged impedance compared to the abdominal layer.	108
6.8	Simulated fundamental and harmonic ultrasound images of a 5 mm anechoic lesion at 5 cm below an abdominal layer using transmit-receive beamforming.	109
6.9	Ultrasonic images of a 5 mm circular anechoic lesion obtained with linear convolution theory for varying fundamental PSF sizes.	110
6.10	Radial integration of the fundamental and harmonic abdominal PSFs.	111
7.1	Map of the speed of sound and a propagating ultrasonic pulse.	122
7.2	Map of the speed of sound, fundamental, and harmonic images.	123
7.3	Fundamental and harmonic images for 0.2 MPa, F/1, 2.1 MHz.	124
7.4	Fundamental and harmonic images for 3 MPa, F/3, 2.1 MHz.	125
7.5	Fundamental and harmonic images for 1 MPa, F/1, 4.2 MHz	126
7.6	Fundamental and harmonic point spread functions for 3 MPa, F/3, 2.1 MHz.	127

7.7	Fundamental and harmonic point spread functions for 3 MPa, F/3, 2.1 MHz.	128
7.8	Fundamental and harmonic point spread functions for 3 MPa, F/3, 2.1 MHz.	129
7.9	Fundamental and harmonic point spread functions for 3 MPa, F/3, 2.1 MHz.	129
8.1	Normalized intensity in the lateral axial plane for the ARFI control, the surface pressure reduced by a factor of 3.5 to 1 MPa, a linear medium, and an F/3 configuration instead of F/2.	137
8.2	Normalized loss calculated as the intensity of the absorbed acoustic pressure in the lateral axial plane for the ARFI control, the surface pressure reduced by a factor of 3.5 to 1 MPa, a linear medium, and an F/3 configuration instead of F/2.	139
8.3	Relative intensity and loss intensity for the control (3.5 MPa), the reduced intensity (1 MPa), and linear propagation (N=0) along the axis calculated from pressures normalized by values at the transducer face.	140
8.4	Relative intensity and loss intensity for the linear propagation along the axis calculated from pressures normalized by values at the transducer face. As predicted by theory, the curves are scaled versions of each other.	141
8.5	Relative intensity and loss intensity for the control (F/2) and the decreased aperture (F/3) along the axis calculated from pressures normalized by values at the transducer face.	142
8.6	The axial displacement profiles over the 3D quarter symmetry model, 1.2 ms after the cessation of the radiation force excitation as calculated from the linear and nonlinear acoustic intensities.	143
8.7	The axial displacement profiles in the center of the region of excitation for the linear ($\beta = 0$) and nonlinear ($\beta = 5$) control acoustic intensity fields.	144

8.8	Normalized lateral and elevation displacement profiles at the focal depth for the linear ($\beta = 0$) and nonlinear ($\beta = 5$) control acoustic intensity fields.	145
-----	---	-----

Glossary of Symbols

A	= nondimensional attenuation parameter
B/A	= parameter of nonlinearity
c	= speed of sound
c_0	= small signal speed of sound
d	= characteristic distance
f	= frequency
G	= nondimensional focusing parameter
k	= wave number
N	= nondimensional coefficient of nonlinearity
P	= total pressure
P_0	= ambient pressure
p	= $P - P_0$ acoustic pressure
p_0	= amplitude of p
R	= nondimensional transverse coordinate (radial)
t	= time
t'	= retarded time
u	= particle velocity component
X	= nondimensional transverse coordinate (Cartesian)
Y	= nondimensional transverse coordinate (Cartesian)
\bar{z}	= shock formation distance for a plane wave

α	= absorption coefficient (nepers per unit distance)
β	= coefficient of nonlinearity, $1+B/2A$
γ	= Rankine Hugoniot shock speed
Γ	= $\beta\varepsilon k/\alpha$, Gol'dberg number
ε	= u_0/c_0 , the acoustic Mach number
λ	= $\Delta\sigma\Delta\tau/(4G\Delta R^2)$
ρ	= mass density
ρ'	= ambient density
σ	= dimensionless propagation distance
τ	= nondimensional retarded time
ν	= power of absorption law
ω	= angular frequency
<hr/>	
∇_{\perp}	= transverse Laplacian

Chapter 1

Background

The propagation of ultrasonic waves is nonlinear. Linear assumptions do not always predict observations made with the intensities associated with diagnostic ultrasound scanners. As a wave propagates forward it distorts; creating harmonics and eventually acoustic shocks. Harmonics can be used to generate images with improved spatial resolution and less clutter.

The energy from nonlinear waves is deposited in a different way than in the linear case which modifies predictions for *in situ* acoustic exposure. Tissue heating and radiation force depend on this intensity. High intensity shock waves are essential for stone comminution with lithotripsy because it depends on the shear gradients caused by the pressure differentials and on the peak negative pressures for cavitation.

This background chapter outlines the clinical and physical motivation for nonlinear acoustics. Then the fundamentals of nonlinear wave and beam propagation are summarized. Current numerical models for nonlinear beams are described.

1.0.1 Clinical Motivation

Tissue Harmonic Imaging (THI) markedly improves image quality [59, 110, 116]. The most dramatic differences between harmonic and linear images are visible in abdominal[23], pelvic[37], and cardiac sonography [66] where clinical papers enthusiastically report improvements in lateral and axial resolution, contrast-to-noise ratio, clutter rejection, increased penetration, lesion visibility and diagnostic confidence. In the past decade practically all commercial diagnostic ultrasound manufacturers have

implemented THI on their scanners. The aims of nonlinear wave modeling include determining which of these claims are substantiated by the ultrasonic beam characteristics, to understand the mechanisms for image improvement, and to use the models to construct better beams.

A study of endocardial border definition by Kornbluth *et al.* [66] reports a visualization improvement in 64% of the images when compared to fundamental imaging with 26% improving from poor/not seen to good/excellent. Harmonic imaging has a similarly significant impact on wall motion scoring and visualization of both normal and abnormal cardiac structures (such as valve chordae and papillary muscles).

In abdominal scanning, harmonic imaging is reported to be better than conventional ultrasound in regard to lesion visibility and diagnostic confidence, especially in patients with a high body mass index (> 30). It is hypothesized that a layer of fat and tissue near the surface of the transducer distorts the phase of the transmitted pulse which limits the accuracy of the high frequency fundamental beam more than the harmonic beam. Fig. 1.1 is an ultrasonic image of a renal cyst with harmonic imaging shown on the left and conventional ultrasound shown on the right. The harmonic image has less noise and demonstrates a septation at the bottom left of the cyst. The mural nodes, visible at the top and right side of the cyst, are also easier to distinguish. The physical mechanisms for these image improvements are outlined in the following sections.

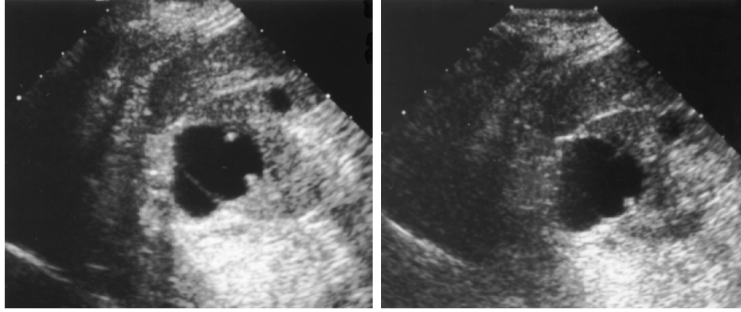


Figure 1.1: A renal cyst. Harmonic imaging (left) demonstrates increased visibility of septation and a mural nodule within the cyst when compared to the noisier fundamental image (right). Image from Choudhry *et al.* [23]

Extracorporeal shock wave lithotripsy alone is used to treat 75% of kidney stones and an additional 20% are treated in conjunction with other methods [57]. Although the procedure is widely used, the mechanisms for stone comminution are not completely understood. Studies suggest compressive failure [19], dynamic fatigue [104, 133], and acoustic cavitation [35, 36, 122, 136]. The intensity required to break the stone is large enough to induce chronic and acute renal alterations [19, 42], which are comparable to external blunt mechanical trauma. Two physical mechanisms are used as explanations: shearing and tearing of the tissue from shock scattering and cavitation bubble collapse [58].

Before the mechanisms for tissue damage and stone comminution can be understood, the acoustical field inside the body needs to be described. Animal studies have been conducted to measure the *in vivo* acoustic field from a clinical lithotripter [33]. However, measurements in the body where it acts on both tissue and stone are difficult to obtain. A numerical simulation of the field has great potential to fully describe cavitation and shearing.

Another therapeutic modality is high intensity focused ultrasound (HIFU). It is used to heat a region of tissue for 5-10 seconds to achieve temperatures of 60 –

100°C [20] and its primary applications are in prostate and hepatic tumors. The heated region is precise to within 1-10mm and there is little heating in the tissue between the transducer and the focal region. Because the heating needs to be rapid, the intensities used are large (on the order of tens of kW/cm²). Both heating and acoustical propagation are nonlinear. Large negative pressures cause cavitation bubbles which can block the penetration of ultrasound [20, 47]. A numerical method of the nonlinear beam can predict the peak negative pressures on which cavitation calculations rely. The nonlinear acoustical field can also be used as an input to the bio-heat equation to accurately predict the heat's spatial distribution. Predictions based on nonlinear models vary by as much as 40% compared to linear models [63]

1.0.2 Physical motivation and B/A

Linear theory provides a suitable approximation for small amplitude waves such as those used in fetal heart monitors and low amplitude B-mode imaging of tissue[38]. In many cases this approximation is sufficient, although a higher order description is necessary where large amplitudes or long propagation lengths and small attenuation are involved.

These cumulative nonlinear effects are caused by variations of the speed of sound within the wavelength of the propagating wave. An initially sinusoidal wave, for example, has a larger speed of sound when the particle velocity is positive than when it is negative. As the wave propagates the peak compression and peak rarefaction move closer together. Eventually the two coincide and give rise to a pressure discontinuity or shock.

The significance of B/A in acoustics lies in its relationship to the speed of sound, c . From a Taylor series expansion of the equation of state for pressure we can derive

(please see appendix for details)

$$\frac{c}{c_0} = 1 + \frac{B}{2A} \left(\frac{\rho'}{\rho_0} \right) + \frac{1}{4} \left[\frac{C}{A} - \frac{1}{2} \left(\frac{B}{A} \right)^2 \right] \left(\frac{\rho'}{\rho_0} \right)^2 + \dots \quad (1.1)$$

where c_0 is the small signal speed of sound, ρ is the density, ρ_0 is the equilibrium density, and $\rho' = \rho - \rho_0$. The parameter B/A expresses the magnitude of the leading order correction to the small signal speed of sound. In the case of plane wave propagation, $\rho'/\rho_0 = u/c_0$, where u is the particle velocity. The first order equation for the speed of sound is then

$$c = c_0 + (B/2A)u \quad (1.2)$$

For positive B/A , the speed of sound increases with positive particle velocity and decreases with negative particle velocity. This variation in the speed of sound forms the basis of nonlinear acoustics. Typical B/A values and other tissue properties are summarized in Tab. 1.1.

Sample	B/A	α at 1 MHz (m^{-1})	ν	c_0 (m/s)
Water	5.0	0.017	2	1500
Human whole blood	6.3	3.4	1.25	1580
Human liver	7.6	14.9	1.3	1570
Human breast fat	9.6	22	1.5	1460

Table 1.1: Typical B/A and attenuation values (from [24, 52])

1.0.3 Imaging with a Nonlinear Beam

Consider, for example, an ultrasound wave transmitted into tissue with a center frequency of f_0 , as shown in Fig. 1.2. As it propagates nonlinearly, the wavefront steepens and the frequency content changes from having energy only at f_0 to developing energy at multiples of the fundamental frequency (i.e. $2f_0, 3f_0, \dots$).

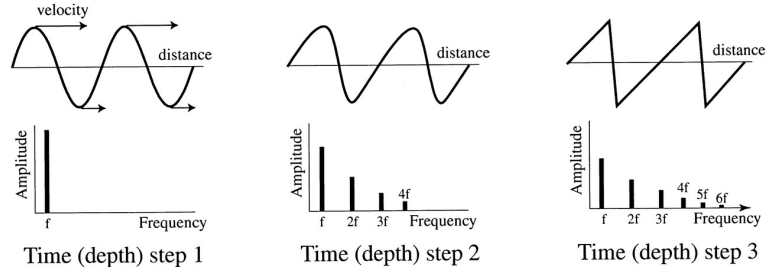


Figure 1.2: Time sequence illustrating the nonlinear propagation of a wave. Note that the harmonic components accumulate as the wave propagates through tissue.

Attenuation and nonlinearity compete for the amplitude of the harmonic frequency signals. As the amplitude of the fundamental component increases the relative amplitude of the harmonic components increases. A large-amplitude fundamental wave generates stronger harmonics than one with a low amplitude. The attenuation, α , of ultrasound in tissue increases with frequency according to a power law [55] so harmonics experience greater attenuation than the fundamental. A schematic representation of this process is shown in Fig. 1.3 [23].

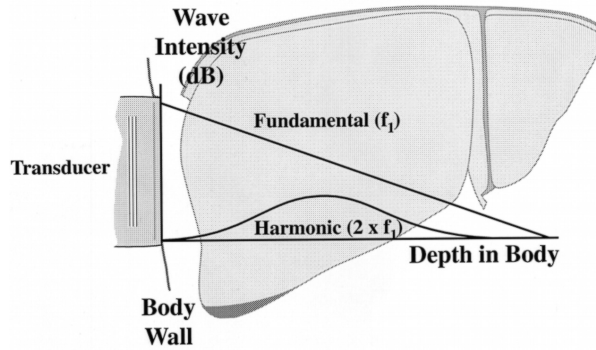


Figure 1.3: A schematic of the relative intensity of the fundamental and harmonic components as they propagate through tissue.

Most modern ultrasonic imaging transducers have a fractional bandwidth of about 70% although experimental models that rely on single crystals or micro-electromechanical

systems can reach values as high as 110%. The frequency response of these transducers can capture the fundamental and second harmonic components. Information from the higher harmonics is lost to bandwidth limitations and attenuation. To form tissue harmonic images, the fundamental and harmonic components must be separated with techniques such as filtering or phase inversion.

1.0.4 Burgers Equation

Burgers' equation describes a propagating plane wave with quadratic nonlinearity. It can be used as a simple model to understand nonlinear propagation, shock wave formation, and shock wave propagation for plane waves. In the following chapters, solutions of Burgers' equation will be used to validate the nonlinear propagation of the proposed numerical models. As with most equations in fluid dynamics, the equation can be derived from conservation of mass and from the momentum equation [52]. In its dimensional form, it can be written as

$$\frac{\partial p}{\partial z} = \frac{\beta p}{\rho_0 c_0^3} \frac{\partial p}{\partial t'} + \frac{\delta}{2c_0^3} \frac{\partial^2 p}{\partial t'^2} \quad (1.3)$$

where the retarded time is given by $t' = t - z/c_0$. The term on the left of the equality represents propagation and the two terms on the right side represent nonlinearity (with the parameter β) and diffusivity (with the parameter δ).

Burgers' equation has been studied extensively since it is one of the simplest nonlinear wave equations [115, 128]. Using the Cole-Hopf transformation, solutions of Burgers' equation are closely related to solutions of the heat equation (see appendix). Note that in acoustics, Burgers' equation has time and space switched when compared to the conventional mathematical treatment. The equation is understood to have an initial condition defined in time, and the nonlinearity develops as the wave propagates

in space.

This equation can be nondimensionalized with the variable substitutions

$$P = p/p_0, \quad \sigma = z/\bar{z}, \quad \tau = \omega_0 t', \quad A = \alpha_0 \bar{z} \quad (1.4)$$

where the plane wave shock propagation distance is $\bar{z} = \rho_0 c_0^3 / \beta p_0 \omega_0$, and the absorption coefficient is $\alpha_0 = \delta \omega_0^2 / 2c_0^3$.

$$\frac{\partial P}{\partial \sigma} = P \frac{\partial P}{\partial \tau} + A \frac{\partial^2 P}{\partial \tau^2} \quad (1.5)$$

The inviscid form of Burgers' equation ignores the effects of attenuation and can be written in the form of a nonlinear scalar conservation law.

$$\frac{\partial P}{\partial \sigma} - \frac{\partial f(P)}{\partial \tau} = 0 \quad (1.6)$$

where the flux function $f(P)$ is

$$f(P) = \frac{1}{2} P^2 \quad (1.7)$$

The characteristic speed, $df/dP = P$, is a function of pressure. As a result, the inviscid Burgers' equation has the implicit solution

$$P(\tau, \sigma) = P_0(\tau - \sigma P(\tau, \sigma)) \quad (1.8)$$

where the initial condition for all time is given by $P_0(\tau) = P(\tau, 0)$. Note that the phase speed is dependent on the pressure much like Eq. 1.2 where the speed of sound is dependent on the particle velocity.

A simple problem is useful in illustrating the characteristic speed and shock de-

velopment. Consider the non-increasing initial conditions

$$P_0(\tau) = \begin{cases} 1 & \tau \leq 0 \\ 1 - \tau & 0 \leq \tau \leq 1 \\ 0 & 1 \leq \tau \end{cases} \quad (1.9)$$

as shown in Fig. 1.4. For $\tau < 0$, the characteristic speed is $df/dP = 1$, so the wave moves with speed 1. For $\tau > 1$, the characteristic speed is $df/dP = 0$, so the wave is stationary. For $0 < \tau < 1$, the characteristic speed varies linearly with τ . As the wave propagates in σ , the front steepens until $\sigma \geq 1$, where it forms a discontinuity. The discontinuity propagates with a speed determined by the Rankine-Hugoniot jump condition.

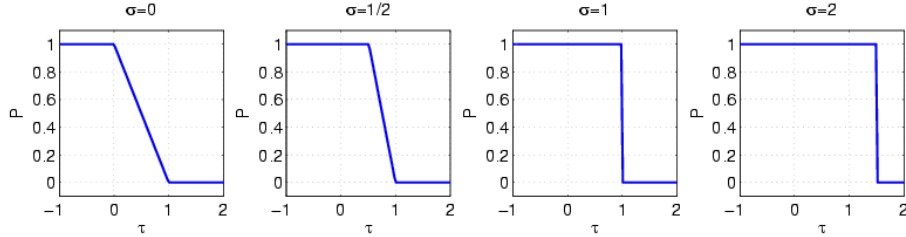


Figure 1.4: Plane wave shock formation described by Burgers' equation with initial conditions in Eq. 1.9. The left-most plot shows the initial conditions ($\sigma = 0$). The second plot ($\sigma = 1/2$) shows the wavefront propagating and the accompanying wave steepening. The third plot ($\sigma = 1$) shows the shock when it first forms and the subsequent plot ($\sigma = 2$) shows the shock propagating.

The plane wave shock formation distance \bar{z} can be calculated by finding the distance at which the waveform first develops a vertical tangent. For Burgers' equation the shock first develops at the point in the wave with the maximum positive slope:

$$\bar{z} = \frac{c_0^2}{\beta \max_{\tau} g_0(\tau)} \quad (1.10)$$

where $g_0(\tau)$ is the source function. This quantity is useful as a characteristic length and in understanding strength of the nonlinearity for a particular waveform. For the Riemann problem above, the maximum slope of the source function occurs in the region $0 \leq \tau \leq 1$. A sinusoidal initial condition is perhaps a better approximation of an ultrasonic initial condition and it has the shock wave distance

$$\bar{z} = \frac{1}{\beta \varepsilon k} \quad (1.11)$$

where $\varepsilon = u_0/c_0$ is the acoustic Mach number.

Table 1.2 shows some plane wave shock propagation distances for a material that has the same nonlinearity coefficient of liver. Note that these systems are all focused and that this effect is ignored in the calculation.

Modality	f (MHz)	p (MPa)	\bar{z} (cm)
Imaging	5	1	30
HIFU	2	5	15
Lithotripsy	2	50	1.5

Table 1.2: Plane wave shock propagation distances in liver ($\beta = 3.5$)

As the shock wave develops the nonlinearity competes with the frequency dependent attenuation. The balance between the processes is characterized by the Gol'dberg number:

$$\Gamma = \frac{\beta \varepsilon k}{\alpha} \quad (1.12)$$

which is the ratio of the shock wave formation distance and dissipation. At diagnostic frequencies, for example, the Gol'dberg number is about two orders of magnitude smaller for tissue than for water. This large difference explains why shock waves form more easily in water than in tissue and why water tank measurements of the acoustical field do not translate easily to estimated fields in tissue.

1.0.5 Propagation of Discontinuities

If the equations governing $P(\tau, \sigma)$ satisfy the integral form of the conservation law then the discontinuity satisfies the Rankine-Hugoniot jump condition. As described in [115], if P is discontinuous along the space-time curve $(z(\sigma), \sigma)$ that moves with speed $\gamma = \frac{dz}{d\sigma}$, then

$$\lim_{\tau \downarrow z(\sigma)} f(P(\tau, \sigma)) - \lim_{\tau \uparrow z(\sigma)} f(P(\tau, \sigma)) = \left\{ \lim_{\tau \downarrow z(\sigma)} P(\tau, \sigma) - \lim_{\tau \uparrow z(\sigma)} P(\tau, \sigma) \right\} \gamma \quad (1.13)$$

For example, discontinuities described by Burgers' equation with the initial conditions of Eq. 1.9 have a speed

$$\gamma = \frac{f(0) - f(1)}{0 - 1} = \frac{1}{2} \quad (1.14)$$

Numerical methods face the challenge of predicting this discontinuity speed and of modeling the discontinuity without becoming unstable or overly diffusive. We will use knowledge from the Rankine-Hugoniot conditions and characteristic analysis of Burgers' equation to validate numerical models for a more complex equation.

1.0.6 KZK equation

The Khokhlov-Zabolotskaya-Kuznetsov (KZK) equation is an augmented form of Burgers' equation. In addition to absorption and nonlinearity, it also accounts for diffraction. This last term allows the KZK equation to describe three dimensional directional nonlinear sound beams; the type generated by ultrasonic transducer.

The nonlinear parabolic KZK wave equation describes the effects of diffraction, absorption, and nonlinearity. Its axisymmetric form in terms of pressure can be written as[12]

$$\frac{\partial^2 p}{\partial z \partial t'} = \frac{c_0}{2} \nabla_{\perp}^2 p + \frac{\delta}{2c_0^3} \frac{\partial^3 p}{\partial t'^3} + \frac{\beta}{2\rho_0 c_0^3} \frac{\partial^2 p^2}{\partial t'^2} \quad (1.15)$$

where $t' = t - z/c_0$ is the retarded time, z is the direction of propagation. The first term on the right hand side represents diffraction, with c_0 as the small signal speed of sound. As with Burgers' equation, the second term accounts for thermoviscous attenuation with δ as the diffusivity parameter. Nonlinearity is described in the third term with $\beta = 1 + B/2A$ as the coefficient of nonlinearity and ρ_0 as the ambient fluid density. The transverse Laplacian can be written in axisymmetric coordinates

$$\nabla_{\perp}^2 p = \left(\frac{\partial^2 p}{\partial r^2} + \frac{1}{r} \frac{\partial p}{\partial r} \right) \quad (1.16)$$

or Cartesian coordinates

$$\nabla_{\perp}^2 p = \left(\frac{\partial^2 p}{\partial x^2} + \frac{\partial^2 p}{\partial y^2} \right) \quad (1.17)$$

Equation 1.15 describes directional sound beams [4, 52] and is valid when $ka \gg 1$, where k is the wave number and a is the characteristic width of the source. The KZK equation was originally derived for the diffusionless ($\delta = 0$) case by Zabolotskaya and Khokhlov in 1969 [131] and Kuznetsov added the absorption term in 1971 [67].

Numerical simulations of the KZK equation began in 1984 with frequency domain methods. Aanonsen *et al.* [1] were able to model the KZK equation in the near-field and Hamilton *et al.* [53] extended the model to the farfield. These techniques were developed at the University of Bergen, therefore the corresponding numerical methods are often referred to as the Bergen code. Experimental measurements have validated the Bergen code for plane [11, 74, 109] and focused circular fields [4, 5, 8], pulsed systems [7, 10], and rectangular geometries [9, 14].

The KZK equation has also been solved in the time domain with finite differences and operator splitting. These methods were introduced by Lee *et al.* [68] in 1995 at the University of Texas and hence it is referred to as the Texas code. Relaxation methods can be incorporated in the KZK equations to include arbitrary

absorption mechanisms [32]. The Texas code was used to model an electrohydraulic lithotripter [3] and the formation of harmonic images with first order operator splitting [69] and second order operator splitting [132]. Time domain solutions of the KZK equation were extended to a fully three dimensional geometry in 2005 [89, 130].

One of limitations of the KZK equation is its reliance on the parabolic or paraxial approximation. It is assumed that the wave-field is in a narrow beam and the source dimension is much larger than a wavelength. The validity of the KZK equation is weakened for strongly focused fields and far off-axis points. Other numerical methods have been implemented to overcome these conditions. In 1991 Christopher and Parker, for example, developed a frequency domain model that uses the angular spectrum to calculate diffraction [30, 31]. This model has been used to simulate lithotrippers [25], *in situ* exposure [26, 29], and harmonic imaging [28]. Khokhlova *et al.* proposed a method similar to Christopher's but with second order operator splitting [108] and a variable number of frequency components [63, 64], which allows sharper wave features to be modeled.

1.0.7 Absorption

The equations of fluid dynamics predict absorption of energy from the thermoviscous interaction of particles as they support wave propagation [73]. Thermoviscous absorption depends on the square of the frequency. Although tissue is similar to fluids in many respects, experimental observation indicates that ultrasonic attenuation in tissue has the power law dependence on frequency, as shown in Eq. 2.16 [55, 65].

One way to remove the discrepancy between theory and observation is with relaxation time constants. An augmented Burgers' equation was derived by Pierce [86]

to include an arbitrary number of relaxation mechanisms (cf. Eq. 1.3).

$$\frac{\partial p}{\partial x} = \frac{\beta p}{\rho_0 c_0^3} \frac{\partial p}{\partial t'} + \frac{\delta}{2c_0^3} \frac{\partial^2 p}{\partial t'^2} + \sum_{\nu} \frac{c_{\nu}}{c_0^2} \int_{-\infty}^{t'} \frac{\partial^2 p}{\partial t''^2} e^{-(t'-t'')/t_{\nu}} dt'' \quad (1.18)$$

where each relaxation process ν is characterized by the relaxation time t_{ν} and a variation in the small signal speed of sound c_{ν} . This equation can be used to model arbitrary frequency dependent absorption over a prescribed frequency range

One of the consequences of frequency dependent attenuation is small frequency dependent variations in the speed of sound (see Appendix F for the Kramers Krönig relation). These variations are required to maintain causality [125] and are shown to have a small but non-negligible effect on the nonlinear propagation [124]. Equation 1.18 has been shown to satisfy the Kramers Krönig relation [105].

Chapter 2

Numerical solutions of the Khokhlov-Zabolotskaya-Kuznetsov equation satisfying the Rankine-Hugoniot condition

The work presented in this chapter is in press in Ultrasonic Imaging [94].

2.1 Introduction

The description of large amplitude ultrasonic beams require an accurate representation of nonlinearity, absorption, and diffraction. The nonlinear parabolic wave equation or the Khokhlov-Zabolotskaya-Kuznetsov (KZK) equation has been widely studied. It describes paraxial sound beams and is valid when the size of the aperture is much larger than the wavelength[4, 52].

There are no analytical solutions of the KZK equation, research has been directed toward numerical solutions. Aanonsen *et al.* [1] were able to model the KZK equation in the nearfield and Hamilton *et al.* [53] extended the model to the farfield. This code, known as the Bergen code, has been validated for plane [11, 74, 109] and focused circular fields [4, 5, 8], pulsed systems [7, 10], and rectangular geometries [9, 14].

Christopher and Parker developed a frequency domain model that uses the angular spectrum to calculate diffraction [30]. This model has been used to simulate lithotriptors [25], *in situ* exposure [26, 29], and harmonic imaging [28]. Khokhlova *et al.* proposed a frequency domain method with second order operator splitting[108] and a variable number of frequency components [63, 64], which allows sharper wave

features to be modeled.

The KZK equation has also been solved in the time domain with finite differences and operator splitting. These methods were introduced by Lee *et al.* [68] and are referred to as the Texas code. Relaxation methods can be incorporated in the KZK equations to include arbitrary absorption mechanisms [32]. The Texas code was used to model an electrohydraulic lithotripter [3] and the formation of harmonic images with first order operator splitting [69] and second order operator splitting [132]. Time domain solutions of the KZK equation were extended to a fully three dimensional geometry [89, 130].

Acoustic beams emitted from intense sources are used extensively in therapeutic and diagnostic ultrasonics. High intensity focused ultrasound (HIFU) is used routinely to treat tumors[62] and shock wave lithotripsy (SWL) has dramatically improved the treatment of renal stones[18].

Although SWL is widely used, the mechanisms for stone comminution are not completely understood. Studies suggest compressive failure [19], dynamic fatigue [104, 133], and acoustic cavitation [36, 122, 136]. The intensity required to break renal stones is large enough to induce chronic and acute alterations in the kidney [19, 42] which are comparable to external blunt mechanical trauma. Two physical mechanisms are used as explanations—shearing and tearing of the tissue from shock scattering and cavitation bubble collapse [58].

Before the mechanisms for tissue damage and stone comminution can be understood, the acoustical field inside the body needs to be described. Animal studies have been conducted to measure the *in vivo* acoustic field from a clinical lithotripter [33]. However, measurements in the body are difficult to obtain. A numerical simulation of the field has potential to fully describe cavitation and shearing and consequently to improve stone comminution while reducing tissue damage.

HIFU heats a region of tissue for 5-10 seconds to achieve temperatures of 60 – 100°C and its primary applications are in prostate and hepatic tumors [20]. Because the heating needs to be rapid, the intensities used are large – on the order of tens of kW/cm². Both heating and acoustical propagation are nonlinear. Large negative pressures cause cavitation bubbles which can block the penetration of ultrasound[20, 47] or modify the lesion shape[6]. Numerical methods for the nonlinear beam can predict the peak negative pressures on which cavitation calculations rely. Also, the nonlinear acoustical field can be used as an input to the bio-heat equation to more accurately predict the heat’s distribution [51, 63].

Discrepancies still exist between measured nonlinear acoustic beams and simulations. This paper addresses a mechanism to improve the accuracy: propagating the shock wave with a speed that satisfies the conservation of flux, known as the Rankine-Hugoniot relation, independently of the attenuation and grid size. The proposed methods are compared with the current time domain method in the context of acoustical fields that model lithotripsy and HIFU in water and tissue. In lithotripsy the peak pressures play an important role in cavitation and shear gradients. The temporally averaged intensity, which affects heating, is compared for the HIFU cases.

2.2 Basic equations

2.2.1 KZK equation

The nondimensionalized KZK equation can be written as

$$\frac{\partial P}{\partial \sigma} = \frac{1}{4G} \int_{-\infty}^{\tau'} \nabla_{\perp} P d\tau' + A \frac{\partial^2 P}{\partial \tau^2} + NP \frac{\partial P}{\partial \tau} \quad (2.1)$$

where

$$P = p/p_0, \quad \sigma = z/d, \quad \tau = \omega_0(t - z/c_0) \quad (2.2)$$

The pressure variable is given by p and p_0 is the normalizing pressure that corresponds to the peak pressure at the initial conditions. The propagation distance is given by z and it is normalized by the focal depth d . The retarded time, τ , tracks the average phase speed c_0 and is normalized by the angular frequency ω_0 .

The dimensionless parameters in Eq. 2.1 are

$$G = z_0/d, \quad N = d/\bar{z}, \quad A = \alpha_0\bar{z} \quad (2.3)$$

where $\bar{z} = \rho_0 c_0^3 / \beta p_0 \omega_0$ is the plane wave shock formation distance at the pressure p_0 , $\alpha_0 = \delta \omega_0^2 / 2c_0^3$ is the thermoviscous attenuation coefficient at a frequency ω_0 , $z_0 = \omega_0 a^2 / 2c_0$ is the Rayleigh distance, ρ_0 is the density, and β is the coefficient of nonlinearity. These parameters represent the focusing gain (G), nonlinearity (N), and attenuation (A).

The nondimensionalized transverse Laplacian has a similar variable substitution

$$\rho = r/a_r, \quad \xi = x/a_x, \quad \zeta = y/a_y \quad (2.4)$$

$$\nabla_{\perp}^2 P = \left(\frac{\partial^2 P}{\partial \rho^2} + \frac{1}{\rho} \frac{\partial P}{\partial \rho} \right) \quad (2.5)$$

and Cartesian coordinates

$$\nabla_{\perp}^2 P = \left(\frac{\partial^2 P}{\partial \xi^2} + \frac{\partial^2 P}{\partial \zeta^2} \right) \quad (2.6)$$

and a is the characteristic width of the aperture in the dimension indicated by the subscript.

2.2.2 Rankine-Hugoniot condition

The equation governing nonlinearity (Eq. 2.10) is a nonlinear conservation law. Any discontinuity described by a conservation law satisfies the Rankine-Hugoniot jump condition, which is a restatement of the conservation of flux. If P is discontinuous along the space-time curve $(z(\sigma), \sigma)$ that moves with speed $\gamma = \frac{dz}{d\sigma}$ then [115]

$$\gamma = \frac{\lim_{\tau \downarrow z(\sigma)} f(P(\tau, \sigma)) - \lim_{\tau \uparrow z(\sigma)} f(P(\tau, \sigma))}{\lim_{\tau \downarrow z(\sigma)} P(\tau, \sigma) - \lim_{\tau \uparrow z(\sigma)} P(\tau, \sigma)} \quad (2.7)$$

where f represents the flux for the conservation law.

Numerical methods face the challenge of predicting this discontinuity speed and of modeling the discontinuity without becoming unstable or overly diffusive. The Rankine-Hugoniot condition and characteristic analysis of Burgers' equation will be used to validate numerical methods for the nonlinear operator.

2.3 Numerical methods

Operator splitting applies numerical techniques to each of the terms in the equation independently over a propagation step[115]. By integrating both sides with respect to τ , the KZK equation can be rewritten as

$$\frac{\partial P}{\partial \sigma} = \mathcal{L}_D(P) + \mathcal{L}_A(P) + \mathcal{L}_N(P) \quad (2.8)$$

where \mathcal{L}_D , \mathcal{L}_A , and \mathcal{L}_N are the operators for diffraction, absorption, and nonlinearity. A first order operator splitting scheme applies the numerical methods sequentially at

each propagation step thus approximating the solution:

$$P = S_{\mathcal{L}_N \Delta \sigma} \circ S_{\mathcal{L}_A \Delta \sigma} \circ S_{\mathcal{L}_D \Delta \sigma}(P_0) + O(\Delta \sigma^2) \quad (2.9)$$

where P_0 is the initial condition, $\Delta \sigma$ is the step size in the direction of propagation, and S represents the numerical method for a particular operator.

This paper focuses on numerical methods used to solve the nonlinear operator, also known as the inviscid Burgers' equation,

$$\frac{\partial P}{\partial \sigma} = NP \frac{\partial P}{\partial \tau} \quad (2.10)$$

Burgers' equation is well studied because it is one of the simplest nonlinear equations[128]. Differences in the shock speed are readily observable and understood for the plane wave described by Eq. 2.10. The KZK equation, however, complicates the wave field with diffraction, focusing, and absorption. This paper compares the effect of predicting the correct shock speed with a stationary shock speed for clinically relevant applications of the KZK equation.

2.3.1 Implicit solution based method

As described by Lee *et al.*,[68] the implicit solution of Burgers' equation

$$P(\sigma, \tau) = P_0(\tau + NP\sigma) \quad (2.11)$$

can be used in conjunction with linear interpolation to obtain

$$P_i^{j+1} = \begin{cases} P_i^j \left[1 - N \left(\frac{P_{i+1}^j - P_i^j}{\Delta\tau} \right) \Delta\sigma \right]^{-1} & P_i^j \geq 0 \\ P_i^j \left[1 - N \left(\frac{P_i^j - P_{i-1}^j}{\Delta\tau} \right) \Delta\sigma \right]^{-1} & P_i^j < 0 \end{cases} \quad (2.12)$$

where i and j represent the discretization in space and time, respectively. This equation incorporates information about the characteristics and is a form of upwind differencing. It is used in current time domain methods for the KZK equation such as the Texas code. It can be easily verified that this method is not conservative because $\sum_i P_i^{j+1} - \sum_i P_i^j$ does not equal the boundary terms [115].

2.3.2 Godunov's method

A commonly used method for nonlinear hyperbolic conservation laws is Godunov's scheme [48]. It is a generalization of upwind differencing for nonlinear problems:

$$P_i^{j+1} = P_i^j - \frac{\Delta\sigma}{\Delta\tau} \left[f_{i+1/2}^{j+1/2} - f_{i-1/2}^{j+1/2} \right] \quad (2.13)$$

The flux for Burger's equation is $f(P) = NP^2/2$ and Godunov's method represents it as

$$f_{i+1/2} = \begin{cases} \frac{N}{2} \max\{P_i, \min\{P_{i+1}, 0\}\}^2, & P_i < P_{i+1} \\ \frac{N}{2} \max\{|P_i|, |P_{i+1}|\}^2, & P_i \geq P_{i+1} \end{cases} \quad (2.14)$$

This method has been amply characterized[115] and is known to satisfy the Rankine-Hugoniot relation (Eq. 2.7). We propose it as a more precise alternative to the spectral method and the implicit solution based method in the solution of the nonlinear operator for the KZK equation.

2.3.3 MUSCL scheme

The Monotone Upstream-centered Scheme for Conservation Laws (MUSCL) scheme combines the upwind, Beam-Warming, Fromm, and Lax-Wendroff methods. It is monotonic and has the advantage over Godunov's method of being second order. Due to its length a full description is omitted here but can be found in [115, 119].

2.3.4 Diffraction

The simulations in this paper solve diffraction in the time domain. As proposed by Lee *et al.*[68] the axisymmetric diffraction operator of the KZK equation can be solved with fully implicit and Crank-Nicolson finite differences. The axisymmetric geometry is used to model circular transducers. With the scheme the linear equations are tridiagonal and relatively straightforward to solve. An equivalent method can be applied to the Cartesian diffraction operator[89, 130] to solve the fully three dimensional KZK equation. To preserve the accuracy of the second order derivatives, the diffraction operator is kept unsplit in this paper so the linear systems are no longer tridiagonal and they present additional computational requirements when compared to the axisymmetric linear systems. The Cartesian geometry is used to calculate the beams for rectangular transducers. Details for these methods are lengthy and are omitted here but they can be found in the fore-cited literature. The boundary conditions minimize unphysical reflections [41].

2.3.5 Absorption

Thermoviscous absorption in the KZK equation is represented by the operator

$$\frac{\partial P}{\partial \sigma} = A \frac{\partial^2 P}{\partial \tau^2} \quad (2.15)$$

This equation predicts absorption which depends on the square of the frequency. It behaves like the heat equation and can be solved in the time domain with standard finite difference methods[68, 115]. Although tissue is similar to fluids in many respects, experimental observation indicates that ultrasonic attenuation in tissue has the power law dependence on frequency shown in Eq. 2.16 [55, 65]. For soft tissue, ν is between 1.1 and 1.5. Absorption in the time domain can be solved with relaxation mechanisms[32].

$$\alpha = f^\nu \tag{2.16}$$

Attenuation and dispersion can be easily represented in the frequency domain. A plane wave solution in can be substituted into Eq. 2.16 to obtain the system of ODE's:

$$\frac{dP_n}{d\sigma} = -n^2 A P_n \tag{2.17}$$

The dependence on n^2 on the right hand side demonstrates the frequency squared dependence of thermoviscous attenuation. Because attenuation in tissue is determined from observation we can perform the empirical substitution[52]

$$n^2 A \rightarrow A_n + jD_n \tag{2.18}$$

to represent arbitrary frequency dependent attenuation A_n and dispersion D_n . Every frequency that can be represented by the simulation has an arbitrary absorption coefficient associated with it. This implementation of absorption has been validated in the context of the Bergen code and Christopher's code. This algorithm is implemented for this paper with FFT's using the Fastest Fourier Transform in the West library [46].

2.3.6 Computational requirements

Because the memory and processing requirements are demanding for 3D systems, the numerical methods are solved in parallel. Processing and internode communication is handled with version 7.0.6 of the LAM/MPI toolkit and communication occurs over a private gigabit network on a SMC8748L2 switch. This code runs on a Linux cluster with eight nodes and two AMD Opteron 270 (dual core, 2.0GHz) processors per node. Each node has 8 GB of RAM. All the systems run CentOS 4, a free version of Red Hat Enterprise Linux 4. The parallel code uses SCALAPACK and PBLAS [15].

2.4 Results

2.4.1 Solutions of the inviscid Burgers' equation

The Riemann problem is commonly used to characterize numerical methods for shock wave propagation. The initial conditions in Eq. 2.19 allow the wave to propagate a certain distance before the shock is formed. Then at $\sigma = 1$ the wave reaches the Riemann initial conditions and the shock region can be verified.

$$P_0(\tau) = \begin{cases} 1 & \tau \leq 0 \\ 1 - \tau & 0 \leq \tau \leq 1 \\ 0 & 1 \leq \tau \end{cases} \quad (2.19)$$

For $\tau < 0$ and $N = 1$ the characteristic speed is $df/dP = P = 1$, the wave moves with speed 1. For $\tau > 1$ the characteristic speed is $df/dP = P = 0$, the wave is stationary. For $0 < \tau < 1$ the characteristic speed varies linearly with τ . As the wave propagates

in σ , the front steepens until $\sigma \geq 1$, where it forms a discontinuity. The discontinuity propagates with a speed determined by the Rankine-Hugoniot jump condition. In this case:

$$\gamma = \frac{f(0) - f(1)}{0 - 1} = \frac{1}{2} \quad (2.20)$$

Figure 2.1 compares the analytic solution to the numerical solutions the initial conditions described in Eq. 2.19 at three depths, σ . The grid sizes are $\Delta\tau = 0.05$ and $\Delta\sigma = 0.045$.

The implicit solution based method is shown with the “x” marks. It is well known that such finite difference methods are not designed to propagate thin shock waves, however we show it here to illustrate how it breaks down under certain conditions. It correctly predicts the inviscid Burgers’ equation phase speed in the pre-shock region ($\sigma < 1$) however it fails to propagate the wave when the discontinuity forms. The Godunov scheme is shown with circles and the MUSCL schemes is shown with crosses. As expected these methods correctly predict the shock wave speed. The MUSCL scheme needs fewer points to resolve the discontinuity because it is a higher order scheme than Godunov’s method.

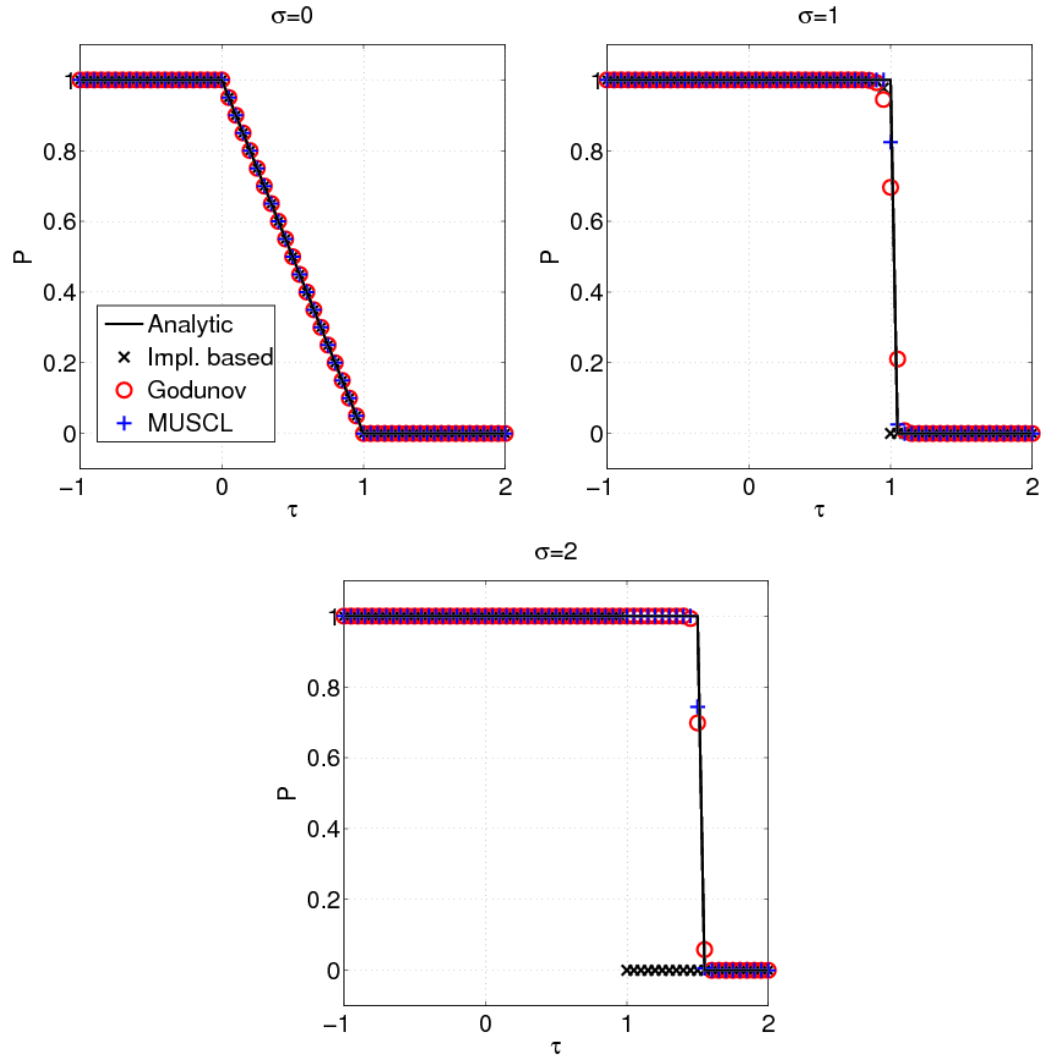


Figure 2.1: A comparison of the analytic solution of the inviscid Burgers' equation with the initial conditions in Eq. 2.19 to the numerical solutions in one spatial dimension. The nondimensionalized pressure P is plotted against the retarded time τ for varying propagation distance, σ . Godunov's method and the MUSCL scheme satisfy the Rankine-Hugoniot condition whereas the implicit solution based method does not, in this case.

2.4.2 Solutions of the viscid Burgers' equation

In most physically relevant situations there is a non-negligible amount of thermoviscous attenuation. Attenuation increases the shock thickness and relaxes the

grid, requirements. With enough viscosity and a sufficiently refined grid the implicit solution based method predicts the correct Rankine-Hugoniot shock wave speed.

Fig. 2.2 characterizes the grid requirements as a function of the attenuation coefficient. The figure plots the number of grid points required to predict the shock wave speed to within 10% of its correct value. The nonlinearity is $N = 1$ and the Courant-Friedrichs-Levy (CFL) condition is fixed: $\Delta\sigma/\Delta\tau = 0.9$.

As the attenuation decreases the number of grid points required by the implicit solution based method increases. The power law slope as estimated from Fig. 2.2 is 2.03. The Godunov and MUSCL schemes are shown for reference but they do not require grid refinement to predict the correct shock wave speed. At large attenuation values the grid requirements for the implicit solution based method are not much larger than those for the Godunov or MUSCL schemes. When the ratio of attenuation to nonlinearity becomes small, as is commonly encountered for lithotripsy or HIFU in water, the grid size can be six orders of magnitude larger.

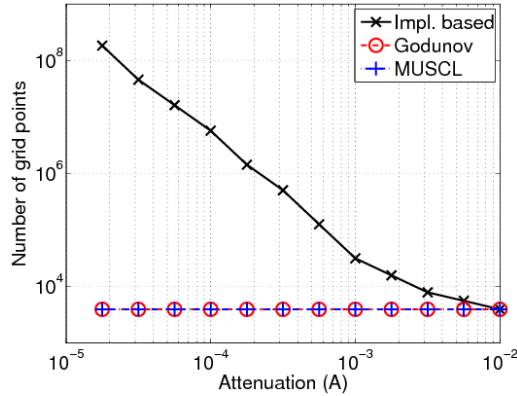


Figure 2.2: Number of grid points required to correctly predict the shock wave speed as a function of attenuation. Here $N = 1$ and $CFL = 0.9$. The Godunov and MUSCL schemes are shown for reference; they do not require refinement with changes in attenuation.

2.4.3 Lithotripsy

Lithotripters produce a wave that is well suited for comparisons of the stationary and Rankine-Hugoniot shocks because much of the wave propagation occurs in water where the nonlinear parameter dominates attenuation. The initial conditions of a lithotripter closely resemble a decaying exponential, which is consistent with the wave form of an underwater explosion[34]. A decaying exponential has been previously used to describe the pressure source of a Dornier HM-3 lithotripter and has been shown to produce more accurate results than other initial wave forms[134].

$$p(t) = Ce^{-(t-t_0)/T}H(t - t_0) \quad (2.21)$$

Equation 3.19 describes the unfocused initial conditions at the transducer surface. Here C is the pressure amplitude, T is the characteristic time, t_0 is the time at which the pulse starts, and H is the Heaviside function.

The simulations model a circularly symmetric parabolically focused lithotripter in water with an aperture of 10 cm, a focal depth of 12.8 cm, a nonlinear parameter of 3.5, a center frequency of 0.5 MHz, a speed of sound 1,500 m/s, an attenuation of 0.0016 Np/m/MHz, and pressure of 7 MPa. The corresponding nondimensional parameters are $G = 20.3$, $N = 2.9$, $A = 1.0e-4$. The numerical methods are identical except for the nonlinear step. The grid sizes are $\Delta\sigma = 3.3e-04$, $\Delta\tau = 0.039$, $\Delta\rho = 0.0011$. The number of points in each dimension are 5250 (σ), 1800 (τ), and 1800 (ρ), for a total of $1.7e10$ grid points. These grid parameters reflect current values used in the literature.

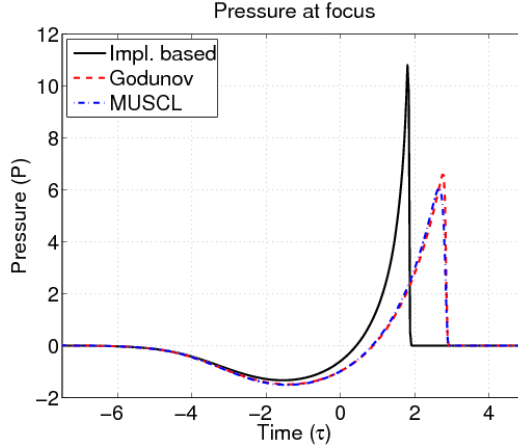


Figure 2.3: Nondimensionalized pressure at the focus ($\sigma = 1$) for numerical solutions of the KZK equation with implicit based (solid), Godunov (dashed), and MUSCL (dash-dotted) schemes.

The nondimensionalized pressure at the focus of the lithotripter is shown in Fig 2.3 for the implicit based (solid) and Godunov (dashed) and MUSCL (dash-dotted) schemes. The position of the shock for the implicit solution based method is delayed compared to the other schemes. More importantly the methods that satisfy the Rankine-Hugoniot condition predict different peak negative and peak positive pressures.

Table 2.1 shows the peak positive pressure predicted by Godunov’s and MUSCL’s schemes is almost half that predicted by the implicit solution based method. The peak negative pressures are about 10% larger.

	P_+	P_-
Impl. based	11.4	-1.47
Godunov	6.63	-1.65
MUSCL	6.11	-1.67

Table 2.1: A comparison of the lithotripter peak pressures.

Pressure as a function of depth is more precisely characterized in in Fig. 2.4. In

the prefocal region, up to a depth of $\sigma = 0.6$ the implicit solution based, Godunov, and MUSCL schemes yield similar peak positive and negative pressures. The greatest disparity between the methods occurs in the focal region where the effects of nonlinearity are strongest due to the large pressures. The agreement between the methods resumes in the post focal region, at a depth of $\sigma > 1.3$. Although the peak negative pressures have different magnitudes they more closely resemble scaled versions of each other.

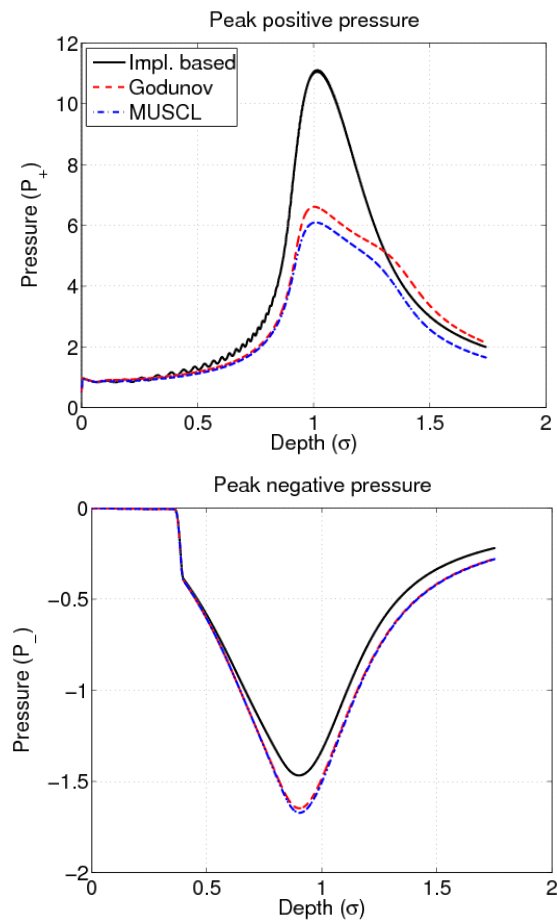


Figure 2.4: Peak positive (top) and peak negative (bottom) nondimensionalized pressure as a function of depth.

2.4.4 HIFU

As with lithotripsy, a circular fixed focus HIFU transducer may use a water path to transmit energy to tissue. The first HIFU simulation models an external transducer such as one used for hepatic applications[62]. It has a 10 cm aperture transducer with a focal depth of 15 cm, a center frequency of 1.5 MHz, an initial condition pressure of 5 MPa, a nonlinearity of 3.5 and an attenuation of 0.0016 Np/m/MHz. The corresponding nondimensional parameters are $G = 52.4$, $N = 3.67$, $A = 3.6e - 4$. The grid parameters are $\Delta\sigma = 3.75e - 4$, $\Delta\tau = 0.052$, $\Delta\rho = 0.0017$. The number of points in each dimension are 4000; (σ), 4000 (τ), and 1200 (ρ), for a total of $1.9e10$ grid points. The transducer emits a parabolically focused continuous wave pulse.

Fig. 2.5 plots the nondimensionalized pressure at the focus. As in the lithotripter simulation the position of the shock front for the implicit solution based method is significantly delayed compared to the other two methods and the peak positive pressure is significantly larger.

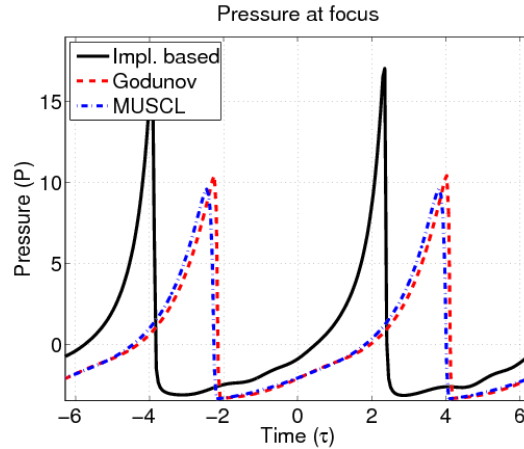


Figure 2.5: Nondimensionalized HIFU pressure at the focus ($\sigma = 1$) for numerical solutions of the KZK equation for propagation in water from a circular transducer.

Fig. 2.6 shows the I_{SPTA} intensity defined as

$$I_{SPTA} = \frac{1}{2T} \max_{\sigma} \int_{-T}^T P^2(\sigma, \tau) d\tau \quad (2.22)$$

The intensity pattern follows a similar distribution as the peak positive pressure (not shown). Differences between the two methods are more strongly localized about the focus. The majority of the variation occurs at the depths $0.93 < \sigma < 1.1$. For depths outside the focus there is a closer match between the methods.

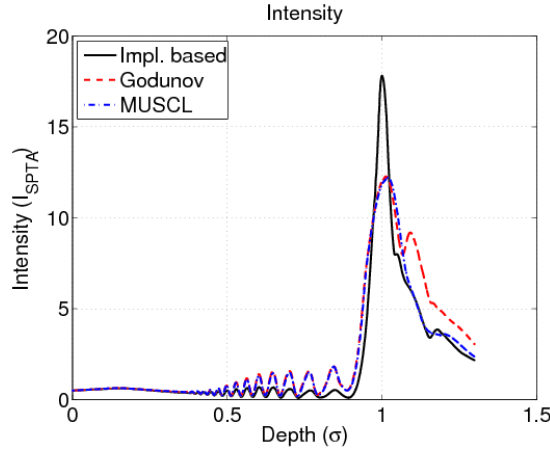


Figure 2.6: Nondimensionalized I_{SPTA} intensity as a function of depth for propagation in water from a circular transducer.

The order of attenuation in tissue is close to the order for nonlinearity so it has a more prominent effect on wave propagation than attenuation in water. However the computational requirements for the three dimensional simulation are more demanding and the grid sizes are smaller. In the following simulation a transrectal rectangular HIFU probe is modeled. It has a 3 cm lateral aperture, a 1 cm elevation aperture, a focal depth of 4 cm in both lateral and elevation dimensions, a center frequency of 3.5 MHz, an initial condition pressure of 5 MPa, the nonlinearity parameter is 5 and attenuation is modeled with a $f^{1.1}$ power law. The corresponding nondimensional

parameters are $G_x = 33.0, G_y = 3.67, N = 5.7, A = 0.60$. The grid parameters are $\Delta\sigma = 2.5e - 04, \Delta\tau = 0.31, \Delta\xi = 0.0125, \Delta\zeta = 0.025$. The number of points in each dimension are 4000; (σ), 400 (τ), 108 (ξ), and 52 (ζ), for a total of $1.4e10$ grid points.

As shown in Fig. 2.7 the difference in position between the shock front is smaller than in the low attenuation case. In this example, the solutions are similar, however the Godunov and MUSCL schemes predict a significantly lower peak negative pressure (27%) which impacts the intensity.

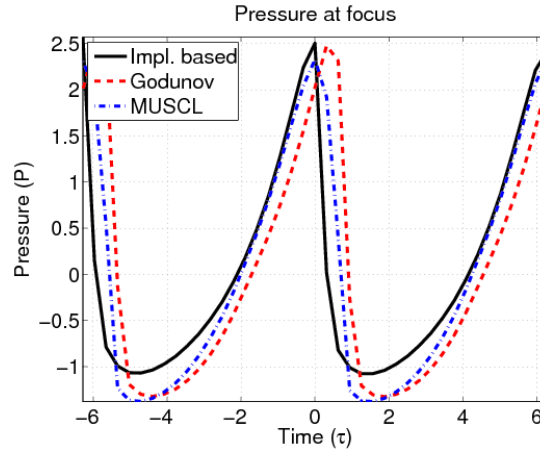


Figure 2.7: Nondimensionalized HIFU pressure at the focus ($\sigma = 1$) for numerical solutions of the KZK equation with stationary (dashed) and Rankine-Hugoniot (solid) shock speeds. Propagation is in tissue from a rectangular transducer.

Fig. 2.8 shows that the difference in intensity predicted by the Godunov and MUSCL schemes is considerably different throughout a wide region about the focus when compared to the implicit solution based method. A difference of over 30% is sustained at depths of $0.5 < \sigma < 1.1$ where the majority of ultrasonic heating occurs.

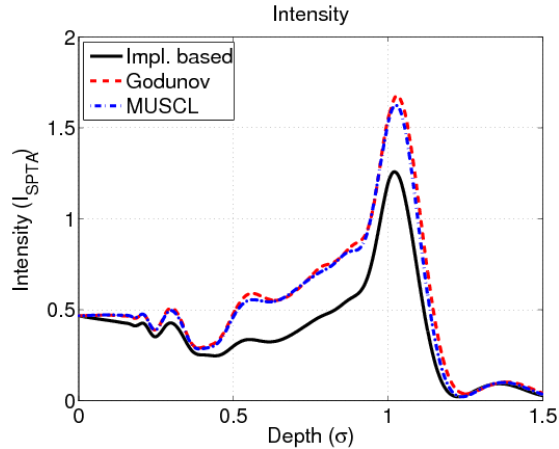


Figure 2.8: Nondimensionalized intensity as a function of depth for propagation in tissue from a rectangular transducer.

2.5 Summary and Conclusions

Planar simulations of the inviscid Burgers' equation have demonstrated that Godunov's method satisfies the Rankine-Hugoniot relation. Current numerical methods approximate the shock speed as being stationary relative to retarded time. Simulations that model lithotripsy and HIFU indicate that propagating the shock with the correct speed has a significant impact on the acoustical field.

In the presence of attenuation the implicit solution based method requires grid refinement as the attenuation decreases. The number of grid points needed to predict the correct shock wave speed increases as the square of the decrease in attenuation. As the attenuation decreases the number of points in the shock must increase to obtain an accurate solution. The Godunov and MUSCL schemes do not require refinement with decreases in attenuation. These schemes satisfy the Rankine-Hugoniot relation at all attenuation values with no changes in the grid size. The computational cost per grid point of the Godunov method is less than the implicit solution based method

and slightly larger for the MUSCL scheme.

A coarse discretization is advantageous when the grid size is large or when specific details of the shock do not need to be simulated. If, for example, the rise-time of the shock needs to be simulated, then the grid needs to be sufficiently refined to include several points within the shock thickness. With such a refined grid both the flux-based methods and the current implicit solution based method are capable of correctly solving the shock wave propagation problem.

With a ratio of the attenuation coefficient to the nonlinearity coefficient on the order of 10^{-5} , such as those encountered in lithotripsy simulations, the number of grid points required to satisfy the Rankine-Hugoniot relation is six orders of magnitude larger than an equivalent Godunov or MUSCL based simulation. The grid requirements for the implicit solution based method taxes available computational resources in 2D and 3D simulations. Grid sizes that do not satisfy the requirements for the Rankine-Hugoniot condition have been used and may yield significantly different results if flux is conserved.

As the shock wave forms in the lithotripter simulations the Rankine-Hugoniot speed of the front pulls it away from the negative phase of the wave. The 10% larger peak negative pressure predicted by the Godunov and MUSCL based simulations suggests that cavitation will occur earlier than from current models. The peak positive pressure is almost half as large indicating that the calculations for bubble formation and collapse as well as the shear gradients may be significantly affected.

The HIFU simulation in water with a circular transducer exhibits a substantial variation in peak positive pressure that is strongly localized at the focus. The intensity at the focus predicted by the Godunov and MUSCL based simulations simulation is 65% of that predicted by the stationary shock front. The Rankine-Hugoniot simulations suggest that the energy deposited at the focal region is less localized than

current models predict.

Simulations in tissue from a rectangular transducer show that the simulations that satisfy the Rankine-Hugoniot condition yield larger peak negative pressures for a wide depth range about the focus. The intensity calculations exhibit a significant difference—30% larger at the focus for the Rankine-Hugoniot satisfying simulations. The total amount of energy deposition about the focus predicted by this model is thus substantially larger.

The application of the proposed numerical method to these three simulations demonstrate that satisfying the Rankine-Hugoniot conditions in simulations of non-linear beams has a significant impact. These results apply to 2D simulations but they even more important in 3D where the computational constraints are more significant and the implicit solution based method cannot realistically satisfy the Rankine-Hugoniot conditions.

2.6 Acknowledgments

The authors are grateful to John Trangenstein for discussions on numerical methods. This work was supported by NIH grants R01-HL075485 and 1R01-CA114093-02.

Chapter 3

Numerical solution of the parabolic wave equation with cubic nonlinearity

The work presented in this chapter was submitted to IEEE Transaction on Ultrasonics, Ferroelectronics, and Frequency Control [95].

3.1 Introduction

Focused acoustic beams emitted from intense sources are used extensively in therapeutic ultrasound. In procedures such as shock wave lithotripsy (SWL), the pressures are large enough to induce compressive failure [19], dynamic fatigue [104, 133], acoustic cavitation and bubble collapse [36, 122, 136] in renal calculi. The intensity is also large enough to induce acute alterations in the kidney from the shearing gradients and bubble collapse [19, 42, 58]. Accurate numerical simulations of the acoustical field have the potential to improve stone comminution and minimize damage to the surrounding tissue.

The Khoklov-Zabolotskaya-Kuznetsov (KZK) equation is a nonlinear beam equation that has been used to model nonlinear wave propagation in therapeutic ultrasound [3, 134]. The KZK equation models the effects of quadratic nonlinearity, attenuation, and diffraction in the paraxial approximation. The nonlinear term of this parabolic wave equation has previously been extended to include the cubic nonlinearity within the paraxial approximation [112]. This higher order description is necessary because the pressures involved in SWL are large enough that a quadratic approximation of the nonlinearity is less accurate. The peak positive pressures in

lithotripsy are on the order of 50 MPa which is when the ratio of the cubic term to the quadratic term becomes significant (> 0.10).

In this paper a numerical method that solves the parabolic wave equation with cubic nonlinearity is proposed. Solutions of this equation are compared to solutions of the parabolic wave equation with quadratic nonlinearity (the KZK equation) in the context of SWL. The parabolic wave equation is solved numerically in the time domain with operator splitting. The cubic and quadratic nonlinear terms are calculated with the monotone upwind scheme for conservation laws (MUSCL), a second order flux-conservative method used to solve nonlinear hyperbolic partial differential equations. A clinically realistic axis-symmetric lithotripter in a water bath is simulated and the waveforms from the numerical solutions are compared.

3.2 Model Description

3.2.1 Acoustic Equation

The wave equation with paraxial cubic order terms can be derived from fundamental equations in fluid dynamics [112]. In terms of the velocity potential, ϕ , it can be written as

$$\left(\frac{\partial^2}{\partial t^2} - c_0^2 \nabla^2 - \frac{D}{c_0^2} \frac{\partial^3}{\partial t^2} \right) \phi = -\frac{\beta}{c_0^2} \frac{\partial}{\partial t} \left(\frac{\partial \phi}{\partial t} \right)^2 - \frac{\delta}{c_0^4} \frac{\partial}{\partial t} \left(\frac{\partial \phi}{\partial t} \right)^3 \quad (3.1)$$

where the coefficient for the cubic nonlinearity is

$$\delta = \frac{1}{6} \left[10 \frac{B}{A} + 3 \frac{B^2}{A^2} - \frac{C}{A} + 14 \right] \quad (3.2)$$

Here c_0 is the equilibrium speed of sound, the quadratic nonlinearity has the coefficient $\beta = 1 + B/2A$, the diffusivity D can be expressed as a function of the absorption coefficient α with the equation $D = 2\alpha c_0^3/\omega^2$ (where ω is the angular frequency). The nonlinearity parameters follow from the Taylor expansion of the variation in pressure with changes in density.

$$p - p_0 = A \left(\frac{\rho - \rho_0}{\rho_0} \right) + \frac{B}{2} \left(\frac{\rho - \rho_0}{\rho_0} \right)^2 + \frac{C}{6} \left(\frac{\rho - \rho_0}{\rho_0} \right)^3 + \dots \quad (3.3)$$

The paraxial approximation can be extended to the linear operator on the left hand side of Eq. 3.1. The paraxial approximation assumes that variations perpendicular to the direction of propagation are much slower than variations along it [52]. In terms of the acoustic pressure, p , this yields the equation

$$\left(\frac{\partial^2}{\partial z \partial t'} - \frac{c_0}{2} \nabla_{\perp}^2 - \frac{D}{2c_0^3} \frac{\partial^3}{\partial t'^3} \right) p = \frac{\beta}{2\rho_0 c_0^3} \frac{\partial^2 p^2}{\partial t'^2} + \frac{\delta}{2\rho_0^2 c_0^5} \frac{\partial^2 p^3}{\partial t'^2} \quad (3.4)$$

where ρ_0 is the equilibrium density, the retarded time is given by $t' = t - z/c_0$. The transverse Laplacian operates perpendicular to the direction of propagation and in cylindrical coordinates it is given by,

$$\nabla_{\perp}^2 = \frac{\partial^2}{\partial r^2} + \frac{1}{r} \frac{\partial}{\partial r} \quad (3.5)$$

The KZK equation is equal to Eq. 3.4 when the cubic term is zero ($\delta = 0$). Equation 3.4 can be nondimensionalized with the substitutions

$$P = p/p_0, \quad \sigma = z/d, \quad R = r/a, \quad \tau = \omega_0 t' \quad (3.6)$$

where p_0 is the peak pressure, d is the focal length of a focused beam, and a is the

width of the aperture. Then,

$$\frac{\partial P}{\partial \sigma} = \frac{1}{4G} \int_{-\infty}^{\tau} \nabla_{\perp} P d\tau' + T \frac{\partial^2 P}{\partial \tau^2} + N_1 \frac{\partial P^2}{\partial \tau} + N_2 \frac{\partial P^3}{\partial \tau} \quad (3.7)$$

where

$$G = \frac{\omega_0 a^2}{2c_0 d}, \quad T = \frac{D d \omega_0^2}{2c_0^2}, \quad N_1 = \frac{\beta d p_0 \omega_0}{2\rho_0 c_0^3}, \quad N_2 = \frac{\delta d p_0^2 \omega_0}{2\rho_0^2 c_0^5} \quad (3.8)$$

The parameters G , T , N_1 , N_2 , respectively represent the small-signal focusing gain, thermoviscous absorption, quadratic nonlinearity, and cubic nonlinearity. This non-dimensional form of the parabolic wave equation is used in the numerical investigations.

3.2.2 Numerical Method

Operator splitting applies numerical techniques to each of the terms in the equation independently over a propagation step and it has been used successfully in the context of the KZK equation [68, 115, 132]. Here it is applied to the parabolic wave equation with cubic nonlinearity with the operators split as

$$\frac{\partial P}{\partial \sigma} = \mathcal{L}_D(P) + \mathcal{L}_A(P) + \mathcal{L}_N(P) \quad (3.9)$$

where \mathcal{L}_D , \mathcal{L}_A , and \mathcal{L}_N are the operators for diffraction, absorption, and the combined cubic and quadratic nonlinearity. A first order operator splitting scheme applies the numerical methods sequentially at each propagation step. Details of operator splitting and the solution of the diffraction and absorption terms are omitted as they can be found in the general numerical literature [115] or specifically in the context of the KZK equation [68]. We instead focus on the portions of the algorithm that rely on numerical solutions for higher order nonlinearity.

Conventionally, numerical solutions of the KZK equation in the time domain are

based on an implicit solution of the quadratic nonlinear operator [68]. Here a numerical method that solves both the quadratic and cubic terms is proposed. The MUSCL scheme is a second order flux-conservative method used to solve nonlinear hyperbolic partial differential equations. It is a combination of the upwind differencing, Beam-Warming, Fromm, and Lax-Wendroff methods. A general treatment can be found in [115]; it is described here in detail for these specific combined quadratic and cubic nonlinear terms. In conservation law form these terms can be written as

$$\frac{\partial P}{\partial \sigma} = \frac{\partial f(P)}{\partial \tau} \quad (3.10)$$

where the flux function is $f(P) = N_1 P^2 + N_2 P^3$. If the coordinate system is discretized in space with the index n and in retarded time with the index j then the characteristic speed is,

$$\lambda_j^n = \frac{\partial f}{\partial P}(P_j^n) = 2N_1 P_j^n + 3N_2 (P_j^n)^2 \quad (3.11)$$

Let the side increments be,

$$\Delta P_{j+1/2}^n = P_{j+1}^n - P_j^n \quad (3.12)$$

the centered increments,

$$\Delta P_j^n = \frac{1}{2}(\Delta P_{j+1/2}^n + \Delta P_{j-1/2}^n) \quad (3.13)$$

and the MUSCL slopes,

$$s_j^n \Delta \tau = \begin{cases} \text{sign}(\Delta P_j^n \min\{2|P_{j-1/2}^n|, 2|P_{j+1/2}^n|, |P_j^n|\}), & \Delta P_{j+1/2}^n \Delta P_{j-1/2}^n > 0 \\ 0 & \text{otherwise} \end{cases} \quad (3.14)$$

Characteristic tracing is then used to compute the states at the left and right of the cell boundaries:

$$\text{if } \lambda_j^n > 0, \text{ then } P_{j+1/2}^L = P_j^n + \frac{1}{2} \left(1 - \frac{\lambda_j^n \Delta \sigma}{\Delta \tau} \right) s_j^n \Delta \tau, \text{ else } P_{j+1/2}^L = P_j^n \quad (3.15)$$

$$\text{if } \lambda_j^n < 0, \text{ then } P_{j-1/2}^R = P_j^n - \frac{1}{2} \left(1 + \frac{\lambda_j^n \Delta \sigma}{\Delta \tau} \right) s_j^n \Delta \tau, \text{ else } P_{j-1/2}^R = P_j^n \quad (3.16)$$

Then the flux at the solution of the Riemann problem for the cubic nonlinear equation is evaluated with the assumption that $N_1, N_2 > 0$:

$$\begin{aligned} &\text{if, } P_{j+1/2}^L < P_{j+1/2}^R, \\ &\quad \text{a) if, } 0 < P_{j+1/2}^L < P_{j+1/2}^R : f_{j+1/2} = f(P_{j+1/2}^L) \\ &\quad \text{b) if, } -\frac{N_1}{N_2} < P_{j+1/2}^L < 0 < P_{j+1/2}^R : f_{j+1/2} = f(0) = 0 \\ &\quad \text{c) if, } P_{j+1/2}^L < -\frac{N_1}{N_2} : f_{j+1/2} = f(P_{j+1/2}^L) \\ &\quad \text{d) if, } -\frac{N_1}{N_2} < P_{j+1/2}^L < P_{j+1/2}^R < 0 : f_{j+1/2} = \min\{f(P_{j+1/2}^L), f(P_{j+1/2}^R)\} \\ &\text{if, } P_{j+1/2}^L > P_{j+1/2}^R, \\ &\quad \text{a) if, } -\frac{2N_1}{3N_2} < P_{j+1/2}^R < P_{j+1/2}^L : f_{j+1/2} = \max\{f(P_{j+1/2}^L), f(P_{j+1/2}^R)\} \\ &\quad \text{b) if, } P_{j+1/2}^R < -\frac{2N_1}{3N_2} < P_{j+1/2}^L : f_{j+1/2} = \max\{f(P_{j+1/2}^L), f\left(-\frac{2N_1}{3N_2}\right)\} \\ &\quad \text{c) if, } P_{j+1/2}^R < P_{j+1/2}^L < -\frac{2N_1}{3N_2} : f_{j+1/2} = f(P_{j+1/2}^L) \end{aligned} \quad (3.17)$$

Finally a conservative difference is used to compute the solution at the new step in space

$$P_j^{n+1} = P_j^n - \frac{\Delta \sigma}{\Delta \tau} [f_{j+1/2}^{n+1/2} - f_{j-1/2}^{n+1/2}] \quad (3.18)$$

Equation 3.18 represents the nonlinear step in the operator splitting procedure described in Eq. 3.9.

3.3 Results

The initial waveform of a spark lithotripter are similar to an underwater explosion and can be closely approximated with a decaying exponential[34]. This type of initial condition has been previously used to describe the pressure source of a Dornier HM-3 lithotripter[134],

$$p(t) = p_0 e^{-(t-t_0)/\eta} H(t - t_0) \quad (3.19)$$

Equation 3.19 describes the initial condition as a function of time. Here η is the characteristic time, t_0 is the time at which the pulse starts, and H is the Heaviside function. The simulation models a circularly symmetric parabolically focused lithotripter in water with an aperture of 10 cm, a focal depth of 12.8 cm, a center frequency of 0.5 MHz, a speed of sound 1,500 m/s, an attenuation of 0.0016 Np/m/MHz, and pressure of 7 MPa. The quadratic nonlinearity parameter was $B/A = 5.2$ and the cubic nonlinearity parameter was $C/A = 32$, which are accepted values for distilled water [129]. The corresponding nondimensional parameters are $G = 20.3$, $A = 0.00010$, $N_1 = 1.51$, $N_2 = 0.026$. The grid sizes are $\Delta\sigma = 6e - 05$, $\Delta\tau = 2\pi/150$, $\Delta\rho = 0.0013$.

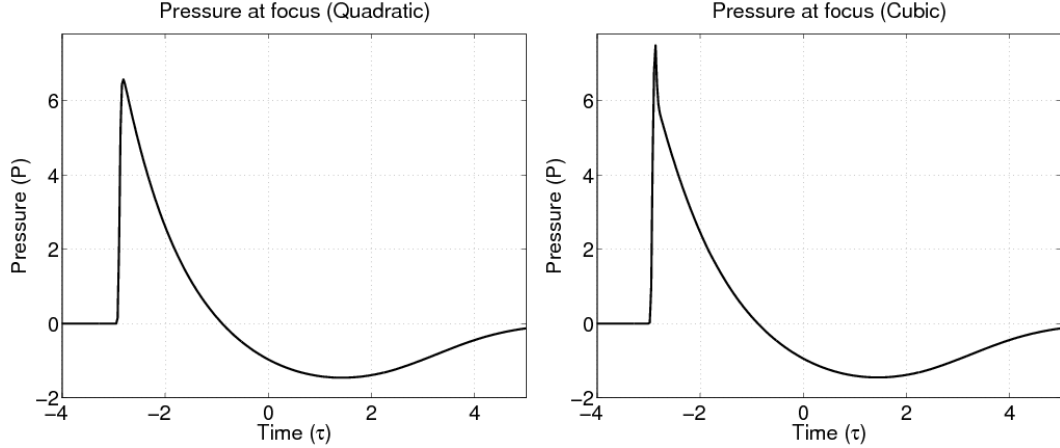


Figure 3.1: Nondimensionalized pressure at the focus ($\sigma = 1$) for numerical solutions of the parabolic wave equation with quadratic and cubic nonlinearity.

The nondimensionalized pressure at the focus of the lithotripter is shown in Fig 3.1 for the quadratic and cubic nonlinearity. The peak pressures are 46.1 MPa and 52.6 MPa, respectively. There is a 14% difference can be accounted for by the substantial size of the cubic term at high pressures. At 52.6 MPa the size of N_2 is 12% of N_1 . There is also a slight narrowing of the pulse near the positive peak. The peak negative pressure is small enough that the effect of the cubic term is negligible. According to the Rankine-Hugoniot shock speed relation the increased flux from the cubic term also causes the shock front to travel faster [115]. At the focus the shock from the cubic simulation precedes the quadratic shock front by 16 ns.

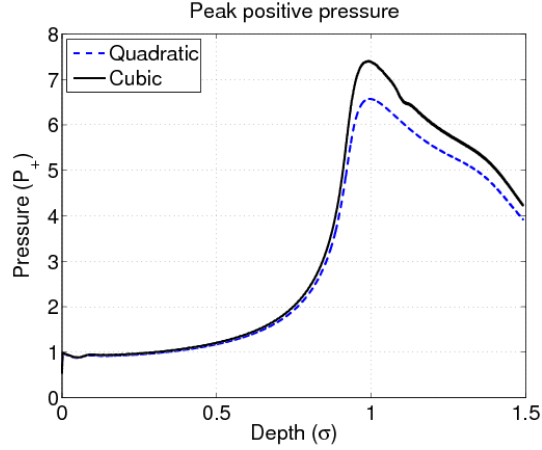


Figure 3.2: Peak positive nondimensionalized pressure as a function of depth for quadratic (dashed) and cubic (solid) nonlinearity.

Variations in the peak positive pressure as a function of depth are characterized in Fig. 3.2. As expected, the biggest difference occurs at the focus where the pressure is large and the contribution of the cubic term is significant. After the nonlinear distortion of the wave from the cubic term has developed it persists until well after the focus. Even though the pressures decrease the effect of the cubic term is still significant. In the region preceding the focus, such as the initial condition surface the pressure is 7 MPa and the size of N_2 is 1.5% of N_1 , which is too small to have significant impact on the nonlinear distortion.

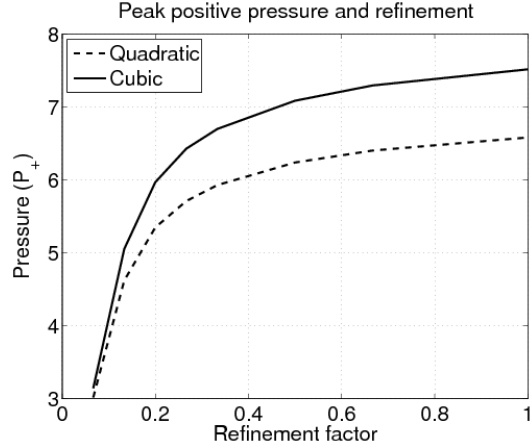


Figure 3.3: Peak positive nondimensionalized pressure as a function of grid refinement for quadratic (dashed) and cubic (solid) nonlinearity.

To test the accuracy of the numerical method a refinement analysis was performed. Figure 3.3 shows the convergence of the peak positive pressure at the focus with refinement of the grid size. The refinement factor is the fraction of the finest grid used in the simulation (described previously). The peak pressures are close to their asymptotic values though additional refinement would result in an increase. The difference between the peak pressures is also stable so even though additional refinement would slightly increase the peak pressures, the difference between the predictions would still be significant.

3.4 Conclusions

A new numerical method for highly nonlinear ultrasonic wave propagation has been presented. The method solves the parabolic wave equation with cubic nonlinearity and was compared to solutions of the conventional parabolic wave equation with quadratic nonlinearity in the context of lithotripsy. The solution of the nonlinear terms rely on a numerical method specifically designed for shock wave propagation

from nonlinear hyperbolic conservation laws. The accuracy of the numerical solutions were verified with a refinement analysis.

The numerical investigation demonstrated that cubic nonlinearity has an important effect at pressure amplitudes such as those encountered in SWL. The 14% larger peak pressure and narrower pulse shape predicted by the simulation with cubic nonlinearity suggest that simulations that rely on quadratic nonlinearity underestimate the shear gradients involved in lithotripsy. The difference in peak positive pressures develop near the focus and once the nonlinear distortion of the wave has been achieved, persist until well after the focus.

3.5 Acknowledgments

This work was supported by NIH grants R01-HL075485 and 1R01-CA114093.

Chapter 4

A comparison of time domain solutions for the full-wave equation and the parabolic wave equation for diagnostic ultrasound transducers

The work presented in this chapter is in press in IEEE Transaction on Ultrasonics, Ferroelectronics, and Frequency Control [93].

4.1 Introduction

Numerical solutions of linear acoustic fields in ultrasonics can be used to determine fundamental beam properties such as the axial and lateral resolution, contrast, and penetration. These solutions are commonly based on time or frequency domain descriptions of the linear full-wave equation but in some cases it is computationally advantageous to use a one-way wave equation. In particular, the parabolic wave equation can be used in lieu of the full-wave equation when the direction of propagation is within 15° of the axis of propagation, such as in narrow beams. Its validity has been investigated theoretically for transducers [111] and its numerical solution has been shown to be useful when other terms, such as nonlinearity, are added to the description of wave propagation [68]. The parabolic wave equation, however, cannot describe reflections, scattering, the off-axis field, two-way propagation in the axial direction, and because of its retarded time frame, heterogeneities.

The purpose of this paper is to investigate the accuracy of finite difference time domain methods (FDTD) that solve the linear wave equation and the parabolic

wave equation in the context of modeling the ultrasonic field emitted by a diagnostic ultrasound transducer in three dimensions. Previous work has been applied to radially symmetric geometries and including thermoviscous attenuation, such as circular piston transducers [68, 109], but computational requirements have prevented an analysis of realistic rectangular phased ultrasound transducers. In the FDTD simulations presented here a 56 processor computer cluster with 100 GB of memory was required. Attenuation is neglected here to simplify the simulations and the analysis of the results. The numerical results are compared to solutions calculated by Field II, a commonly accepted numerical model that solves the wave equation. Although Field II and the FDTD method both solve the wave equation, the finite difference scheme can additionally simulate propagation through finely heterogeneous media, multiple scattering, and reflections so it can be used to simulate the complex propagation of ultrasonic pulses through a realistic three-dimensional representation of tissue [72, 87].

Both numerical methods discussed in this paper were originally developed for nonlinear propagation. The intent of this paper is also to establish the validity of numerical methods for nonlinear waves when propagation occurs in the linear regime. The finite difference techniques used here can be directly extended to simulate nonlinear propagation. With the addition of a quadratically nonlinear term and thermoviscous attenuation, the wave equation becomes the Westervelt equation [87], and the parabolic wave equation becomes the Khokhlov-Zabolotskaya-Kuznetsov (KZK) equation [68], both of which have been solved numerically.

4.2 Equations

The linear wave equation in a homogeneous medium can be written as

$$\frac{1}{c_0^2} \frac{\partial^2 p}{\partial t^2} - \nabla^2 p = 0 \quad (4.1)$$

where c_0 is the equilibrium speed of sound, and p is the pressure. The parabolic wave equation assumes that variations perpendicular to the direction of propagation are much slower than variations along it [52]

$$\frac{\partial^2 p}{\partial z \partial t'} - \frac{c_0}{2} \left(\frac{\partial^2 p}{\partial x^2} + \frac{\partial^2 p}{\partial y^2} \right) = 0 \quad (4.2)$$

z is the direction of propagation, the retarded time is given by $t' = t - z/c_0$. This assumption is also known as the paraxial approximation and it limits the validity of the equation to propagation within 15° of the axis (the z direction) and the single derivative in z limits propagation to one direction along the axis.

4.3 Methods

Two transducer configurations are simulated. In the first case the $f/\#$ is 1.5, so that the angle between the farthest point of the transducer and the axis at the focus is 33.7° which is not consistent with the paraxial approximation of the parabolic wave equation. Note that the full-wave equation is valid at all angles. The second simulation has an $f/5$ or a maximum angle of 11.3° , which is within the valid range of the paraxial approximation. This allows us to verify the validity of the numerical methods within their theoretical limits and the applicability of the parabolic approximation to weakly non-paraxial propagation in ultrasound transducers.

The linear full-wave equation was solved with fourth order finite difference discretizations in the spatial domain and standard second order discretizations in time. The spatial stencil for the diffraction operator is based on rotations of the discretiza-

tion,

$$\nabla^2 p_z \approx (-p_{i,j,k-2}^n + 16p_{i,j,k-1}^n - 30p_{i,j,k}^n + 16p_{i,j,k+1}^n - p_{i,j,k+2}^n)/12\Delta z^2 \quad (4.3)$$

shown here for the Z-axis. A perfectly matched layer that reduces the incident pulse by 78 dB was used as an absorbing boundary condition. The numerical method is solved explicitly and further details of the implementation can be found in *Pinton et al.* [87] in the context of the nonlinear full-wave equation.

The parabolic wave equation was solved with implicit finite differences in the time domain using operator splitting [68, 130]. The method used here is different because the transverse Laplacian was kept unsplit in order to preserve the accuracy of the diffraction operator in three dimensions [89]. Fine fully implicit steps are used for the first few wavelengths of propagation and coarser steps are used for the higher order Crank-Nicolson scheme at larger depths.

The grid size for the full-wave simulation was $\Delta x = \Delta y = \Delta z = 20\mu\text{m}$ for the three spatial coordinates and $\Delta t = 2.6\text{ ns}$ in time. The parabolic wave equation was discretized with $\Delta x = \Delta y = 20\mu\text{m}$ in the lateral elevation plane, $\Delta t' = 2.6\text{ ns}$ in retarded time, $\Delta z = 1.2\mu\text{m}$ for the first 100 steps and $\Delta z = 12\mu\text{m}$ for the remaining steps in the propagation dimension.

Field II uses the Tupholme-Stepanishen method for calculating linear pulsed ultrasound fields in a homogeneous. The spatially varying impulse response of the acoustic source is convolved with the excitation function [60]. Field II has been used and evaluated extensively in ultrasonic transducer modeling.

The transducer was modeled to match the proposed algorithm, meaning the kerf was set to zero and an element size of $20\mu\text{m}$ by $20\mu\text{m}$ was used to model an active aperture size of 16 mm by 5 mm. The number of mathematical elements used for

each $20 \mu\text{m}$ by $20 \mu\text{m}$ was set to 1. The soft baffle boundary condition was used in the Field II simulation, and a parabolically focused profile was used in both the lateral and elevation dimensions.

In addition, the angular response of the transducer elements was negated by applying an apodization of

$$\theta = \tan^{-1}(x/d_z); \quad (4.4)$$

$$\text{apod}_{\text{lat}} = \text{sinc}(a_x \sin(\theta)/\lambda) \cos(\theta) \quad (4.5)$$

in the lateral and elevation dimensions. Here a_x is the element width, d_z indicates the focal depth, and x indicates lateral position. The proposed algorithm does not apply an angular weight to the transducer elements. To reduce error, a high sampling frequency of 160 MHz was used in the Field II simulation. The accuracy of the Field II simulations was also verified by reducing the element size and changing the rectangular elements to the more accurate triangular elements, none of which altered the Field II solutions. Also note that the elements are so small that their associated far field is negligibly close and does not affect the accuracy of the simulations. As described in Ref. [61] we expect the error in the Field II calculation to be less than 3 to 5% of the analytic solution.

The transducer modeled in the following simulations is a Siemens VF10-5 linear array (Siemens Medical Solutions USA, Inc., Issaquah, WA) with 192 elements, a 2 cm elevation focus, 2.4 cm lateral focus, an f/1.5 or 5, and a 4.2 MHz center frequency. The element dimensions are 0.201 mm width and 5 mm height. For the purposes of the simulations the element kerf was assumed to be negligible. The simulation domain was 1.5 cm laterally, 1 cm in elevation, and 3.35 cm in depth, on the positive quadrant of the lateral-elevation plane. A parabolically focused profile was used in both the lateral and elevation dimensions, and was modeled as a continuous function

$$p(x, y, z = 0) = p_0 f(t + x^2/2c_0d_x + y^2/2c_0d_y) \quad (4.6)$$

where d_x is the lateral focus, d_y is the focus in elevation, p_0 is the peak pressure, and f is the sinusoidal pulse function. The number of cycles was set to 1.667 with a Gaussian envelope so that the fractional bandwidth was approximately 0.6.

4.4 Results

Figure 4.1 shows the lateral pressure contour plot of f/1.5 beams calculated by Field II on the left, the full-wave equation in the center, and the parabolic wave equation on the right taken at the center of the elevation plane. Results in the elevation plane exhibit similar characteristics and are omitted in the interest of concision. Field II and the full-wave equation have almost indistinguishable distributions. There is a 1 mm difference in the depth at which the proximal -6 dB finger begins and the -20 dB contour is slightly narrower for the full-wave simulation at shallow depths, but overall these two plots are best described by their similarities rather than their differences. The numerical solution for the parabolic wave equation, on the other hand, exhibits marked deviations from the Field II standard. The -6 dB finger is absent, the -10 dB contour begins deeper, and the overall beam focus is deeper.

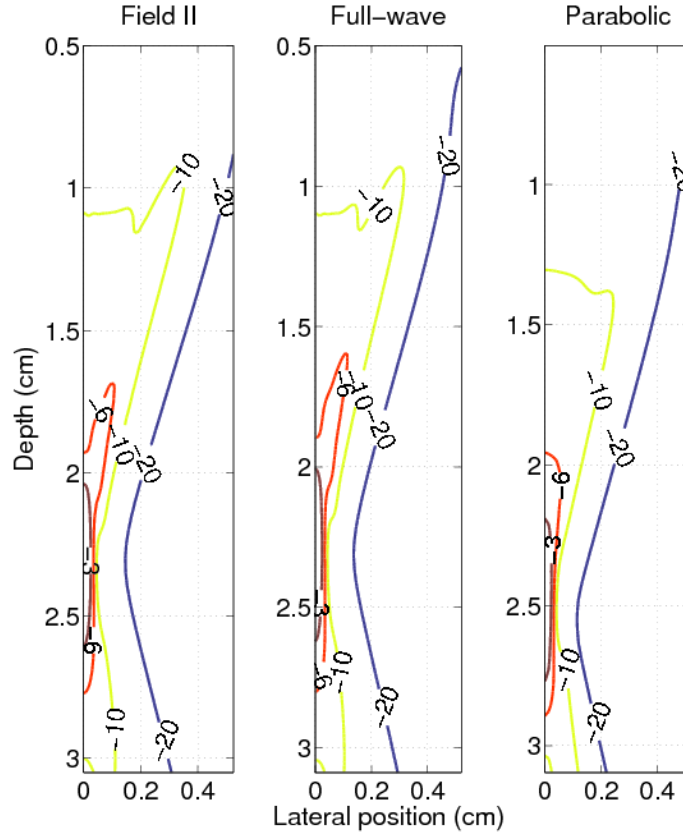


Figure 4.1: Lateral contour plots for simulations of a diagnostic ultrasound transducer with an $f/1.5$ using Field II (left), finite differences applied to the full-wave equation (center), and finite differences applied to the parabolic wave equation (right). The slice is at the center of the elevation plane

Differences in the position of the focus are more precisely characterized by the normalized axial intensity plots in Fig. 4.2. Field II and the finite difference full-wave solutions predict a peak in the intensity at a depth of 2.35 cm and the solution of the parabolic wave equation predicts 2.50 cm. The parabolic wave equation also predicts a relatively lower intensity in the pre-focal region and the small hump preceding the main peak is absent. There is an insignificant difference in the full-width half-maximum (FWHM) of all three numerical solutions.

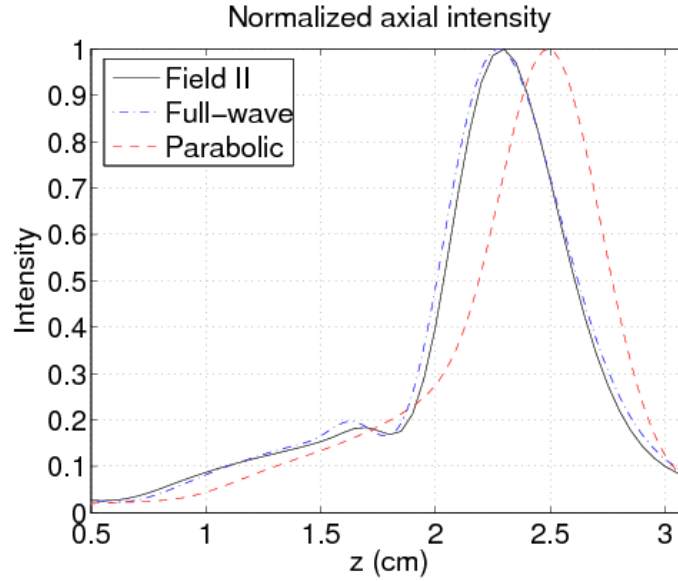


Figure 4.2: The normalized axial intensity for simulations of a diagnostic ultrasound transducer with an $f/1.5$ using Field II (solid), finite differences applied to the full-wave equation (dash-dotted), and finite differences applied to the parabolic wave equation (dashed).

Figure 4.3 shows the lateral beamplot at the focus and at the center of the elevation plane. The difference between Field II and the finite difference full-wave solutions is less than 0.4 dB across the 2 mm lateral extent. There is no significant difference in the shape of the main-lobe. The parabolic wave equation solution has a narrower main-lobe and 2.7 dB lower side-lobe. These differences persist with an increase in the lateral position.

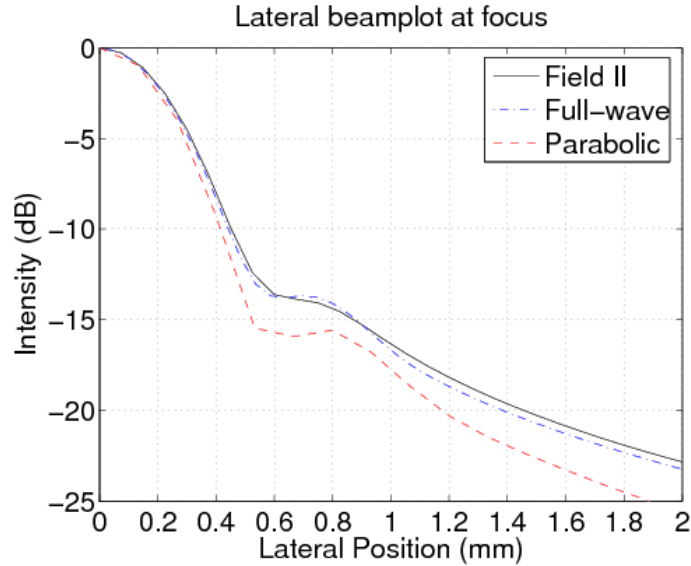


Figure 4.3: The lateral beamplot for simulations of a diagnostic ultrasound transducer with an $f/1.5$ taken at the center of the elevation plane.

In the following simulation the aperture size was reduced to obtain an $f/5$ and the remaining parameters were kept constant. This larger $f/\#$ is consistent with the paraxial approximation because the angle the beam forms with the outermost point of the active transducer is 11.3° . Figure 4.4 shows the lateral beamplot at the focus taken at the center of the elevation plane. Both finite difference solutions are in close agreement with the Field II simulation and within the plotted lateral range the variation is less than 0.5 dB.

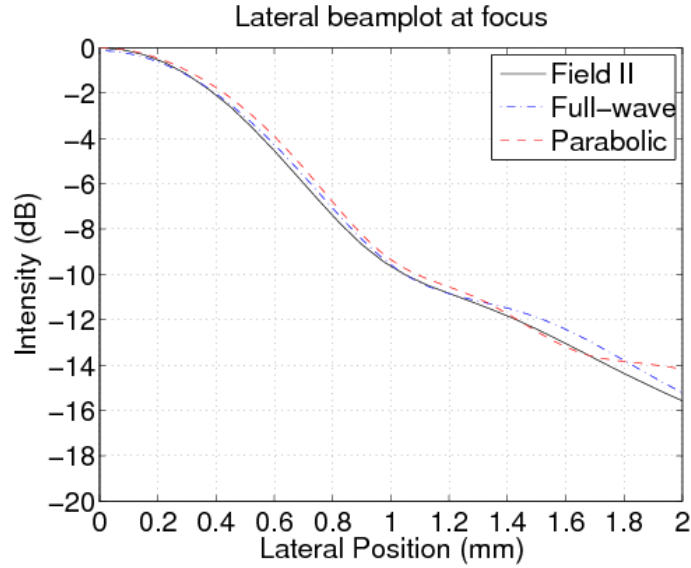


Figure 4.4: The lateral beamplot for simulations of a diagnostic ultrasound transducer with an $f/5$ taken at the center of the elevation plane.

Figure 4.5 shows the axial intensity for the large $f/\#$ simulations. The intensity peaks at 1.33 cm for Field II, 1.39 cm for the full-wave simulation, and 1.51 for the parabolic simulation. The parabolic simulation yields an accurate lateral beamplot but axially its focus is deep when compared to Field II. For this $f/\#$ the position of the focus for the full-wave simulation is also slightly deep, suggesting that numerical error in the finite difference solutions may be contributing to the focal error.

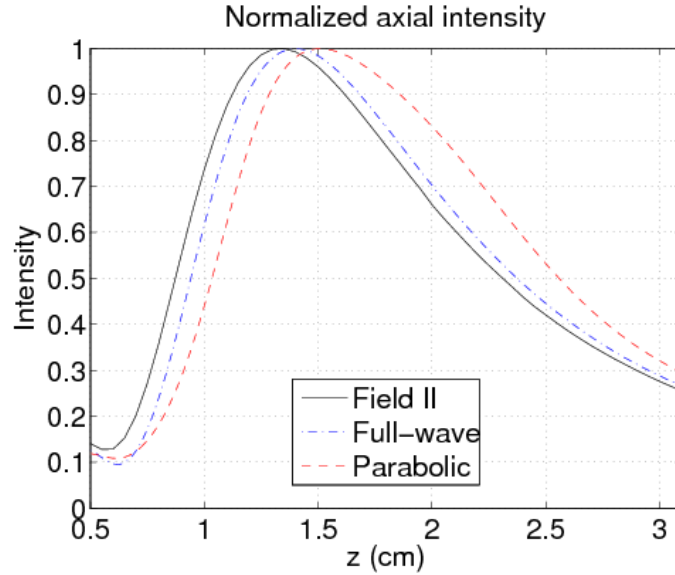


Figure 4.5: The normalized axial intensity for simulations of a diagnostic ultrasound transducer with an $f/5$.

4.5 Conclusion

Finite difference solutions of the full-wave equation and the parabolic wave equation for a diagnostic ultrasound transducer were compared to Field II. In the case of low $f/\#$, where the assumptions of the paraxial approximation are violated, the parabolic equation is significantly different from Field II. The position of the focus is shifted by 1.5 mm, the main-lobe is 4.7% narrower at the FWHM, and the side-lobe is lower by 2-3 dB. The FDTD full-wave simulation, on the other hand, is practically indistinguishable from the Field II simulation. There is no difference in the focus and the lateral beamplot varies by less than 0.4 dB across the 2 mm lateral extent considered. The FDTD simulation is consistent with Field II to within the 3-5% error range expected by the simulation and is within the error of an equivalent water tank measurement.

When the $f/\#$ is changed to 5, and the aperture size is consistent with the paraxial approximation, both the parabolic and full-wave simulations match Field II to within 0.5 dB. The numerical solution to the parabolic wave equation still exhibits a significant focal error of 1.8 mm.

Numerical solutions of the full wave equation are accurate for large and small $f/\#$ s. The lateral beamplot of numerical solutions to the parabolic wave equation is accurate for large $f/\#$ s but exhibit focal errors at both large and small $f/\#$ s.

The computation time of the three dimensional FDTD simulations is approximately 32 hours on a computer cluster. Given the computational challenge of exploring a multidimensional parameter space, investigations that examine the error as a function of $f/\#$, frequency, and transducer geometry are postponed to future publications.

4.6 Acknowledgments

This work was supported by NIH grants R01-HL075485 and 1R01-CA114093.

Chapter 5

A heterogeneous nonlinear attenuating full-wave model of ultrasound

The work presented in this chapter was submitted to IEEE Transaction on Ultrasonics, Ferroelectronics, and Frequency Control [87].

5.1 Introduction

Characterization of acoustic waves that propagate nonlinearly in an inhomogeneous medium has important applications in diagnostic and therapeutic ultrasound. The heterogeneous composition of tissue distorts the phase and generates unwanted reverberation of an ultrasonic signal. This results in the degradation of the lateral resolution and contrast of an ultrasonic scanner. The nonlinearity of wave propagation is used to the advantage of diagnostic scanners that use the harmonic components of the ultrasonic signal to improve the resolution and penetration of clinical scanners [59, 110, 116]. Harmonic imaging has been shown to have an important effect in reducing phase aberration and clutter [99, 121, 123].

A number of equations and numerical methods that address nonlinear propagation, heterogeneous media, or multiple scattering have been proposed. Ultrasonic propagation through fine scale heterogeneities has been simulated with a finite difference time domain (FDTD) solution of the 3D linear wave equation [71, 72]. This numerical implementation models the fine structure of human tissue and the arrangement of the tissue in the human body. The full-wave equation accounts for multiple reflections and scattering but current numerical implementations lack the ability to

simulate nonlinear propagation and attenuation.

The Khokhlov-Zabolotskaya-Kuznetsov (KZK) equation or nonlinear one-way parabolic wave equation, accounts for nonlinearity, attenuation, and diffraction within a paraxial approximation [67, 131]. It has been solved in the time and frequency domains [9, 63, 68] however the parabolic wave equation assumes that field variations transverse to the direction of propagation are slow compared to axial variations and the paraxial approximation limits the equation's validity to about 15° from the axis of propagation [107]. Additionally this one-way wave equation does not model reflections, scattering, and heterogeneities.

The nonlinear full-wave equation describes acoustic fields in a nonlinear thermo-viscous medium [52, 127]. It has the advantages of both the three dimensional linear wave equation and the nonlinear parabolic wave equation by incorporating nonlinearity, attenuation, and all wave effects, such as multiple scattering, reflection, and refraction. It is not limited by a paraxial approximation so it accurately describes an ultrasonic beam in the off axis region and it is valid for arbitrary scatterers in the field. An axisymmetric version of this equation has been solved numerically in the context of heat deposition [51].

Here we propose a novel three-dimensional numerical solution to a nonlinear full-wave equation that additionally describes arbitrary frequency dependent attenuation and variations in density. As the accuracy of simulations improves it becomes increasingly important to include higher order effects. We present the first numerical method that comprehensively describes three dimensional nonlinear wave propagation in heterogeneous media with arbitrary attenuation law. This paper also describes the implementation of perfectly matched layers (PML) at the boundaries to reduce reflections to negligible levels. It is shown that the FDTD method can accurately represent nonlinear ultrasonic propagation from a diagnostic transducer and that it

can simulate heterogeneities in speed of sound, attenuation, nonlinearity, and density.

The perfectly matched layer (PML) was introduced by Berenger in the context of electromagnetic waves to provide absorption under a broad variety of conditions [13]. In the continuous limit, it has been shown that the PML interface between the regular medium and the PML completely absorbs the incident wave independently of incidence angle and frequency. Various other methods have been proposed to but they are successful only for a limited range of frequencies and angles of incidence. The PML technique has been previously adapted for acoustics [21, 70] but the methods use low order discretizations for their finite differences. In this paper we introduce a new acoustic PML method for higher order finite differences.

The incorporation of arbitrary frequency dependent absorption laws is straightforward in frequency domain methods. However it is numerically intractable for time-domain methods to solve the equivalent convolution. In this paper, in addition to thermoviscous attenuation, which is only valid for fluids, we use relaxation mechanisms to model arbitrary attenuation, such as the power laws observed in tissue. The numerical methods are based on research in seismic wave fields [40] but are adapted for the high order spatial discretizations used here.

Numerical solutions of the full-wave equation are extensively validated. In the linear, non-attenuating regime results are compared to Field II, a well accepted standard for transducer modeling [60, 61]. Nonlinearity is verified by comparing the distortion of a plane wave with solutions of a frequency domain Galerkin method. Water tank measurements of a commercial ultrasonic transducer are used to validate the combined effects of diffraction, nonlinearity, and attenuation in the simulation results for fundamental and harmonic components of the acoustic field. Once the validation of the method is established the simulation is used to propagate diagnostic ultrasound pulses through an experimentally determined representation of an abdominal layer.

Multiple pulses are used to compose a harmonic and fundamental ultrasound image using the same process that a diagnostic scanner employs. The pulses propagate, aberrate through the abdominal layer, reflect, scatter, and part of the transmitted energy returns to the transducer face where it is beamformed into an image. Unlike other simulations that use nonlinear propagation to create ultrasound images [69], this simulation, in addition to including the effects of inhomogeneities and multiple scattering, does not require any linear convolution assumptions of the point spread function. Finally we examine the effects of clutter on the point spread function and show that one of the primary mechanisms of image degradation in fundamental imaging, compared to harmonic imaging, is the presence of near-field reverberation at the fundamental frequencies.

5.2 Methods

5.2.1 Acoustic Equation

The nonlinear full-wave equation used in this paper is a second order wave equation that describes a nonlinear wave propagating in an attenuating medium.

$$\nabla^2 p - \frac{1}{c_0^2} \frac{\partial^2 p}{\partial t^2} + \frac{\delta}{c_0^4} \frac{\partial^3 p}{\partial t^3} + \frac{\beta}{\rho c_0^4} \frac{\partial^2 p^2}{\partial t^2} + \frac{1}{\rho} \nabla p \cdot \nabla \rho - \sum_{m=1}^v \xi_m = 0 \quad (5.1)$$

where ξ_m satisfies the equation

$$\dot{\xi}_m + \omega_m \xi_m = a_m \omega_m \frac{\Delta c}{c_0} \nabla^2 p \quad (5.2)$$

The first two terms in Eq. 5.1 represent the linear wave equation, the third term accounts for thermoviscous diffusivity, followed by nonlinearity, variations in density,

and v relaxation mechanisms. Here p is the acoustic pressure, c_0 and ρ are the equilibrium speed of sound and density, δ is the acoustic diffusivity, and β is the nonlinearity parameter. The nonlinear parameter B/A is related to the coefficient, β , by $\beta = 1 + B/2A$ and the diffusivity δ can be expressed as a function of the absorption coefficient α with the equation $\delta = 2\alpha c_0^3/\omega^2$ (where ω is the angular frequency). The material parameters c_0, δ, ρ and β can be functions of space. The relaxation equation (Eq. 5.2) has v peaks at characteristic frequencies ω_m with weight a_m that depend on the particular frequency dependent attenuation law that is being modeled. The change in speed of sound Δc must obey the Kramers-Kronig relation to preserve causality.

5.2.2 Diffraction

Explicit finite differences in the time domain are used to discretize the nonlinear full-wave equation on a three dimensional Cartesian grid. The three dimensional linear wave equation is modeled with a rotated stencil in Cartesian coordinates. Fourth order spatial derivatives were used to minimize the effects of numerical dispersion and reduce the requirements for grid refinement. Higher order discretizations that operate only in the Cartesian directions tend to have unwanted directionality—the wave propagates at different speeds along the direction of discretization compared to directions that are at an angle [103]. This type of error has particular significance for correct focusing and spherical propagation from point scatterers. To minimize this effect, the spatial discretization used here has two rotated stencils in addition to the conventional Cartesian stencil. The total star-shaped stencil for the spatial derivatives is shown below,

5.2.3 Temporal terms and density

The linear temporal derivatives are approximated by second order finite differences.

$$\frac{\partial^2 p}{\partial t^2} \approx \frac{(p_{i,j,k}^{n+1} - 2p_{i,j,k}^n + p_{i,j,k}^{n-1})}{\Delta t^2} \quad (5.4)$$

$$\frac{\partial^3 p}{\partial t^3} \approx \frac{(6p_{i,j,k}^{n+1} - 23p_{i,j,k}^n + 34p_{i,j,k}^{n-1} - 24p_{i,j,k}^{n-2} + 8p_{i,j,k}^{n-3} - p_{i,j,k}^{n-4})}{(2\Delta t)^3} \quad (5.5)$$

The nonlinear term was rewritten as

$$\frac{\partial^2 p^2}{\partial t^2} = 2 \left[\left(\frac{\partial p}{\partial t} \right)^2 + p \frac{\partial^2 p}{\partial t^2} \right] \approx \quad (5.6)$$

$$2 \left[\left(\frac{p^n - p^{n-1}}{\Delta t} \right)^2 + p^n \left(\frac{p^{n+1} - 2p^n + p^{n-1}}{\Delta t^2} \right) \right] \quad (5.7)$$

so the equation can be solved for p^{n+1} directly.

The spatial derivatives in the density term are modeled with a standard fourth order approximation, but because only a first order derivative is being calculated the total width of the spatial stencil remains unchanged. Preserving the stencil width reduces the communication time required by the domain decomposition in the parallelized code, as is described in further detail in the discussion. The discretization is shown here for the ρ derivative in the x-axis

$$\frac{\partial \rho}{\partial x} \approx \frac{-\rho_{i-2} + 8\rho_{i-1} - 8\rho_{i+1} + \rho_{i+2}}{12\Delta x} \quad (5.8)$$

5.2.4 Relaxation mechanisms

The v relaxation mechanisms describe the following frequency dependent attenuation

$$\alpha(\omega) = \omega \left[\frac{\sum_{m=1}^v y_m \frac{\omega/\omega_m}{1+(\omega/\omega_m)^2}}{1 + \sum_{m=1}^v y_m \frac{\omega/\omega_m}{1+(\omega/\omega_m)^2}} \right] \quad (5.9)$$

where

$$y_m = \left(\frac{\Delta c}{c_0} \right)^2 a_m \quad (5.10)$$

Each relaxation mechanism has an associated characteristic frequency, ω_m and a fractional change in speed of sound associated with the parameter y_m . If we assume that $\Delta c \ll c_0$, then Eq. 5.9 can be approximated by

$$\alpha(\omega) \approx \omega \sum_{m=1}^v y_m \frac{\omega/\omega_m}{1 + (\omega/\omega_m)^2} \quad (5.11)$$

To fit the relaxation mechanisms to an arbitrary frequency dependent attenuation law the characteristic frequencies, ω_m , are chosen. Then certain discrete frequencies are chosen across a frequency range of interest. Due to the linearity of Eq. 5.11 with respect to y_m these weights can be determined with a straightforward minimization of the mean of the square error between the relaxation mechanisms and the attenuation law. This approach requires selecting characteristic frequencies. A more accurate, and more complex, alternative to this procedure requires the use of a nonlinear minimization routine to explore the parameter space given by both ω_m and y_m and then determine their optimal values. As subsequent results will show, the former method provides sufficient accuracy for the purpose of this paper.

Once the relaxation parameters are established, finite differences are used to discretize Eq. 5.2. A second order in time and fourth order in space discretization is

used

$$\xi_m^{q+1/2} = A_m \xi_m^{q-1/2} + B_m (\nabla^2 p)_{t=n\Delta t} \quad (5.12)$$

with

$$A_m = (2 - \omega_m \Delta t) / (2 + \omega_m \Delta t) \quad (5.13)$$

and

$$B_m = \frac{2y_m \omega_m \Delta t}{(2 + \omega_m \Delta t) (1 + \sum_{m=1}^n y_m)} \quad (5.14)$$

The finite difference scheme for the relaxation attenuation is then

$$\sum_{m=1}^v \xi_m \approx \frac{1}{2} \sum_{m=1}^v (\xi_{m,i,j,k}^{q+1/2} + \xi_{m,i,j,k}^{q-1/2}) \quad (5.15)$$

and

$$\xi_{m,i,j,k}^{q+1/2} = A_m \xi_{m,i,j,k}^{q-1/2} + 2B_m C_{i,j,k} / h^2 \quad (5.16)$$

where $C_{i,j,k}$ represents the spatial discretization of $\nabla^2 p$ described in Eq. 5.3.

5.2.5 Perfectly matched layer

The perfectly matched layer boundary condition is applied to the linear wave equation

$$\nabla^2 p - \frac{1}{c_0^2} \frac{\partial^2 p}{\partial t^2} = 0 \quad (5.17)$$

Each of the six orientations in the stencil described by Eq. 5.3 must be solved separately and have their own independent calculations. This adds considerable complexity to the code, and practically, only the three conventional Cartesian orientations need to be used to obtain a satisfactory absorbing boundary layer, as is demonstrated in subsequent results. In the interest of notational simplicity, we describe here the solution in the z coordinate using the stretched coordinate approach proposed in

Chew and Weedon [22]. The wave equation can then be written in time-harmonic form with the complex-coordinate stretched space

$$\frac{1}{c_0^2}(i\omega^2)\hat{p} = \frac{\partial^2 \hat{p}}{\partial x^2} + \frac{\partial^2 \hat{p}}{\partial y^2} + \frac{1}{s_z} \frac{\partial}{\partial z} \left(\frac{1}{s_z} \frac{\partial \hat{p}}{\partial z} \right) \quad (5.18)$$

where the z coordinate is stretched by

$$s_z = 1 + \sigma_z/i\omega \quad (5.19)$$

Equation 5.18 can be written in the time domain with the aid of the auxiliary variables D_1 and D_2

$$i\omega \hat{D}_1 = \frac{1}{1 + \sigma_z/i\omega} \frac{\partial \hat{p}}{\partial z} \quad (5.20)$$

$$i\omega \hat{D}_2 = \frac{1}{1 + \sigma_z/i\omega} \frac{\partial}{\partial z} (i\omega \hat{D}_1) \quad (5.21)$$

Then the scalar wave equation can be written as

$$\frac{\partial D_1}{\partial t} + \sigma_z D_1 = \frac{\partial p}{\partial z} \quad (5.22)$$

$$\frac{\partial D_2}{\partial t} + \sigma_z D_2 = \frac{\partial^2 p}{\partial z \partial t} \quad (5.23)$$

$$\frac{1}{c_0^2} \frac{\partial^2 p}{\partial t^2} = \frac{\partial^2 p}{\partial x^2} + \frac{\partial^2 p}{\partial y^2} + \frac{\partial D_2}{\partial t} \quad (5.24)$$

These equations can be discretized by deconvolving the second order derivative so that two applications of the first derivative match the second derivative coefficients:

$[b_{-1}, b_0, b_1] * [b_{-1}, b_0, b_1] = [-1, 16, -30, 16, -1]/12$. Then

$$D_{1,i,j,k+1/2}^{n+1/2} = \frac{1 - \sigma_z \Delta t/2}{1 + \sigma_z \Delta t/2} D_{1,i,j,k+1/2}^{n+1/2} + \frac{1}{1 + \sigma_z \Delta t/2} \left(\sum_{m=-1}^1 b_m P_{i,j,k+m}^n \right) \quad (5.25)$$

$$D_{2_{i,j,k+1/2}}^{n+1/2} = \frac{1 - \sigma_z \Delta t/2}{1 + \sigma_z \Delta t/2} D_{2_{i,j,k+1/2}}^{n+1/2} + \frac{1}{1 + \sigma_z \Delta t/2} \left(\sum_{m=-1}^1 b_{-m} D_{1_{i,j,k+m}}^{n+1/2} - \sum_{m=-1}^1 b_{-m} D_{1_{i,j,k+m}}^{n-1/2} \right) \quad (5.26)$$

where to single floating point precision

$$b_{-1} = -1.077350269189626 \quad (5.27)$$

$$b_0 = 1.154700538379252$$

$$b_1 = -0.077350269189626$$

In Eq. 5.26 note the minus sign in b_{-m} to preserve the convolution ordering. The PML is sensitive to small variations and the numerical derivatives in the limiting case of $\sigma_z = 0$ must match the derivatives in non-absorbing region. The field parameters D_1 and D_2 do not have a particular physical meaning and are only used for their numerical convenience. The diffraction term in Eq. 5.17 can then be discretized as

$$\nabla^2 p_z \approx \quad (5.28)$$

$$\left[C_{i,j,k}^n - (-p_{i,j,k-2}^n + 16p_{i,j,k-1}^n - 30p_{i,j,k}^n + 16p_{i,j,k+1}^n - p_{i,j,k+2}^n)/12\Delta z^2 \right] + \left(D_{2_{i,j,k+m}}^{n+1/2} - D_{2_{i,j,k+m}}^{n-1/2} \right) / \Delta z^2 \quad (5.29)$$

The conductivity profile of the PML is given by

$$\sigma_z(z) = - \left(\frac{z}{d} \right)^m \frac{c_0(m+1) \ln(R_0)}{2d} \quad (5.30)$$

where d is the thickness of the PML, m is the order, and R_0 is the reflection of the PML at normal incidence. These parameters are optimized with respect to the number of matching layers and the frequency of the incident wave.

5.2.6 Hydrophone measurements

Prior to making measurements, a membrane hydrophone (Onda Corp, Sunnyvale, CA) was placed in deionized water for thirty minutes. A Siemens Antares ultrasound scanner (Siemens Medical Solutions USA, Inc., Issaquah, WA) was then set up to repeatedly fire the center beam of a VF10-5 transducer (Siemens Medical Solutions USA, Inc., Issaquah, WA) at about 100Hz PRF using a two cycle apodized pulse at 7% of its maximum power. The center of the hydrophone was placed at the 20 mm focus of the transducer. A two dimensional acquisition was performed with a Newport MM3000 (Newport Corporation, Irvine, CA) translation stage to move the transducer in increments of 0.1mm laterally and in elevation. The translation stage has a precision of $0.1\mu\text{m}$. A 5mm by 5mm grid was recorded, with 5 waveforms being acquired at each spatial location using a trigger from the ultrasound scanner. Once this acquisition was completed, the transducer was lowered 16.5mm and another two dimensional acquisition with a fixed axial position (10mm by 10mm) was performed with the same parameters. Voltage was converted to pressure according to the conversion factor provided by the manufacturer's frequency based calibration.

Basic filtering and averaging were used to remove noise from the data. A 0.3 mm spatial low pass filter was used in the lateral-elevation plane before averaging the five independent acquisitions. Additionally, the initial condition data obtained from the transducer face was band-pass filtered with a 200% bandwidth Gaussian filter centered at the transducer's 6.67 MHz pulse frequency.

5.2.7 Field II

The linear non-attenuating algorithm was compared to an equivalent Field II [60] simulation for a commercial linear transducer. Field II solves the wave equation with

the Topholme-Stepanishen method for calculating linear pulsed ultrasound fields in a homogeneous medium [101, 102, 117]. It has been widely validated and is commonly used to model transducers.

The transducer modeled in the Field II simulations is consistent with linear transducers made commercially. The array had an elevation focus of 2 cm, a lateral focus of 2.4 cm, an $F/\#$ of 1.5, and a center frequency of 4.2 MHz. The transducer was modeled to match the proposed algorithm, meaning the kerf was set to zero and an element size of $20 \mu\text{m}$ by $20 \mu\text{m}$ was used to model an active aperture size of 16 mm by 5 mm. The number of mathematical elements used for each $20 \mu\text{m}$ by $20 \mu\text{m}$ was set to 1. The soft baffle boundary condition was used in the Field II simulation, and a parabolically focused profile was used in both the lateral and elevation dimensions,

$$p(x, y, z = 0) = p_0 f(t + x^2/2c_0d_x + y^2/2c_0d_y) \quad (5.31)$$

where p_0 is the pressure amplitude, d_x is the lateral focus, d_y is the elevation focus and f is the impulse function:

$$f(t) = e^{-(\omega_0 t/n\pi)^{2m}} \sin(\omega_0 t) \quad (5.32)$$

Here the number of cycles, n , was set to 1.667 so that the fractional bandwidth was approximately 0.6, and the exponential drop-off parameter, m , was 2.

In addition, the angular response of the transducer elements was negated by applying an apodization of

$$\theta = \tan^{-1}(x/z); \quad (5.33)$$

$$\text{apod}_{\text{lat}} = \text{sinc}(a_x \sin(\theta)/\lambda) \cos(\theta) \quad (5.34)$$

in the lateral and elevation dimensions. The element width is given by a_x . The

proposed algorithm does not apply an angular weight to the transducer elements. A sampling frequency of 160 MHz was used in the Field II simulation.

5.3 Results

5.3.1 Stencil parameters

The stencil parameters, γ and η , were calculated by comparing the linear inviscid part of the algorithm ($\beta = \delta = 0$) to the analytic solution for an oscillating point source in a homogeneous medium [73]. A 2 MHz oscillator was placed in the center of a $1.5 \text{ cm} \times 1.5 \text{ cm} \times 1.5 \text{ cm}$ grid with $\Delta x = \Delta y = \Delta z = 18 \mu\text{m}$ and the time step was set to 2.3 ns. The material parameters are $c_0 = 1540 \text{ m/s}$ and $\rho = 1000 \text{ kg/m}^3$. To avoid edge effects, the spherical wave was allowed to propagate until it just reached the boundaries, then the stencil parameters were varied until the L^2 numerical error was minimized. These were found to be $\gamma = 0.025$ and $\eta = 0.005$ and these values are used in the remainder of this paper.

5.3.2 Relaxation mechanisms

The relaxation parameters were calculated using a two parameter model for attenuation laws in tissue and water. In tissue the attenuation was modeled with an f^1 frequency dependence and an attenuation of 0.7 dB/MHz/cm. In water the frequency dependence is f^2 with an attenuation of 1.7000e-04 dB/cm at 0.5 MHz. The parameters were calculated by minimizing the error for a frequency range between 0.5 and 12 MHz using the approximation that $\Delta c \ll c_0$, as described previously. The plots below show the ideal attenuation law and the fitted relaxation mechanism for tissue (on the left) and water (on the right). Two parameters, $q = 2$, were sufficient

to obtain an excellent fit with the relaxation models across the wide frequency band. Table 5.1 shows the relaxation parameters used to fit the relaxation models to the attenuation laws.

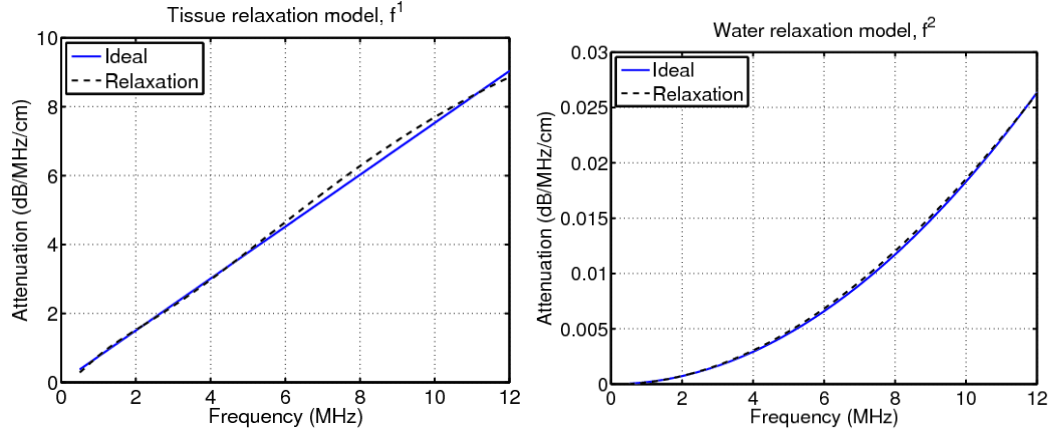


Figure 5.2: Relaxation model for frequency dependent attenuation laws in tissue (left) and water (right). A two parameter model is sufficient to closely fit the attenuation laws across a wide frequency range.

	y_1	ω_1 (rad/s)	y_2	ω_2 (rad/s)
Tissue	0.00337039	$2\pi \cdot 1e6$	0.0033757	$2\pi \cdot 10e6$
Water	$2.5312e-5$	$2\pi \cdot 0.1e6$	$-0.08215e-5$	$2\pi \cdot 50e6$

Table 5.1: Relaxation parameters

5.3.3 Perfectly matched layers

The conductivity profile of the PML was optimized for 40 and 100 matching layers for a 2.4 MHz center frequency, as shown in Table 5.2. A planar ultrasonic pulse was transmitted through a homogeneous non-attenuating medium at a normal angle to the absorbing layer and the amplitude of reflected wave was measured. Figure 5.3 shows the incident (left) and reflected (right) pulses for an absorbing boundary layer with 100 layers or a thickness of 1.25 mm. Even though the layer is thin, the amplitude of

the reflected pulse is reduced by close to four orders of magnitude. A 0.5 mm layer reduces the reflected energy by over three orders of magnitude. Much like a physical absorbing layer, the reflected wave has a lower frequency content indicating that a further measured reduction of the energy would occur when it is filtered through the pass-band of an ultrasonic transducer. In the subsequent simulations the 40 layer boundary condition is used at the sides of the domain, which is reached by the diffracted edges of an ultrasound pulse, and 100 layers are used at the bottom surface, where the more intense pulse center is absorbed.

Num. Layers	Thickness	Reflected energy	m	R_0
40	0.5 mm	-63.2 dB	2	1e-5
100	1.25 mm	-78.9 dB	3	1e-7

Table 5.2: Conductivity profiles

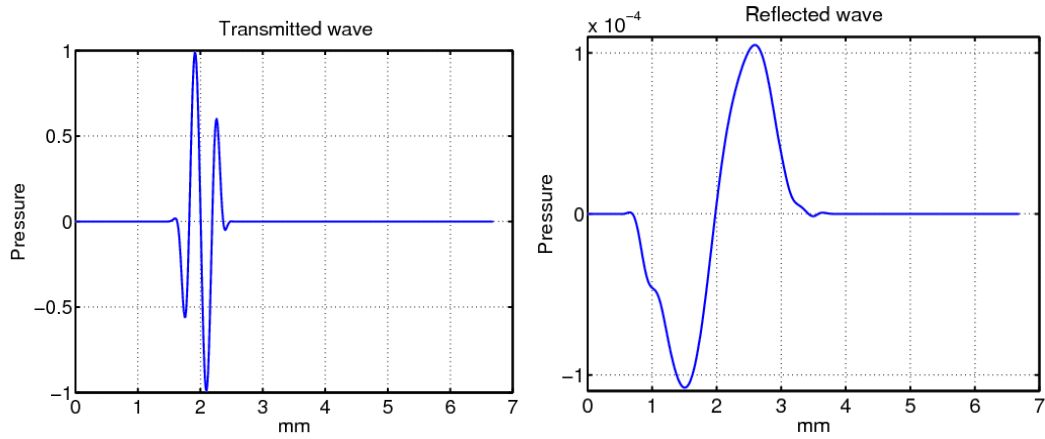


Figure 5.3: Transmitted and reflected waves from the perfectly matched layer with 100 layers (or a 1.25 mm thickness). Values are normalized to the transmitted amplitude.

5.3.4 Clinical transducer in a linear homogeneous non-attenuating medium

The linear non-attenuating algorithm was compared to an equivalent Field II simulation for a commercial transducer. Field II solves the wave equation with the Tupholme-Stepanishen method for calculating linear pulsed ultrasound fields in a homogeneous medium [101, 102, 117]. It has been widely validated and is commonly used to model transducers.

The transducer used in the following simulations is a Siemens VF10-5 linear array (Siemens Medical Solutions USA, Inc., Issaquah, WA) with 192 elements, a 2 cm elevation focus, 2.4 cm lateral focus, an F-number of 1.5, and a 4.2 MHz center frequency. The element dimensions are 0.201 mm width and 5 mm height. For the purposes of the simulations the element kerf was assumed to be negligible. The simulation parameters were kept as described above except for the grid size, which was altered to 1.5 cm laterally, 1 cm in elevation, and 3.35 cm in depth, on the positive quadrant of the lateral-elevation plane.

Figure 5.4 compares the intensity of the acoustic field for the Field II and FDTD nonlinear full-wave simulations across the lateral plane. The agreement is good throughout the simulated region. There are small visible differences, notably the -6 dB contour is approximately 1 mm more proximal to the transducer face in the nonlinear full-wave simulation and the -20 dB contour is slightly narrower at shallow depths ($z < 1.5$ cm). However, the overall morphology of the contours is very close.

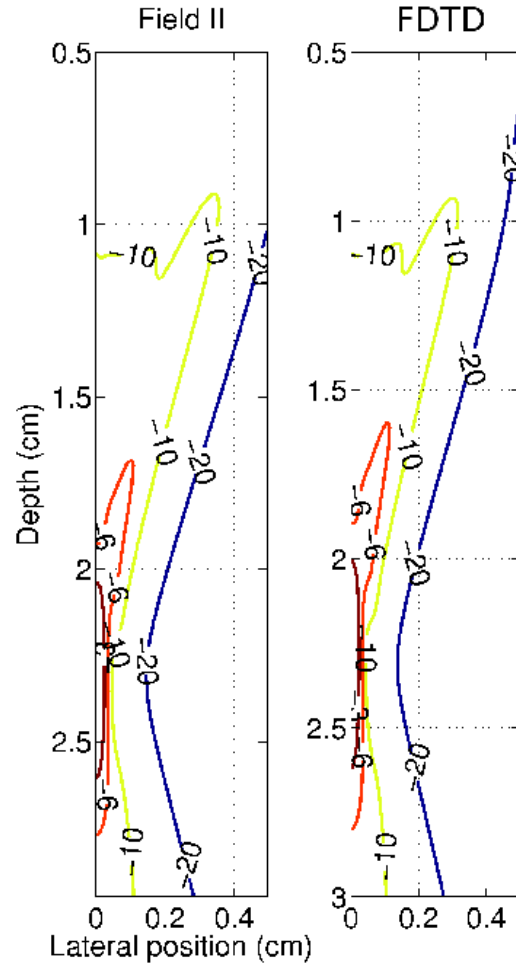


Figure 5.4: A comparison of the intensity of the acoustic field as calculated by Field II and the linear inviscid FDTD nonlinear full-wave method for a commercial clinical ultrasound transducer. The lateral plane is shown.

The lateral beamplot at the focus is shown in Fig. 5.4. The width and shape of the main lobe is almost indistinguishable between the two simulations. The height of the side lobe is slightly larger (< 0.2 dB) for the nonlinear full-wave simulation. Beyond 1 cm laterally the difference between the two simulations is less than 0.3 dB.

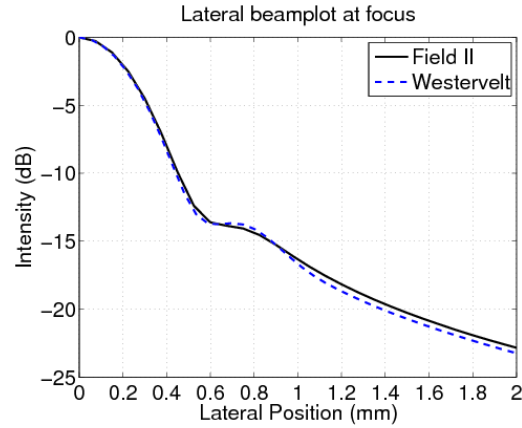


Figure 5.5: A comparison of the lateral beamplot at the focus for the Field II and the linear inviscid nonlinear full-wave simulations.

The agreement between simulations for the axial intensity, shown in Fig. 5.6, is also very good. There is a small difference in the calculations at the hump preceding the focal region ($z=1.6$ cm) and the nonlinear full-wave simulation predicts a slightly wider (< 0.2 mm) focal region.

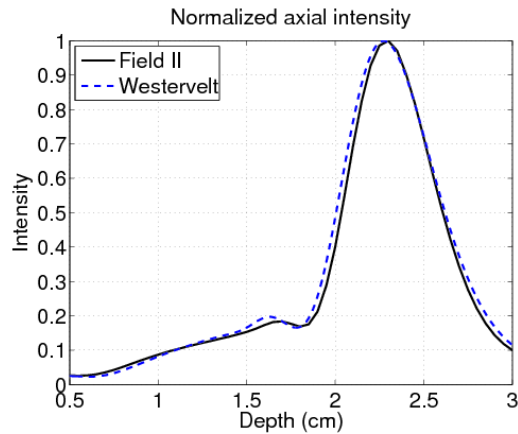


Figure 5.6: A comparison of the axial intensity for the Field II and the linear inviscid nonlinear full-wave simulations.

5.3.5 Nonlinear plane wave

Results from the inviscid FDTD nonlinear full-wave simulation were compared to the results from the Galerkin method applied to the inviscid Burgers' equation [85]. Burgers' equation is a nonlinear hyperbolic partial differential equation that in acoustics can be written as

$$\frac{\partial p}{\partial z} = \frac{\beta}{2\rho c_0^3} \frac{\partial p^2}{\partial t'} \quad (5.35)$$

where $t' = t - z/c_0$ is the retarded time. The use of transformed coordinates shifts the small signal phase speed of the wave to zero. Therefore changes in pressure from Eq. 5.35 are due entirely to nonlinearity and not propagation effects. Solutions of the Burgers' equation can be compared to solutions of an inviscid plane wave propagating with the FDTD nonlinear full-wave algorithm because the transverse components of the Laplacian operator in Eq. 5.1 are zero. Thus the solutions are mathematically equivalent for one-way waves but numerically different. Unlike the time domain method used to solve the nonlinear full-wave equation, the Galerkin technique solves Eq. 5.35 in the frequency domain. The details of the implementation are omitted here but can be found in [85].

Figure 5.10 shows a 2 MHz plane wave with $\beta = 5$, $p_0 = 1.5$ MPa after it has propagated a distance of 2 cm. This distance is approximately one quarter of the theoretical plane wave shock formation distance for a sinusoidal wave. The initial waveform is a 1.677 cycle pulse with an exponential drop-off, m , of 2 and is shown as a solid line. The dashed line represents the wave as calculated by the Galerkin method after it has propagated 2 cm and the dash-dotted line is the FDTD nonlinear full-wave calculation.

In the time domain (the left graph in Fig 5.10), the simulations are practically

indistinguishable. In the frequency domain (right graph of Fig. 5.10) there is excellent agreement at the fundamental and second harmonic frequencies. At the third harmonic there is a 1.2 dB difference between the peaks and at the fourth there is a 2.5 dB difference.

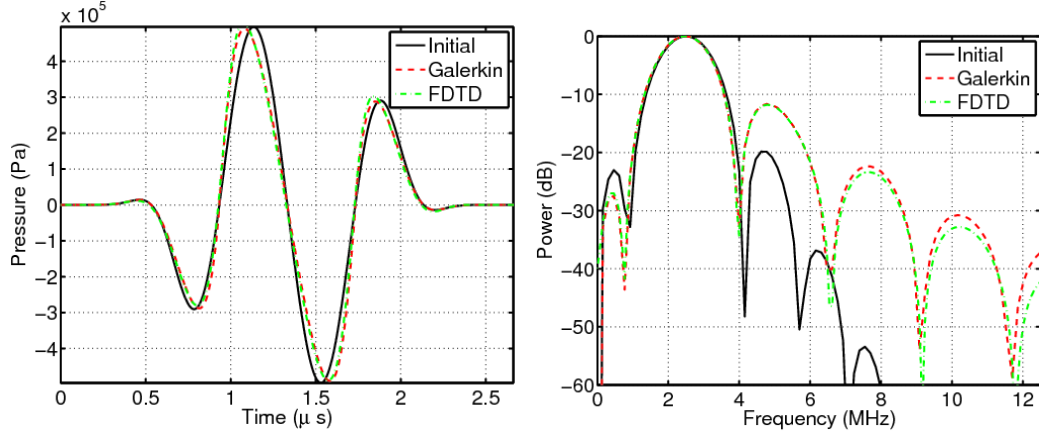


Figure 5.7: Nonlinear propagation of a plane wave as calculated by the FDTD nonlinear full-wave algorithm and the Galerkin scheme. A time domain waveform is shown on the left and the power spectrum is shown on the right.

5.3.6 Experimental verification

The acoustic plane at the transducer face was measured and used as an input to the full-wave simulation with the acoustic properties of water. Shown on the left of Fig 5.8 are the experimentally measured point spread functions for the fundamental (top) and harmonic (bottom) fields. The equivalent plots are shown for the simulated data with the experimentally determined initial conditions on the right. A Gaussian bandpass filter with a 100% bandwidth was used to filter the fundamental and harmonic components. The point spread function was calculated as the temporally averaged intensity on a normalized dB scale.

There is an excellent agreement between the experimental and simulated funda-

mental PSFs in terms of primary and secondary features. The size and position of the mainlobe are very similar and the initial off-plane position of the transducer is apparent in the measured and simulated data sets. The elevation and lateral sidelobes also have similar position and amplitude. Features that are less than 35 dB down from the peak or off axis with respect the lateral and elevation planes exhibit a close correspondence even though there is a visible amount of noise in the experimental data. Sections of the lateral and elevation beamplots shown in Fig. 5.9 provide a more quantitative visualization of the differences. The mainlobe of fundamental lateral beamplot is almost identical to the measured values. The sidelobes and data below -25 dB exhibit a small discrepancy of about 1-2 dB. The elevation beamplots remain above -25 dB throughout the considered range and they are visually indistinguishable from each other.

The harmonic PSFs shown in the bottom of Fig. 5.8 have similar primary features and many of the secondary features are distinguishable even though the noise floor of the experimental data limits the accuracy of the comparison in the sub -30 dB range. The mainlobe position and size shows good agreement and the elevation sidelobes have the same position and amplitude even though they appear to be blurred into the mainlobe for the experimental data. The lateral sidelobes can be seen peeking through the noise floor in the same locations as the simulated data. Beamplots at the bottom of Fig. 5.9 show that in the elevation plane the mainlobe matches the experimental data up to -30 dB and in the elevation plane there is a close match with a 5% error at the full width half maximum (FWHM). The position of the secondary lobes is accurate though there is a discrepancy of less than 4 dB in the magnitude.

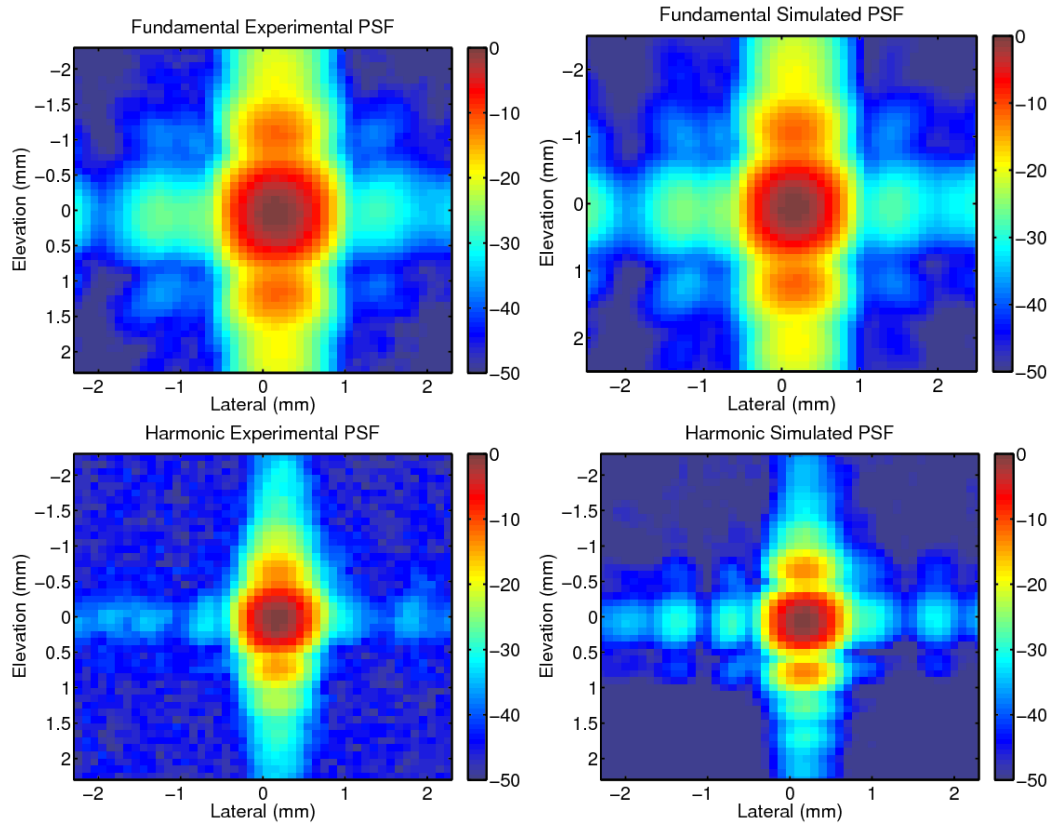


Figure 5.8: Experimental (left) and simulated (right) PSFs for the fundamental (top) and harmonic (bottom) beams.

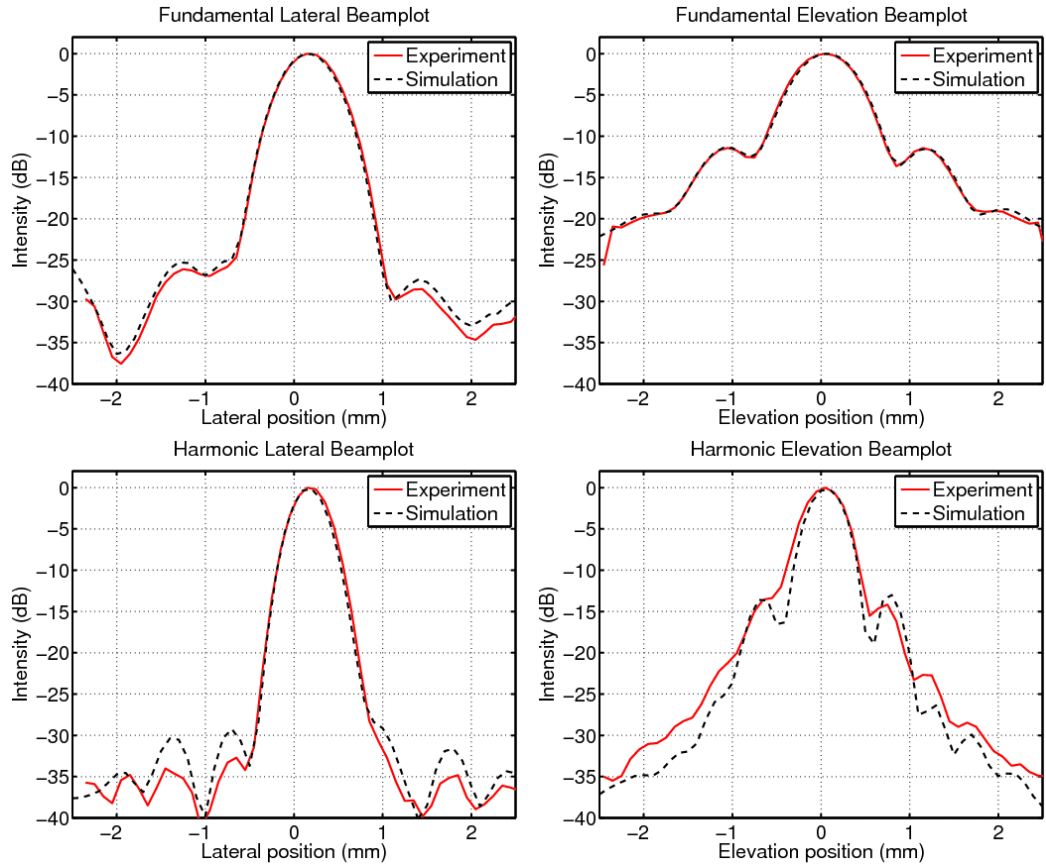


Figure 5.9: A comparison of measured (solid) and simulated (dashed) lateral (left) and elevation (right) beamplots for the fundamental (top) and harmonic (bottom) PSFs shown in Fig. 5.8.

A comparison of the experimental and simulated power spectra at the focal point is shown in Fig. 5.10. The fundamental power spectra at 6.67 MHz are indistinguishable and there is a 1 dB or less difference for the harmonic power spectra at 13.3 MHz. There is a slightly larger difference in the power spectra for frequencies in between the fundamental and harmonic power bands but it is limited to a narrow frequency range centered at 10 and 12 MHz.

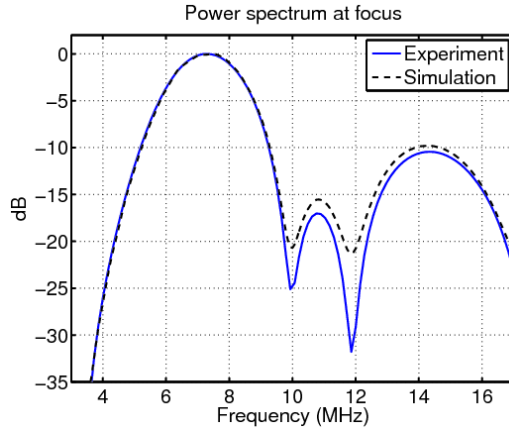


Figure 5.10: A comparison of the experimental (solid) and simulated (dashed) power spectrum at the focus.

5.3.7 Ultrasonic imaging

A focused ultrasonic pulse was propagated through a two dimensional heterogeneous tissue model with twelve point scatterers per resolution. The initial pulse had an amplitude of 0.5 MPa and was spherically focused at 5 cm from an unapodized transducer with an F-number of 1.5. Its center frequency was 2.1 MHz with a 67% bandwidth. The tissue representation was obtained from a histologically stained cross section of the human abdominal wall and then scanned on a digital flatbed scanner at 300 d.p.i. A combination of automatic and manual digital image processing was used to segment the images into tissue maps. The structures in the tissue were correlated with their measured properties of which the speed of sound is shown on the right of Fig. 5.11. As shown in Table 5.3 there are variations in speed of sound, attenuation, density, and nonlinearity. Subcutaneous fat lobules and fatty structures within muscle layer are included in the “fat” category. Various muscle groups are combined in the “muscle” category. Skin septa within the subcutaneous fat, tendon, the peritoneum, and connective fasciae are associated with the “connective tissue”

category. The point scatterers have a $40 \mu\text{m}$ diameter and a random spatial and amplitude variation with a mean variation in the speed of sound of 77 m/s , which corresponds to a 5% variation of the accepted average tissue velocity of 1540 m/s . The pressure field at the focus (5 cm) is shown on the right side of Fig. 5.11 on a compressed scale to emphasize small amplitude features such as those occurring from reflection, reverberation, and scattering.

Tissue	B/A	α (dB/MHz/cm)	c_0 (m/s)
Fat	9.6	0.40	1479
Muscle	8.0	0.15	1550
Connective	8.0	0.68	1613
Liver	7.6	0.50	1570

Table 5.3: Acoustic parameters for tissue

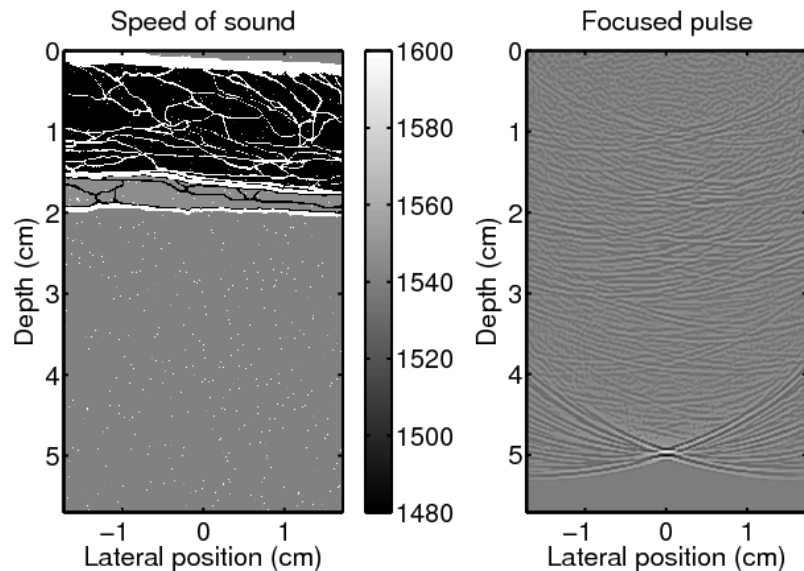


Figure 5.11: On the left, a graphical representation of the variation in the speed of sound for the abdominal layer (not shown are spatial variations in attenuation, nonlinearity, and density). On the right, the acoustic field of a diagnostic pulse at the focus (scale is compressed to emphasize small amplitudes).

A circular anechoic region with a 5 mm diameter was placed at the focus to mimic a lesion. To simulate an ultrasonic imaging system, a focused pulse was transmitted

and allowed to propagate. The resulting reflections were measured and a standard constant F-number delay and sum beamforming algorithm was used to create a single A-line. The process was repeated by translating the transducer and forming a series of A-lines that are shown as fundamental (left) and harmonic (right) B-mode images in Fig. 5.12. A 100% bandwidth bandpass filter was used to obtain the fundamental and harmonic components from the raw data. No point spread function assumptions were used to form the images.

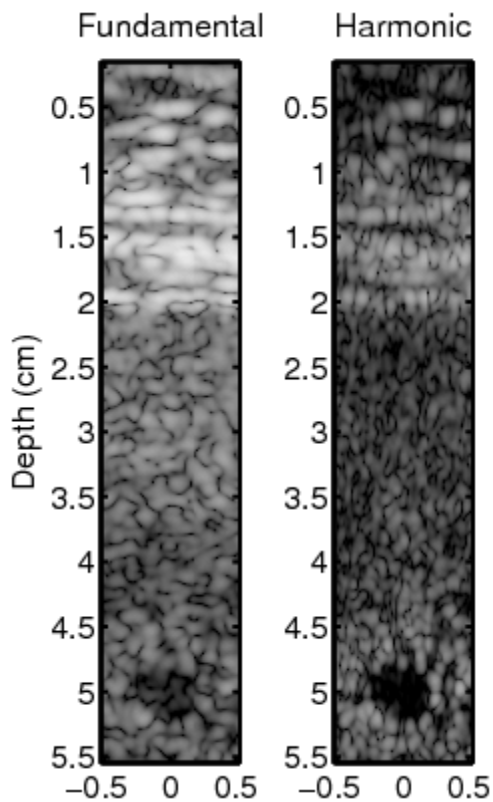


Figure 5.12: Simulated fundamental (left) and harmonic (right) ultrasound images of an anechoic region below an abdominal using a transmit-receive beamformation process.

In a second, related, application the transmit receive point spread functions were calculated for the same ultrasonic pulse propagating through the tissue layer but

without the spatially distributed scatterers. A single point scatterer was placed at the focus and beamforming was used to obtain the fundamental and harmonic point spread functions shown on the left of Fig. 5.13. All other material and pulse parameters were kept unchanged from the previous description. The plots on the right of Fig. 5.13 were obtained by subtracting the reverberation from the near-field layer from the original fundamental and harmonic PSFs. This reverberation PSF was calculated by removing the point target at the focus and using only the reflections from the abdominal layer in the beamforming process.

The plots of the PSFs have four distinct regions of interest: the “X” shaped portion spanning the image, representing a conventional PSF if it did not incur any degradation; the lateral regions within the isochronous volume to the left and right of the “X”; the region above, that precedes the pulse temporally; and the region below, that trails it. The fundamental PSF has a substantial amount of clutter written into all these regions whereas the harmonic PSF is degraded primarily in the isochronous volume, to a lesser extent in the trailing region, and even less in the preceding region. When the reverberation clutter is linearly subtracted from the original PSF there is a marked improvement in the fundamental PSF. All of the clutter in the preceding region is removed, there is a substantial reduction in the trailing region, and there is an improvement in the isochronous volume. In the harmonic PSF the clutter in the preceding region is also removed but because the original harmonic PSF does not have much clutter there to begin with the improvement is comparatively smaller. There is not an easily discernible improvement in the remaining regions.

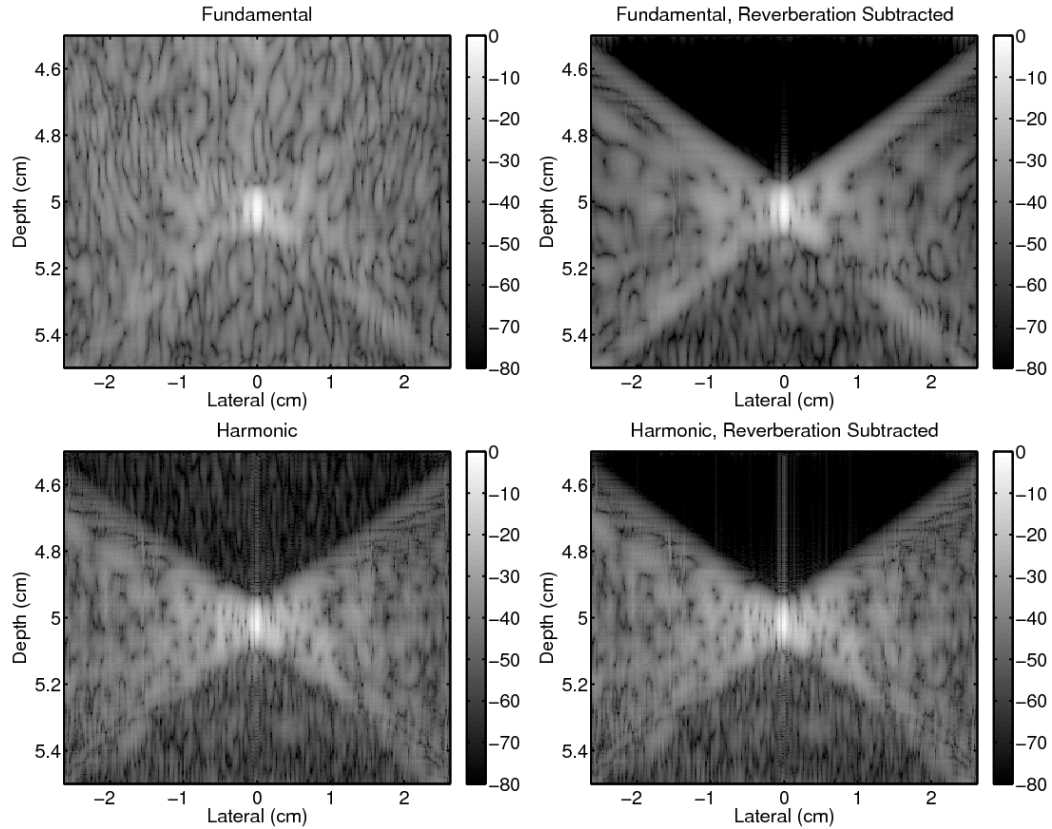


Figure 5.13: Point spread functions with clutter from propagation through a representation of the abdominal wall. The fundamental (top) and harmonic (bottom) PSFs are shown without any processing (left) and with reverberation clutter removed (right). The axes are not geometrically proportional.

5.4 Discussion

5.4.1 Computation

The algorithm uses fourth order finite difference discretizations in space and second order discretizations in time that were solved explicitly in the time domain. Due to the fine discretization and the use of three spatial dimensions the memory and processing requirements were demanding. More than 10^9 physical grid points and

more than 10^{13} spatio-temporal points are calculated for each three-dimensional simulation. To distribute the memory and computational requirements custom parallel code was written with version 7.0.6 of the LAM/MPI toolkit using a combination of C and Fortran77. This code runs on a dedicated 56 processor Linux cluster with 64 bit architecture and 112 GB of RAM.

The overall spatial stencil for the entire method was kept at five points per dimension which, with the one dimensional domain decomposition used in the parallelization, required communication of a laterally two point wide axial-elevation volume per processor per domain boundary. These extensive internode communication requirements were negotiated with a private gigabit network using jumbo frames on a SMC8748L2 switch. The system runs CentOS 4, a free version of Red Hat Enterprise Linux 4. The three dimensional simulations presented in this paper required approximately 32 hours of run time and 90 GB of memory.

5.4.2 Perfectly matched layer

In the PML literature it is common to treat the interior of the domain, where there are no absorbing layers, as an extension of the PML's with the stretched coordinate set to 1 [22, 70]. To improve the memory requirements, here the interior is treated separately and only the boundary elements have the increased memory requirements associated with the PML. For large simulations, such as those presented in this paper, the boundaries represent a small fraction of the total simulation therefore the added memory requirement of the PML is practically negligible and grows only marginally with an increase in the domain size.

One of the advantages of using PML's compared to conventional methods such is that the amount of absorption can be increased by simply adding extra layers. There

is, however, a point of diminishing returns, for example an increase from 40 to 100 layers reduced the reflected amplitude from -63.2 dB to -78.9 dB, a 24% change.

An 80 dB reduction in reflected energy is low enough to satisfy demanding ultrasound applications, such as those requiring clutter or reverberation measurements, and is much better than typical results from water tank setups with absorbing media on the walls.

5.4.3 Nonlinear plane wave

Propagation of a nonlinear plane wave and comparison with the Galerkin solution of Burgers' equation shows the accuracy to within 2.5 dB of the FDTD method up to four times the fundamental frequency. An accurate representation of the higher frequencies is particularly important for thermal simulations where the amount of energy deposition is related to the frequency dependent absorption and is more heavily dependent on higher frequencies. There is no distinguishable error in the power spectrum estimate for the second harmonic, which has particular significance for harmonic imaging. Frequencies beyond the second harmonic are normally outside of the transducer's pass band and do affect imaging applications.

5.4.4 Experimental verification

The experimental verification ties together the effects of diffraction, nonlinearity, and, to a lesser extent, frequency dependent attenuation, which had previously examined independently. The results indicate that the nonlinear full-wave FDTD simulation can take a measured apodized focused ultrasonic field at the transducer face and accurately reproduce the acoustic field at the focus for both the fundamental and harmonic components. Even fine characteristics that are 30 dB below the

mainlobe and focal errors in the original pulse can be seen in the simulated results. The excellent agreement between between the simulated and experimentally determined power spectra at the focus, support the previous spectral results for plane wave propagation.

5.4.5 Ultrasonic Imaging

The previous verifications of the simulation established confidence in our ability to simulate realistic ultrasonic fields in homogeneous media. However, the intended application of the simulation is for heterogeneous media where our ability to verify the results is limited. The heterogeneous results were presented based on the strength of prior verification steps.

When an ultrasound pulse propagates through an *in silico* representation of a measured section of human abdominal wall it exhibits the expected complex characteristics associated with heterogeneous propagation. In the multimedia file (not shown here) the pulse can be seen reflecting from the layers in the abdominal wall. As the pulse emerges the spherical profile of reflections from the point scatterers become apparent. Some of the energy reaches the boundary where there is no discernible reflection from the wall. The pulse becomes progressively tighter as it reaches the focus at 5 cm. Meanwhile acoustic energy continues to reverberate in between the layers of the abdomen and there is a discernible step in the amplitude of the reverberating acoustic field that follows integer multiples of the abdominal depth. Finally the pulse is completely absorbed by the distal boundary and only the reverberated energy persists in the simulated region. Although it is not discernible in the movie, the propagation occurs nonlinearly and with frequency dependent loss.

The simulated ultrasonic images shown in Fig. 5.12 exhibit characteristic dif-

ferences between conventional and harmonic imaging. In the harmonic image the anechoic lesion at 5 cm has better contrast to noise ratio and better boundary definition. The abdominal layers in the fundamental image are comparatively brighter indicating that proportionally more fundamental energy is reflected from them than harmonic energy, which is consistent with the fact that a certain propagation distance is required for harmonic energy to develop and accumulate.

The clutter point spread function images shown in Fig. 5.13 provide a more comprehensive picture of the mechanisms for harmonic image quality improvement. When the clutter PSFs are subtracted from the original PSFs there is a marked improvement in the fundamental PSF but only a marginal improvement in the harmonic PSF. This provides strong supporting evidence that reverberations from near-field layers are a substantial source of image quality degradation for fundamental imaging but not for harmonic imaging. Energy at harmonic frequencies has not yet developed in the near-field therefore there isn't enough reverberation at those frequencies to degrade the image.

The clutter simulations also demonstrate the capabilities of the simulation in a numerically demanding situation. An 80 dB dynamic range is achieved in the fundamental plots in Fig. 5.13 and, preceding normalization, an additional 10 dB is shown in the harmonic plots. A small amount of numerical noise is visible as striations in the center of the harmonic reverberation subtracted image, and to a lesser extent in the fundamental image, but overall there are very few numerical artifacts. There are no discernible reflections, which would be visible where the "X" meets the lateral boundaries (note that these images were not cropped laterally, and the edge of the image corresponds to the lateral boundary of the domain).

5.5 Summary and Conclusions

We have introduced a finite difference time domain algorithm that solves the nonlinear attenuating full-wave equation in three spatial dimensions. The numerical method propagates nonlinear diagnostic ultrasound waves in an heterogeneous attenuating medium with boundary conditions that reduce reflections to negligible levels. The entire acoustic field is simulated so the effects of reflection, reverberation, multiple scattering, and clutter can be accurately modeled and an arbitrary acoustic source can be placed anywhere in the three dimensional simulated field. In the simulations presented heterogeneities in the nonlinearity, attenuation, density, and speed of sound can be modeled with a resolution of $12.5 \mu\text{m}$.

The numerical solutions were verified extensively. Diffraction, or the linear wave term, was verified with Field II, a simulation package that is considered a standard in linear transducer modeling, and with water tank measurements. Differences between the two simulations were less than 0.3 dB across the considered acoustic field. Comparisons of the measured and simulated focal plane of a diagnostic ultrasound transducer exhibited the same primary and secondary features with respect to the position and amplitude of the mainlobe and sidelobes for both the fundamental and harmonic components. A comparison of the power spectrum at the focus also showed excellent agreement. The nonlinear propagation was also verified numerically with results from the Galerkin method for a propagating plane wave and were shown to be agreement to within 2.5 dB up to four times the fundamental frequency. There is negligible disagreement if only the fundamental and harmonic frequencies are considered.

We demonstrated the code's ability to propagate sound through heterogeneous media by transmitting an ultrasound pulse through a measured representation of

human abdominal wall. There is no easy way to verify heterogeneous propagation but the acoustic field qualitatively exhibited the expected behavior as it scattered, reflected, reverberated, focused, and distorted nonlinearly.

The method's capabilities were demonstrated by creating fundamental and harmonic ultrasonic images *in silico* through the same physical process used in a diagnostic scanner: a series of pulses were transmitted through a heterogeneous scattering medium and the received acoustic field at the transducer plane was used in a beamforming algorithm. The resulting harmonic image exhibited the characteristic improvement in lesion boundary definition and contrast. To determine a mechanism for the image quality improvement the point spread functions for these images were calculated and it was shown that reverberation clutter degrades the fundamental image to a much larger extent than the harmonic image.

This simulation has the potential to investigate harmonic imaging in heterogeneous media not just for clutter, but also from the perspective of distributed or near-field phase aberration, beamformation, tissue structure and properties, scatterer distribution, and for novel transducer geometries. Although not presented here, in addition to imaging applications the simulation can, for example, output the complete spatio-temporal loss field as calculated from the relaxation mechanisms which has particular applications for acoustic radiation force or tissue heating.

5.6 Acknowledgments

We would like to thank Joshua Baker-LePain for technical support with the computer cluster and T. Douglas Mast for providing the histological data for the human abdominal wall. This work was supported by NIH grants R01-HL075485 and R01-CA114093.

Chapter 6

Sources of image degradation in fundamental and harmonic ultrasound imaging

The work presented in this chapter is in preparation for IEEE Transaction on Ultrasonics, Ferroelectronics, and Frequency Control [92].

6.1 Introduction

As an ultrasonic wave propagates through tissue, the heterogeneous composition of the medium aberrates the phase and amplitude, generates multiple reflections, lengthens the pulse and degrades the resolution and contrast of an ultrasonic scanner. This paper presents a quantitative evaluation of the relative contributions of various sources to ultrasonic image quality degradation. These three mechanisms of image degradation are examined in detail with simulations of linear and nonlinear pulse propagation in a heterogeneous medium.

Significant reflections occur at interfaces with large impedance mismatches, such as fat and muscle [126]. Tissue with a layered structure is an acoustic environment that is conducive to trapping energy from the propagating ultrasonic pulse with multiple reflections. As the captured energy bounces in between layers, a portion of it is transmitted through the tissue back to the ultrasonic transducer where it overlays acoustic noise to its received signals. If the tissue layers have a distinct periodicity, the noise is visible in the ultrasonic image as brighter bands that occur at integer multiples of the spatial period. For example, this can be commonly observed in fetal imaging

due to the high impedance tissue-amniotic fluid interface. If there is no periodicity the image degradation occurs uniformly, as might occur in a high body mass index patient where there are multiple fat, muscle, and connective tissue layers. In this paper this type of noise, from reflections in the tissue, is referred to as reverberation clutter. It degrades the imaging system's PSF homogeneously, as would be expected of a noise source that has an approximately uniform spatio-temporal distribution within the PSFs characteristic extent.

The nonlinearity of wave propagation is used to the advantage of diagnostic scanners that use the harmonic components of the ultrasonic signal to improve the resolution and penetration of clinical scanners [59, 110, 116]. In terms of image quality, harmonic imaging has been shown to have an important effect in reducing phase aberration and clutter [99, 121, 123]. It has been hypothesized that harmonic imaging can circumvent reverberation clutter as a mechanism for image degradation because it has a low amplitude in the near field where most of the reverberations occur [16]. There is therefore comparatively much less energy at the harmonic frequency that is trapped in the layers with the ability to add uniform acoustic noise to the received signals.

A second mechanism of image quality degradation is due to reflections that, instead of being transmitted towards the transducer face are, transmitted in the direction of pulse propagation adding a long tail low amplitude tail to the originally compact pulse. This effect, which is referred to as pulse lengthening, in addition to adding clutter also degrades the axial resolution. Harmonic imaging can reduce this type of degradation if it is generated in the near field at the fundamental frequency because it is low amplitude and therefore not as susceptible to nonlinear distortion as the main pulse when it reaches the focus. Most of the energy in the pulse tail will thus remain in the fundamental frequency with propagation and will not appear in

the harmonic image.

The final mechanism of image degradation considered in this paper is a result of beamforming errors due to variations in acoustic velocity. In soft tissue, for example, the speed of sound in fat is 1460 m/s and in muscle it is as high as 1610 m/s [49, 50]. When the acoustic velocity of tissue is inhomogeneous across the pulse wavefront parts of it travel faster or slower introducing aberrations in the ideally focused phase profile. An equivalent time delay in the aberration has a more significant effect on a higher frequency pulse because the phase aberration is larger. Variations in attenuation also cause aberrations in the amplitude. It has been shown with theoretical and *in vivo* studies that the defocusing effect of the phase aberrations increases the width of the mainlobe and raises the level of the sidelobes, which reduces the resolution and contrast [39, 54, 81, 114, 118, 135]. The degradation of the PSF from phase aberration occurs only in the isochronous volume, which is the spatial region from which an acoustic signal can be received if the beamformer is temporally gated to a point in time. Degradation from reverberation clutter, by contrast, occurs both within and outside the isochronous volume. Pulse lengthening can be observed primarily in the region trailing the isochronous volume and to a lesser extent within the isochronous volume.

In this paper we investigate and quantify the image quality improvement between fundamental and harmonic imaging due to these three sources of image quality degradation using a novel numerical algorithm that simulates ultrasonic propagation in a medium with heterogeneities in nonlinearity, attenuation, density, and speed of sound. The numerical simulations output the full pressure waveforms at every point in the simulated field and therefore allow great flexibility in calculating the ultrasound images and PSFs. Ultrasonic propagation through fine scale heterogeneities has been simulated with a finite difference time domain (FDTD) solution of the 3D linear wave

equation [71, 72]. This numerical implementation models the fine structure of human tissue and the arrangement of the tissue in the human body. The full-wave equation accounts for multiple reflections and scattering but current numerical implementations lack the ability to simulate nonlinear propagation and attenuation. Here we use a novel numerical solution to a nonlinear full-wave equation that additionally describes arbitrary frequency dependent attenuation and variations in density.

The numerical methods are used to simulate propagation from a diagnostic ultrasound transducer propagating through a histologically measured representation of the human abdomen [72]. In the simulations presented in this paper the heterogeneities are described with a resolution of $12.5 \mu\text{m}$. The broadband pulse is simulated as it is transmitted through the abdominal layer to a point scatterer and reflected back to the transducer surface. Conventional delay-and-sum beamforming is used to generate fundamental and harmonic PSFs for various scenarios. In addition to the abdominal PSFs a homogeneous control is presented for comparison as well as PSFs that represent only the imaging response due to reverberation clutter. In a subtraction calculation the reverberation clutter PSFs are used to obtain PSFs without reverberation. The medium is also altered to remove the effect of phase aberrations but retain identical clutter characteristics. These PSFs are compared to determine the relative importance of phase aberration, reverberation clutter, and pulse lengthening in fundamental and harmonic imaging.

Multiple transmit-receive simulations are used to compose a harmonic and fundamental ultrasound image using the same process that a diagnostic scanner employs. The pulses propagate, aberrate through the abdominal layer, reflect, scatter, and part of the transmitted energy returns to the transducer face where it is beamformed into an image. Unlike other simulations that use nonlinear propagation to create ultrasound images [69], this simulation, in addition to including the effects of

inhomogeneities and multiple scattering, does not require any linear convolution assumptions of the point spread function. The fully beamformed images are compared with convolution images to determine their validity in describing clutter within an anechoic lesion.

6.2 Methods and Results

The nonlinear full-wave equation describes acoustic fields in a nonlinear thermoviscous medium [52, 127]. It incorporates the effects of nonlinearity, attenuation, and all wave effects, such as multiple scattering, reflection, and refraction. It can be written as

$$\nabla^2 p - \frac{1}{c_0^2} \frac{\partial^2 p}{\partial t^2} + \frac{\delta}{c_0^4} \frac{\partial^3 p}{\partial t^3} + \frac{\beta}{\rho c_0^4} \frac{\partial^2 p^2}{\partial t^2} + \frac{1}{\rho} \nabla p \cdot \nabla \rho - \sum_{m=1}^v \xi_m = 0 \quad (6.1)$$

where ξ_m satisfies the equation

$$\dot{\xi}_m + \omega_m \xi_m = a_m \omega_m \frac{\Delta c}{c_0} \nabla^2 p \quad (6.2)$$

The first two terms in Eq. 6.1 represent the linear wave equation, the third term accounts for thermoviscous diffusivity, followed by nonlinearity, variations in density, and v relaxation mechanisms. Here p is the acoustic pressure, c_0 and ρ are the equilibrium speed of sound and density, δ is the acoustic diffusivity, and β is the nonlinearity parameter. The nonlinear parameter B/A is related to the coefficient, β , by $\beta = 1 + B/2A$ and the diffusivity δ can be expressed as a function of the absorption coefficient α with the equation $\delta = 2\alpha c_0^3/\omega^2$ (where ω is the angular frequency). The material parameters c_0 , δ , ρ and β can be functions of space. The relaxation equation (Eq. 6.2) has v peaks at characteristic frequencies ω_m with weight a_m that depend

on the particular frequency dependent attenuation law being modeled.

This equation is solved using finite differences in the time domain and solutions have been extensively verified with water tank measurements of a commercial diagnostic ultrasound transducer, comparisons with a Field II [60, 61], and solutions of Burgers' equation. Perfectly matched layers are used at the simulation boundaries to reduce reflections by approximately 80 dB [13, 21, 70]. Full details of the numerical methods and their verification can be found in Pinton et. al [87].

In this paper the simulations model propagation from a commercial diagnostic ultrasound. The array has an elevation focus of 2 cm, a lateral focus of 5 cm, F/1.5, and a center frequency of 2.1 MHz. A parabolically focused profile was used in both the lateral and elevation dimensions,

$$p(x, y, z = 0) = p_0 f(t + x^2/2c_0d_x + y^2/2c_0d_y) \quad (6.3)$$

where p_0 is the pressure amplitude, d_x is the lateral focus, d_y is the elevation focus and f is the impulse function:

$$f(t) = e^{-(\omega_0 t/n\pi)^{2m}} \sin(\omega_0 t) \quad (6.4)$$

Here the number of cycles, n , was set to 1.667 so that the fractional bandwidth was approximately 0.6, and the exponential drop-off parameter, m , was 2.

6.2.1 Backscatter

The ultrasonic pulse was transmitted through field of randomly distributed random amplitude scatterers with density of twelve scatterers per -6 dB resolution cell. The plot in Fig. 6.1 shows the simulated energy as a function of density from the

received backscattered signal. As expected the power has an f^4 energy dependence.

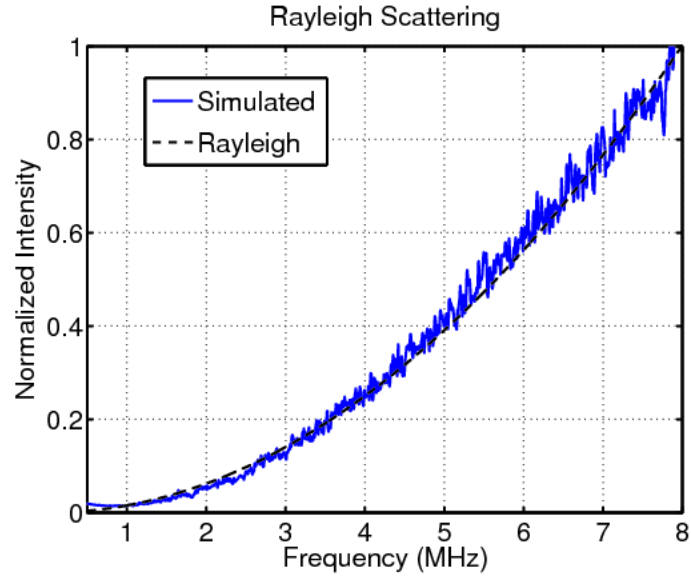


Figure 6.1: A comparison of the theoretical and simulated power spectrum of the backscatter from a field of randomly distributed scatterers in the Rayleigh regime.

The backscatter σ_s can be described by the equation [106]

$$\sigma_s = 4\pi a^2 \left(\frac{\omega}{\omega_0}\right)^4 \quad (6.5)$$

where a is the characteristic size of the scatterer, ω is the radial frequency of the impinging wave, and ω_0 is a material dependent characteristic frequency.

6.2.2 Heterogeneous propagation

A focused ultrasonic pulse was propagated through a two dimensional heterogeneous tissue model. The tissue representation was obtained from a histologically stained sample of human abdominal wall [56, 72] and the structures in the tissue were correlated with their measured properties of which the speed of sound is shown on

the right of Fig. 6.2. As shown in Table 6.1 in addition to variations in the speed of sound, there are variations in attenuation, density, and nonlinearity. The pressure field at the focus (5 cm) is shown on the right side of Fig. 6.2 on a compressed scale to illustrate small amplitude features such as those occurring from reflection, reverberation, and scattering.

Tissue	B/A	α (dB/MHz/cm)	c_0 (m/s)
Fat	9.6	0.40	1479
Muscle	8.0	0.15	1550
Connective	8.0	0.68	1613
Liver	7.6	0.50	1570

Table 6.1: Acoustic parameters for tissue

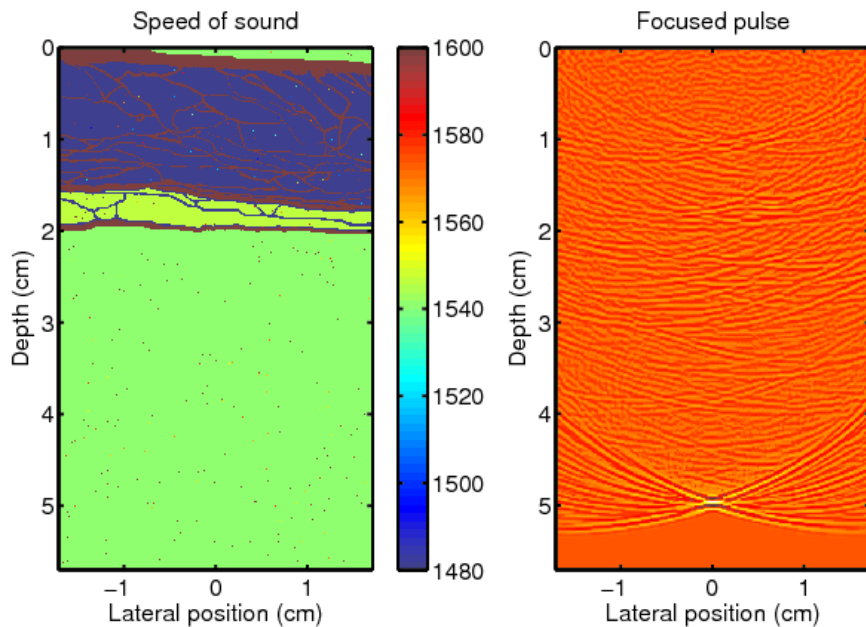


Figure 6.2: On the left, a graphical representation of the variation in the speed of sound for the abdominal layer (not shown are spatial variations in attenuation, nonlinearity, and density). On the right, the acoustic field of a diagnostic pulse at the focus (scale is compressed to emphasize small amplitudes)

6.2.3 Point spread functions

The transmit-receive PSFs were calculated for the same ultrasonic pulse but without the spatially distributed scatterers. A single $40\ \mu\text{m}$ point scatterer with a 25% impedance mismatch was placed at the 5 cm focus and conventional delay-and-sum beamforming was used to obtain the fundamental and harmonic point spread functions shown respectively on the left and right of Fig. 6.3. The material properties of the homogeneous medium have the same average speed of sound, attenuation, nonlinearity, and density as the abdominal layer properties.

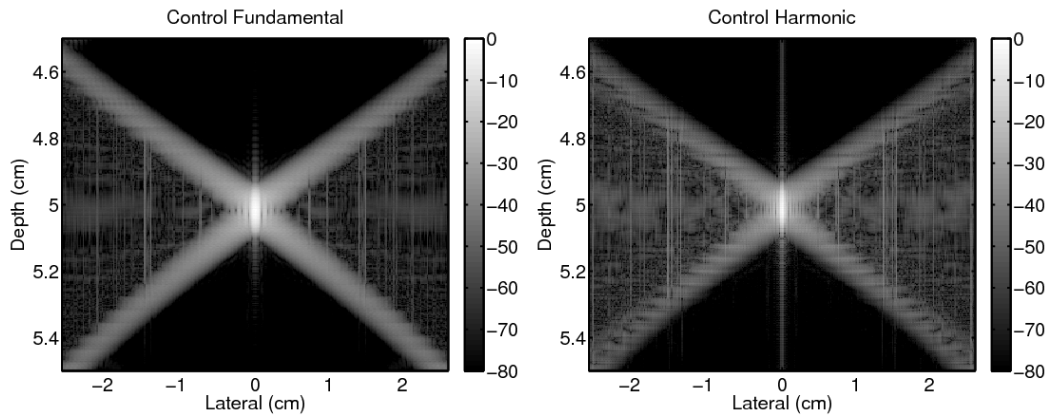


Figure 6.3: Transmit receive PSFs from an unapodized transducer in a homogeneous medium. The fundamental (left) and harmonic (right) PSFs are shown normalized relative to their peak. Note that the scales for the x and y axes are not geometrically proportional.

The plots of the PSFs have three distinct regions of interest: the “X” shaped portion spanning the image, representing a conventional PSF; the lateral regions within the isochronous volume to the left and right of the “X”; the region above, that precedes the pulse temporally; and the region below, that trails it. Note that the scales for the x and y axes are not geometrically proportional.

For the control PSFs the regions preceding and trailing the isochronous volume

do not contribute to the PSF. As expected there is a low level contribution within the isochronous volume. The mainlobe of the harmonic PSF is also visibly narrower than the fundamental. Note that the line centered at 0 cm laterally is a numerical artifact.

When the abdominal layer is added to the simulation the plots shown in Fig. 6.4 are obtained. These plots show the total transmit-receive PSFs for propagation through the abdominal wall model and include all the major effects that degrade the PSF, i.e. distributed aberration, reverberation, and multiple scattering.

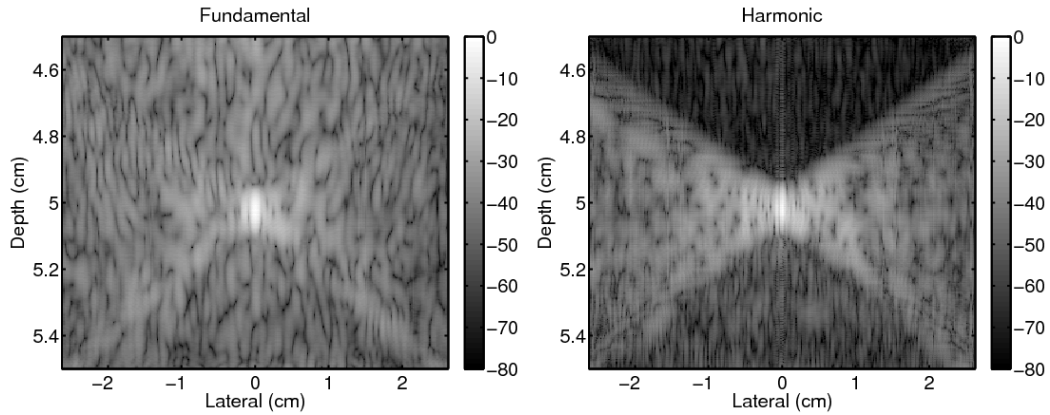


Figure 6.4: Point spread functions with clutter from propagation through a representation of the abdominal wall. The fundamental (left) and harmonic (right) PSFs are shown.

As can be observed in Tab. 6.2, compared to the homogeneous case the fundamental PSF suffers substantial amount of degradation in all three regions whereas the harmonic PSF is degraded primarily in the isochronous volume, to a lesser extent in the trailing region, and even less in the preceding region. In the preceding region the average dB intensity of the PSF increases by 57 dB for the fundamental and 34 dB for the harmonic. Compared to the control, the trailing region the fundamental increases by 40 dB and the harmonic region by 28 dB.

Since the sources of PSF degradation, aberration, reverberation, and multiple scattering, are not distinguishable from this plot alone the reverberation clutter from the abdominal layer was isolated. The point target from the focus was removed and the beamforming process was applied as before. The resulting PSFs, shown in Fig. 6.5, represent the contribution to the PSFs from reverberation clutter alone because only the reflections from the abdominal layer are used in the beamforming process.

	Isochronous		Preceding		Trailing	
	Fund.	Harm.	Fund.	Harm.	Fund.	Harm.
Homogeneous	-59.8	-58.6	-98.1	-93.8	-86.7	-83.9
Abdomen	-42.8	-46.9	-41.1	-68.2	-46.8	-56.0
Reverb. Subtracted	-48.6	-47.8	-92.6	-84.6	-55.2	-56.1
Isovelocity	-46.6	-57.7	-42.5	-71.2	-49.9	-63.0

Table 6.2: Mean dB values for three regions of PSFs

It is immediately apparent from these plots that the fundamental image is more susceptible to near-field reverberation clutter than the harmonic image. The average for the fundamental reverberation PSF is -46 dB and the average for the harmonic is PSF is -72 dB or a 26 dB difference, which is consistent with the previously discussed increases in the trailing and preceding regions.

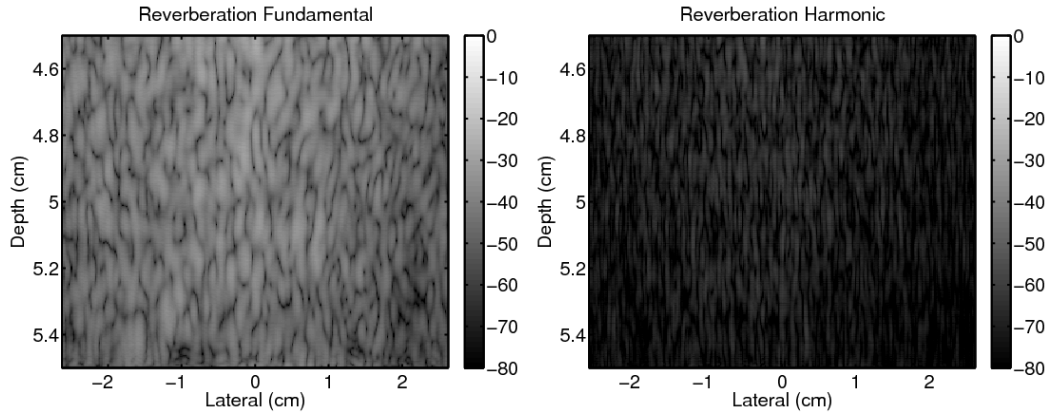


Figure 6.5: Point spread functions of the reverberation clutter from propagation through a representation of the abdominal wall. The fundamental (left) and harmonic (right) PSFs are shown without any signal from a point target.

The reverberation clutter in Fig. 6.5 can be linearly subtracted from the original PSFs shown in Fig. 6.4 to obtain PSFs without the effects of near field clutter, shown in Fig. 6.6. This figure still includes the effects of aberration and pulse lengthening. There is a marked improvement in the fundamental PSF because the clutter in the preceding region is removed, there is a substantial reduction in the trailing region, and there is a small improvement in the isochronous volume. As shown in Tab. 6.2, the differences between these regions when compared to the original abdominal PSFs are respectively 52 dB, 32 dB, and 6 dB.

In the harmonic PSF the clutter in the preceding region is also removed but, because the original harmonic PSF does not have much clutter there to begin with, the improvement is comparatively small. In the preceding, trailing, and isochronous volumes the reduction in clutter is 16 dB, 0.1 dB, and 1 dB, which is substantially less than for the equivalent fundamental PSF values.

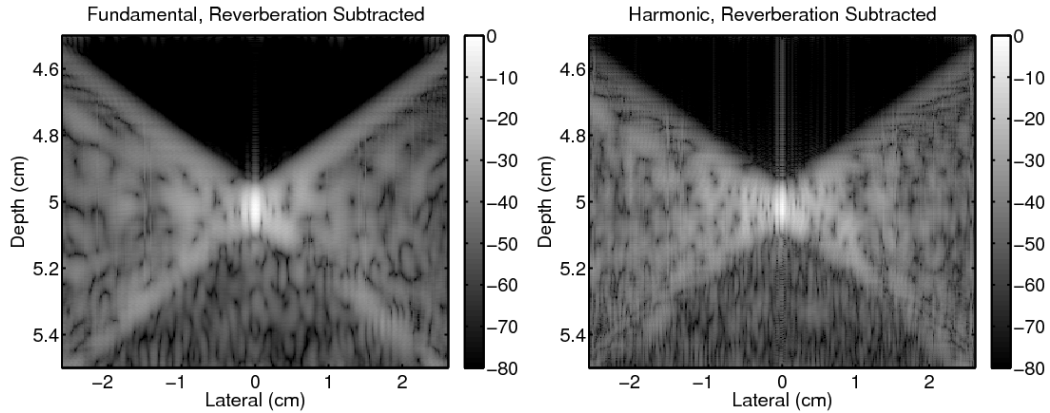


Figure 6.6: Point spread functions without reverberation clutter obtained by subtracted the reverberation clutter PSF (Fig. 6.5) from the abdominal PSF (Fig. 6.4).

To remove the effects of aberration the speed of sound was set to a uniform value corresponding to the mean (1537 m/s) and the tissue densities were altered to maintain the original impedance mismatch. This modification preserves the phase profile of the ultrasonic pulse while generating an equal amount of reverberation and multiple reflections. All other tissue parameters and pulse properties were unchanged.

The resulting PSFs are shown in Fig. 6.7. When compared to the original PSFs in Fig. 6.4 the fundamental appears quite similar. However, the harmonic PSF with the modified medium has significantly less clutter within the isochronous volume. In this figure the isochronous volume of the harmonic looks similar to that shown for the control PSF in Fig. 6.3. When compared to the abdominal PSF the fundamental PSF exhibits an improvement of 4 dB, 1 dB, and 3 dB in the isochronous, preceding, and trailing regions. The harmonic PSF, on the other hand, improves by 11 dB, 3 dB, and 7 dB.

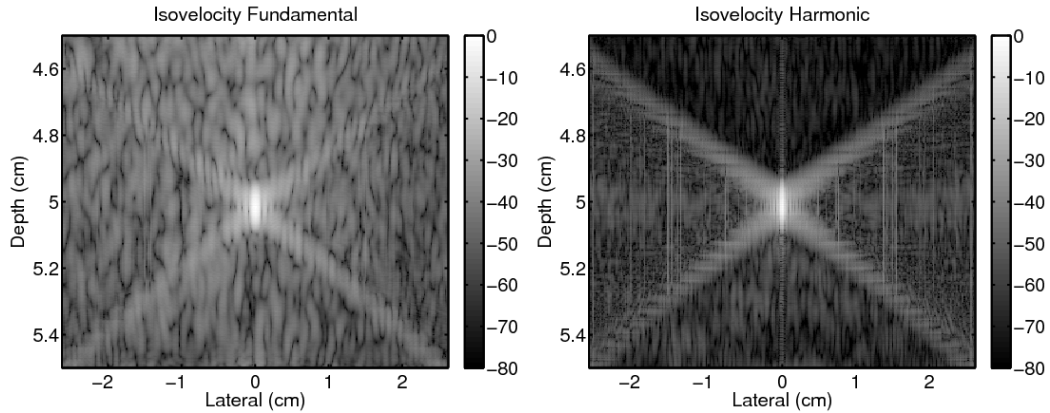


Figure 6.7: Point spread functions without aberration obtained propagating the ultrasonic pulse through a medium with no variations in the speed of sound but with an unchanged impedance compared to the abdominal layer.

6.2.4 Ultrasonic Imaging

To simulate a scattering ultrasonic medium, twelve point scatterers per resolution cell were overlaid on the tissue representation. The point scatterers have a $40\ \mu\text{m}$ diameter and a random spatial and amplitude variation with a mean variation in the speed of sound of $77\ \text{m/s}$, which corresponds to a 5% variation of the accepted average tissue velocity of $1540\ \text{m/s}$. A circular anechoic region with a $5\ \text{mm}$ diameter was placed at the focus to mimic a lesion. To simulate an ultrasonic imaging system, a focused pulse was transmitted and allowed to propagate. The resulting reflections were measured and a standard dynamic receive delay-and-sum beamforming algorithm was used to create a single A-line. The process was repeated by translating the transducer and forming a series of A-lines that are shown as fundamental (left) and harmonic (right) B-mode images in Fig. 6.8. A 100% bandwidth bandpass filter was used to obtain the fundamental and harmonic components from the raw data. No point spread function assumptions were used to form the images.

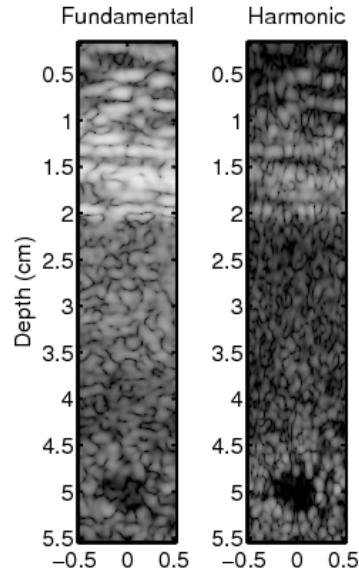


Figure 6.8: Simulated fundamental and harmonic ultrasound images of a 5 mm anechoic lesion at 5 cm below an abdominal layer using transmit-receive beamforming.

To compare the beamformed images with those predicted by linear convolution theory, the fundamental PSF was convolved with a scatterer field of randomly distributed amplitude and spatial location. All regions except the lesion were populated by scatterers. A finite choice for the convolution kernel size must be used in computations. Each ultrasonic image shown in Fig. 6.9 convolves the scatterer field with increasing kernel sizes for the PSF, ranging from 3.7×1.8 mm to 14.8×7.2 mm. As the kernel size increases the amount of clutter observed in the lesion also increases but even with the largest PSF kernel size the clutter level does not approach that observed in the beamformed image. As shown in Tab. 6.3 for the contrast to noise ratio (CNR) varies from 2.20 to 2.00 from the smallest to largest kernel size whereas in the fundamental beamformed image shown in Fig. 6.8 the CNR is 1.48.

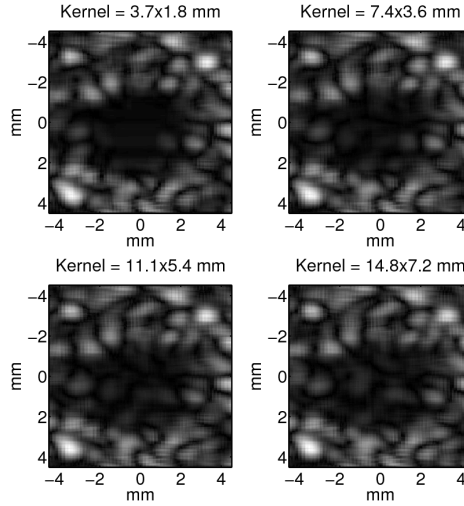


Figure 6.9: Ultrasonic images of a 5 mm circular anechoic lesion obtained with linear convolution theory for varying fundamental PSF sizes.

Kernel Size (mm)	CNR
3.7×1.8	2.20
7.4×3.6	2.04
11.1×5.4	2.01
14.8×7.2	2.00
Beamformed	1.48

Table 6.3: CNR for varying PSF kernel size

Figure 6.10 illustrates the contribution to the PSF of low level clutter distributed over a large area by plotting the radial integral of the fundamental and harmonic PSFs for their three regions. The most striking difference between the energy distributions in the PSFs occurs in the preceding region where there is an increase with radius for the fundamental but a decrease for the harmonic. The amount of signal coming from the isochronous volume is large in both the fundamental and harmonic PSFs but it is comparatively more significant in the harmonic where there is approximately a 12 dB difference between it and the nearest curve. In the fundamental PSF none of the curves appear to appreciably decrease with radial distance but in the harmonic PSF

they all do.

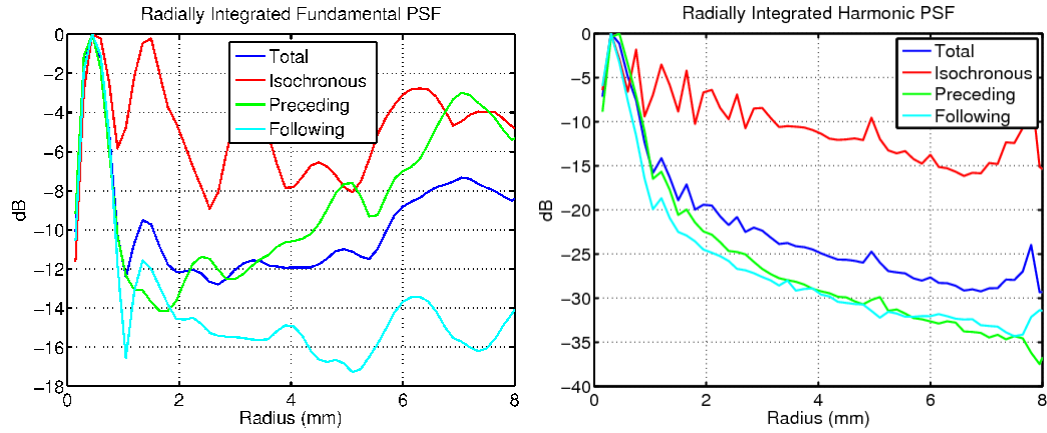


Figure 6.10: Radial integration of the fundamental and harmonic abdominal PSFs. Note: not normalized by radius and plotted on different scales.

6.3 Discussion

6.3.1 Point source brightness

The PSFs were obtained by beamforming the return echo from a point scatterer at the focus that has an arbitrarily assigned brightness. With a brighter target the parts of the PSF that are reflected from the focal point would have higher levels in the previously shown PSF plots. In particular the isochronous volume and the trailing region would appear to be more significant than the reverberation clutter. We can therefore make absolute comparisons between fundamental and harmonic PSFs or between the isochronous volume and the trailing region with confidence but we avoid comparisons with the reverberation clutter.

6.3.2 Sources of PSF degradation

As mentioned previously, there are three distinct sources of PSF degradation explored in this paper, two of which affect the ultrasonic pulse, and one which degrades the signal received by the transducer. First, as a pulse propagates through tissue its phase aberrates from a focused profile. Second it is lengthened in the direction of propagation by multiple reflections. Phase aberration occurs only within the isochronous volume and the effects of pulse lengthening can be observed in the isochronous volume and the trailing region of the PSF. Third, multiple reflections and reverberation of sound within the layers and structure in tissue also create a background of acoustic clutter that uniformly degrades the PSF in all three regions.

It is clear from the beamformed images in Fig. 6.8 that the lesion in the harmonic image has better boundary definition and more contrast, however the different sources of image degradation are integrated over the PSF and cannot be determined just from the image. The plots of the PSFs at the focus, in Fig. 6.4, show that the harmonic PSF is less sensitive away from the peak, especially in the preceding and following regions where the improvement is 27 dB and 10 dB, respectively.

6.3.3 Reverberation clutter

The plots in Fig. 6.5 show that the amount of clutter due to reverberation is 26 dB higher for the fundamental PSF than for the harmonic, indicating that there is significantly more energy reflected from near-field structures at the fundamental frequency. For short propagation distances the energy in the pulse is primarily at the fundamental frequency. As the pulse travels through the tissue there is an accumulation of harmonic energy from both the propagation distance and the increase in pressure from focusing. By the time a significant amount of harmonic signal has

developed the pulse has already propagated through the near-field abdominal layer. It is thus less susceptible to reverberation clutter from near-field structures because there is little energy at that frequency.

We have thus quantified with a validated model that reverberation clutter is a source of image degradation in fundamental imaging. To determine if it is the primary source of degradation, the reverberation clutter was subtracted from the original abdominal PSFs to obtain the PSFs shown in Fig. 6.6. In contrast to the original abdominal PSFs, the fundamental and harmonic reverberation corrected PSFs have very similar characteristics in the three regions of interest. According to Tab. 6.2 the average dB levels in the isochronous volume are within 0.8 dB of each other, for the trailing region they are within 0.9 dB, and in the preceding region both are below -80 dB. This indicates that, with the reverberation clutter subtracted, the fundamental and harmonic PSFs have very similar clutter characteristics. Inversely this demonstrates that the primary source of degradation in fundamental imaging compared to harmonic imaging is reverberation clutter.

6.3.4 Phase aberration

The comparative importance of phase aberration was determined by simulating pulse propagation through an equivalent tissue model with uniform speed of sound but unchanged impedance characteristics. These PSFs are shown in Fig. 6.7. The isochronous region of the harmonic PSF appears to be very similar to the equivalent isochronous region shown in Fig. 6.3 for the homogeneous PSF. In fact the average dB level between the two is within 0.9 dB indicating that phase aberration is the primary source of degradation within the isochronous volume for the harmonic PSF. An equivalent statement cannot be made for the fundamental PSF because there

is still a substantial amount of energy from the reverberation clutter observable in the isochronous volume. Compared to the original abdominal PSFs removing phase aberration improves the fundamental isochronous volume by 4 dB and the harmonic isochronous volume by 11 dB. The harmonic PSF is therefore more susceptible to phase aberration than the fundamental, which is consistent with the understanding that higher frequencies incur comparatively larger aberration. Furthermore aberration degrades it to a larger extent than reverberation clutter.

6.3.5 Validity of convolution

A visual comparison of the lesion in the fundamental beamformed image in Fig. 6.8 to any of the convolution images in Fig. 6.9 indicates that the convolution images underestimate the amount of clutter in the lesion. As shown in Tab. 6.3 the size of the convolution kernel increases the CNR decreases but it quickly approaches a region of diminishing returns and the difference in CNR between the last two kernel sizes is 0.5% yet these figures are overestimating the CNR by at least 34%. Figure 6.10 shows that the contribution to the fundamental PSF does not appreciably decrease with increasing radial distance. Clutter in the PSFs comes from low amplitude regions that are distributed over a large area. To accurately represent the clutter in convolutions with scatterers a very large area must be preserved, obviating many of the benefits of convolution theory.

6.4 Summary and Conclusions

A numerical method that solves the nonlinear attenuating wave equation in heterogeneous media was used to determine the primary sources of clutter in fundamental and harmonic imaging. The simulation of a 2.1 MHz diagnostic transducer through

a measured representation of the human abdominal layer generated the transmit-receive PSFs. For this particular imaging system there are three distinct conclusions that can be drawn from the presented data.

First the primary source of image degradation in the fundamental PSF comes from reverberation in the near-field abdominal structures. Measurements of the reverberation clutter alone indicate that it is 26 dB higher for the fundamental PSF compared to the harmonic PSF and that it is the single largest source of clutter. Second phase aberration is the largest source of clutter in the harmonic PSF. When phase aberration is removed using a uniform velocity and unchanged impedance medium the harmonic PSF exhibits an 11 dB improvement in the isochronous volume, which is significantly larger than the 0.9 dB improvement from reverberation clutter subtraction. Finally clutter in the PSFs occurs primarily from low level contributions distributed over a large area, especially in the fundamental PSF where plots of the radial distribution show no appreciable decrease with increasing distance.

6.5 Acknowledgments

We would like to thank Joshua Baker-LePain for technical support with the computer cluster and T. Douglas Mast for providing the histological data for the human abdominal wall. This work was supported by NIH grants R01-HL075485 and R01-CA114093.

Chapter 7

Numerical nonlinear ultrasonic imaging in heterogeneous media

The work presented in this chapter is in preparation for IEEE Transaction on Ultrasonics, Ferroelectronics, and Frequency Control [91].

7.1 Introduction

Harmonic imaging has been shown to have significantly improved image quality when compared to fundamental imaging and has gained widespread clinical use [59, 110, 116]. The most dramatic differences are visible in abdominal[23], pelvic[37], and cardiac sonography [66] where improvements in lateral and axial resolution, contrast to noise ratio, clutter rejection, increased penetration, lesion visibility and diagnostic confidence are reported.

Although harmonic imaging is used extensively, the mechanisms by which harmonic imaging works in tissue and optimization of an ultrasound system's parameters for harmonic imaging are still a poorly understood processes. For a homogeneous medium, the image quality improvements are due to a reduction in the harmonic main lobe width and height of the side lobes [27, 28]. However, some of the most important aspects of harmonic imaging are its reported abilities to reduce clutter and aberration which are heterogeneous phenomena [2, 38]. The complexity of performing experiments or simulations in a three dimensional medium has been an obstacle in describing and quantifying the precise mechanisms of image quality improvement in harmonic imaging.

To more accurately quantify the metrics of image quality improvement we define sources of point spread function (PSF) degradation that are directly related to physical phenomena [92]. Layered interfaces with large impedance mismatches, such as fat and muscle [126], provide an ideal acoustic environment to trap energy from a propagating ultrasonic pulse. Part of the reverberating energy leaks back to the transducer where it adds noise to more distal structures, which is referred to as reverberation clutter.

A second metric of image quality degradation is due to reflections that are leaked in the direction of pulse propagation adding a long, low amplitude tail to the originally compact pulse. This pulse lengthening reduces the axial resolution and also adds clutter to the image, though in a less uniform fashion than reverberation clutter.

The final metric considered in this paper is aberration in the pulse profile from variations in acoustic velocity or attenuation. When the acoustic velocity of tissue is inhomogeneous across the pulse wavefront parts of it travel faster or slower introducing aberrations in the ideally focused phase profile. Variations in attenuation cause aberrations in amplitude. Theoretical and *in vivo* studies have shown that both types of aberration increase the width of the mainlobe and raise the level of the sidelobes, which reduces the resolution and contrast [39, 54, 81, 114, 118, 135].

The degradation of the PSF from these three sources occurs in specific regions. Aberration shifts the peak of the PSF to the outlying of the isochronous volume, which is the spatial region from which an acoustic signal can be received if the beamformer is temporally gated to the a point in time. Degradation from reverberation clutter occurs throughout the PSF, both within and outside the isochronous volume. Pulse lengthening can be observed primarily in the region trailing the isochronous volume and to a lesser extent within the isochronous volume [92].

In an experiment with a porcine abdominal tissues, one dimensional measure-

ments showed that the harmonic field was less aberrated than the fundamental [123]. However a three dimensional study that simulated a series of phase screens to mimic distributed aberration reached the conclusion that aberration affects that harmonic to the same degree as the fundamental [120, 121]. These simulations used a one-way wave equation and thus cannot model multiple reflections and scattering. A full-wave equation that includes multiple reflections and describes nonlinear propagation in a heterogeneous medium was used to simulate ultrasonic imaging through a measured representation of the human abdomen [87]. This research compared the relative importance reverberation clutter, pulse lengthening, and aberration. It was shown that aberration has a greater effect on the harmonic than the fundamental. The primary mechanism of harmonic image improvement was the reduction of reverberation clutter.

In this paper we investigate and quantify the three aforementioned metrics of image quality improvement between fundamental and harmonic imaging due to changes in the transducer $F/\#$, the transmit frequency, and the source pressure. A novel numerical algorithm is used that simulates ultrasonic propagation in a medium with heterogeneities in nonlinearity, attenuation, density, and speed of sound. The numerical simulations generate the full pressure waveforms at every point in the simulated field and therefore allow great flexibility in calculating the ultrasound images and PSFs. Ultrasonic propagation through fine scale heterogeneities has previously been simulated with a finite difference time domain (FDTD) solution of the 3D linear wave equation [71, 72]. This numerical implementation accounts for multiple reflections and scattering but current numerical implementations lack the ability to simulate nonlinear propagation and attenuation. The numerical methods used in this paper additionally describes arbitrary frequency dependent attenuation and variations in density.

The numerical methods are used to simulate propagation from a diagnostic ultrasound transducer propagating through a histologically measured representation of the human abdomen [72]. In the simulations presented in this paper the heterogeneities are described with a resolution of $12.5 \mu\text{m}$. The broadband pulse is simulated as it is transmitted through the abdominal layer to a point scatterer and reflected back to the transducer surface. Conventional delay-and-sum beamforming is used to generate fundamental and harmonic PSFs for various scenarios.

Multiple transmit-receive simulations are used to compose harmonic and fundamental ultrasound images using beamforming processes that diagnostic scanners employ. The pulses propagate, aberrate through the abdominal layer, reflect, scatter, and part of the transmitted energy returns to the transducer face where it is beamformed into an image line. Unlike other simulations that use nonlinear propagation to create ultrasound images [69], this simulation, in addition to including the effects of inhomogeneities and multiple scattering, does not require any linear convolution assumptions of the point spread function. It has been previously demonstrated that convolution images may not accurately describe clutter because the PSFs must have a large spatial extent to describe the large area and low amplitude region that contributes to image degradation [92].

7.2 Methods

The nonlinear full-wave equation describes acoustic fields in a nonlinear thermo-viscous medium [52, 127]. It incorporates the effects of nonlinearity, attenuation, and most wave effects, such as multiple scattering, reflection, and refraction and is written as

$$\nabla^2 p - \frac{1}{c_0^2} \frac{\partial^2 p}{\partial t^2} + \frac{\delta}{c_0^4} \frac{\partial^3 p}{\partial t^3} + \frac{\beta}{\rho c_0^4} \frac{\partial^2 p^2}{\partial t^2} + \frac{1}{\rho} \nabla p \cdot \nabla \rho - \sum_{m=1}^v \xi_m = 0 \quad (7.1)$$

where ξ_m satisfies the equation

$$\dot{\xi}_m + \omega_m \xi_m = a_m \omega_m \frac{\Delta c}{c_0} \nabla^2 p \quad (7.2)$$

The first two terms in Eq. 7.1 represent the linear wave equation, the third term accounts for thermoviscous diffusivity, followed by nonlinearity, variations in density, and v relaxation mechanisms. Here p is the acoustic pressure, c_0 and ρ are the equilibrium speed of sound and density, δ is the acoustic diffusivity, and β is the nonlinearity parameter. The nonlinear parameter B/A is related to the coefficient, β , by $\beta = 1 + B/2A$ and the diffusivity δ can be expressed as a function of the absorption coefficient α with the equation $\delta = 2\alpha c_0^3/\omega^2$ (where ω is the angular frequency). The material parameters c_0, δ, ρ and β can be functions of space. The relaxation equation (Eq. 7.2) has v peaks at characteristic frequencies ω_m with weight a_m that depend on the particular frequency dependent attenuation law being modeled.

This equation is solved using finite differences in the time domain and solutions have been extensively verified with water tank measurements of a commercial diagnostic ultrasound transducer, comparisons with a Field II [60, 61], and solutions of Burgers' equation. Perfectly matched layers are used at the simulation boundaries to reduce reflections by approximately 80 dB [13, 21, 70]. Full details of the numerical methods and their verification can be found in Pinton et. al [87].

A focused ultrasonic pulse was propagated through a two dimensional heterogeneous tissue model with twelve point scatterers per resolution. The initial pulse had an amplitude of 0.5 MPa and was spherically focused at 5 cm from an unapodized transducer. Its center frequency was 2.1 MHz with a 67% bandwidth. Transmit-receive point spread functions were calculated for the same ultrasonic pulse propagating through the tissue layer but without the spatially distributed scatterers. A

single point scatterer was placed at the focus and beamforming was used to obtain the fundamental and harmonic point spread functions.

Four transducer configurations were simulated. The first case was an F/1 aperture with a 1 MPa source pressure. Then the source pressure was reduced to 0.2 MPa. The aperture for the third transducer was reduced to F/3 and the pressure was increased to 3 MPa to compensate for the reduction in the aperture. Finally a 1 MPa, F/1 transducer with transmit frequency that was doubled to 4.2 MHz was simulated.

The tissue representation was obtained from a histologically stained sample of human abdominal wall [56, 72] and the structures in the tissue were correlated with their measured properties of which the speed of sound is shown on the right of Fig. 7.1. Table 7.1 shows the values for speed of sound, attenuation, and nonlinearity used in these simulations. The point scatterers have a 40 μm diameter and a random spatial and amplitude variation with a mean variation in the speed of sound of 77 m/s, which corresponds to a 5% variation of the accepted average tissue velocity of 1540 m/s. The pressure field at the focus (5 cm) is shown on the right side of Fig. 7.1 on a compressed scale to emphasize small amplitude features such as those occurring from reflection, reverberation, and scattering.

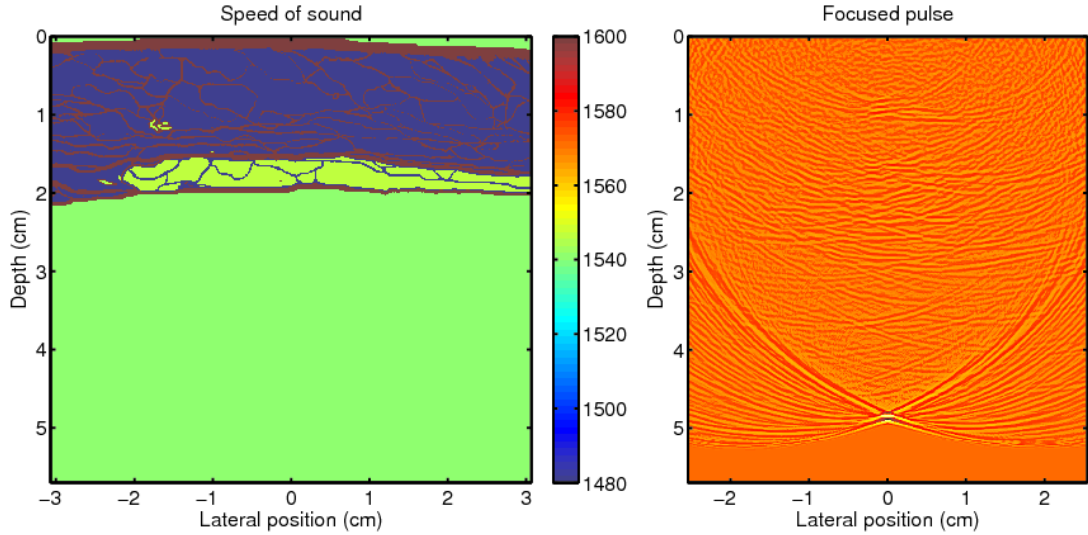


Figure 7.1: On the left, a graphical representation of the variation in the speed of sound for the abdominal layer (not shown are spatial variations in attenuation, nonlinearity, and density). On the right, the acoustic field of a diagnostic pulse at the focus (scale is compressed to emphasize small amplitudes).

Tissue	B/A	α (dB/MHz/cm)	c_0 (m/s)
Fat	9.6	0.40	1479
Muscle	8.0	0.15	1550
Connective	8.0	0.68	1613
Liver	7.6	0.50	1570

Table 7.1: Typical acoustic parameters for tissue

7.3 Results

The image on the left of Fig. 7.2 is the speed of sound map for the section of the abdominal wall shown in the ultrasound images. The simulated fundamental image is shown in the middle of the figure, and the harmonic on the right on a 60 dB dynamic range. The anechoic lesion is visible at 5 cm in both images but its contrast is superior and its boundaries are better defined in the harmonic image.

According to Tab. 7.2, where the contrast to noise ratios (CNR) for the ultrasound images are summarized, the harmonic image has a CNR that is almost 50% better than the fundamental image. Overall the fundamental image is brighter. Relative to the speckle brightness the near-field abdominal structures are also brighter in the fundamental image.

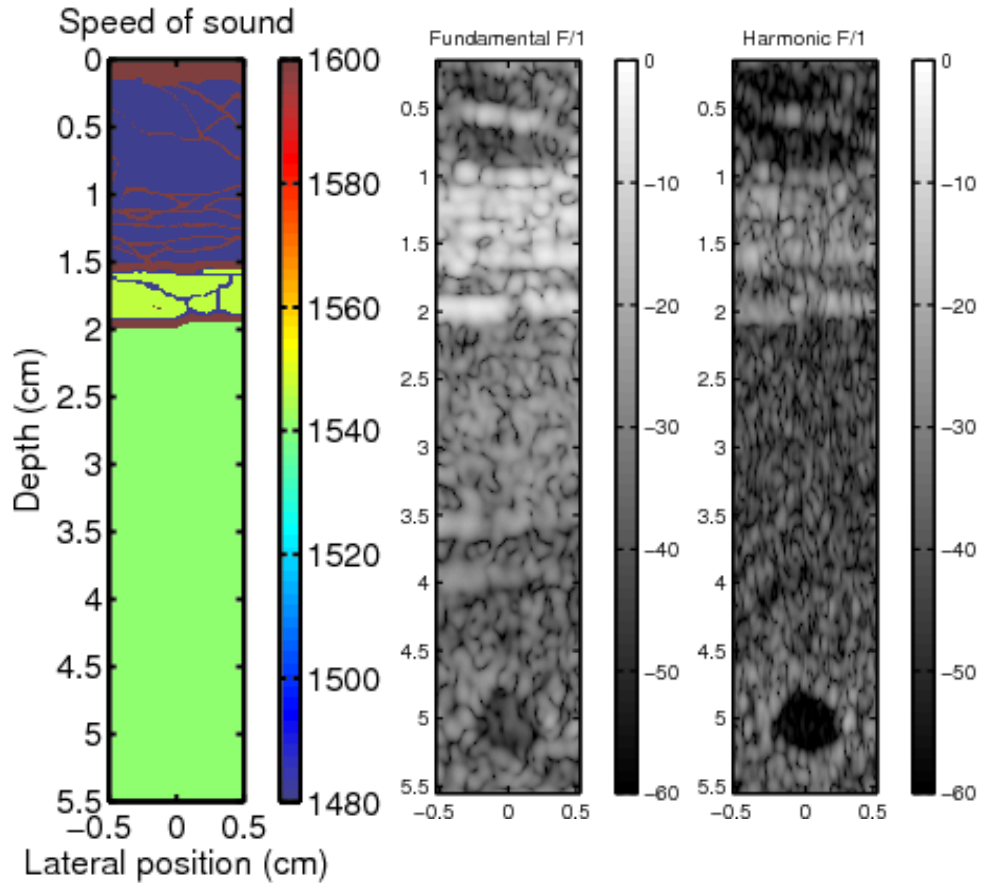


Figure 7.2: On the left, the speed of sound map for the section of the abdominal wall shown in the ultrasound images. Simulated fundamental (middle) and harmonic (right) ultrasound images of an anechoic region, visible below the abdomen at 5 cm. The source pressure is 1 MPa and the aperture is F/1.

When the pressure of the transmitted pulse is reduced by a factor of five the resulting images, shown in Fig. 7.3 do not appear any different. The boundary

	Fundamental CNR	Harmonic CNR
F/1	0.9961	1.4748
P/5	0.9979	1.4710
F/3	0.4885	1.2536
2f	1.1238	0.9731

Table 7.2: Contrast to noise ratios for images of the anechoic lesion.

definition, contrast speckle brightness and even speckle pattern appears to have the same structure for both the fundamental and harmonic images.

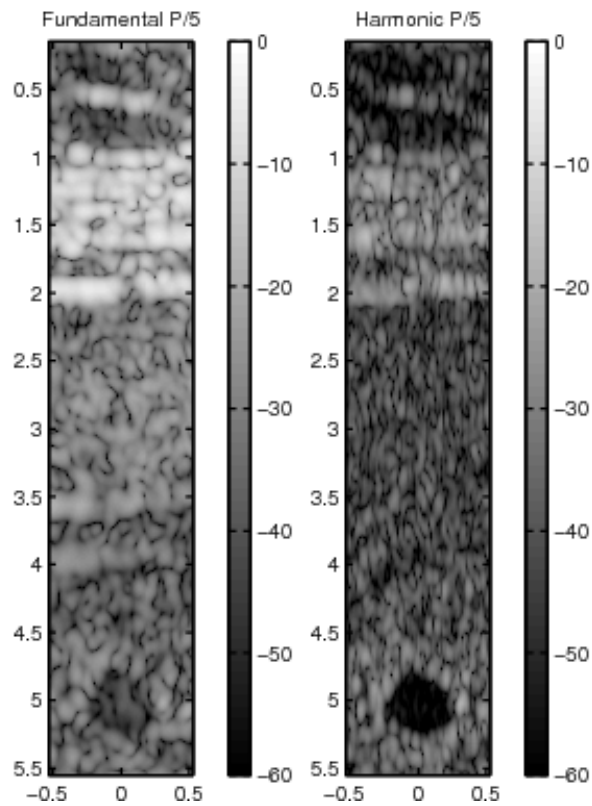


Figure 7.3: Simulated fundamental (left) and harmonic (right) ultrasound images of an anechoic region, visible below the abdomen at 5 cm. The source pressure is 0.2 MPa and the aperture is F/1.

A reduction of the aperture to F/3, shown in Fig. 7.4, results in larger speckle size, a reduction in speckle brightness relative to the near-field structures, and poorer

boundary definition for the fundamental and the harmonic images. The CNR for the fundamental image is 0.49 which is significantly worse than the 1.00 CNR for the F/1 image. The CNR for the harmonic image is 1.25, slightly worse than 1.48 for the F/1 case, but it represents over 125% improvement over the fundamental image, which is a larger improvement than that observed for the F/1 image.

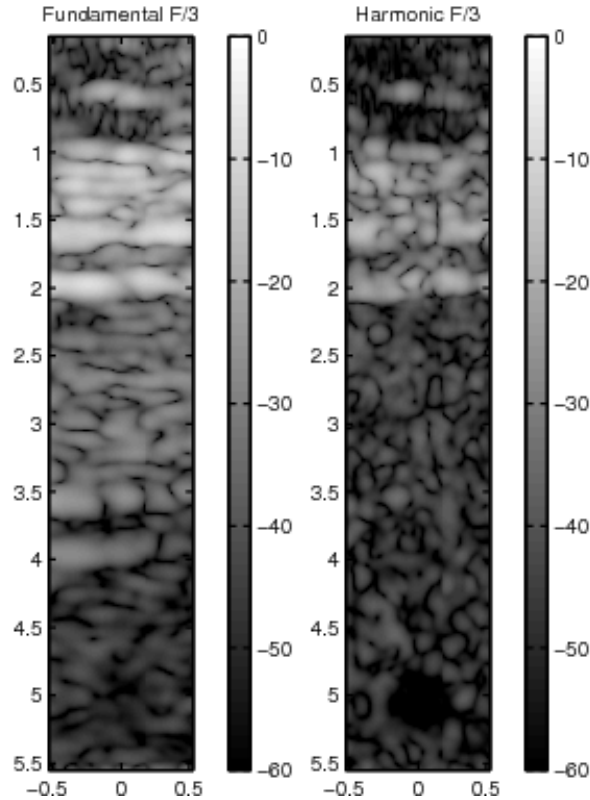


Figure 7.4: Simulated fundamental (left) and harmonic (right) ultrasound images of an anechoic region, visible below the abdomen at 5 cm. The source pressure is 0.2 MPa and the aperture is F/1.

The fundamental and harmonic images for twice the transmit frequency in Fig. 7.5 exhibit subtle differences in the boundary definition and contrast of the lesion. Of all the fundamental images the 4.2 MHz fundamental image produces the greatest CNR of the cyst, while for all harmonic images, the 4.2 MHz transducer yields the

worst CNR. The ratio of scatterer brightness to the near-field structures appears to be largest of all images considered. Note that the dynamic range shown in these images was increased to 80 dB.

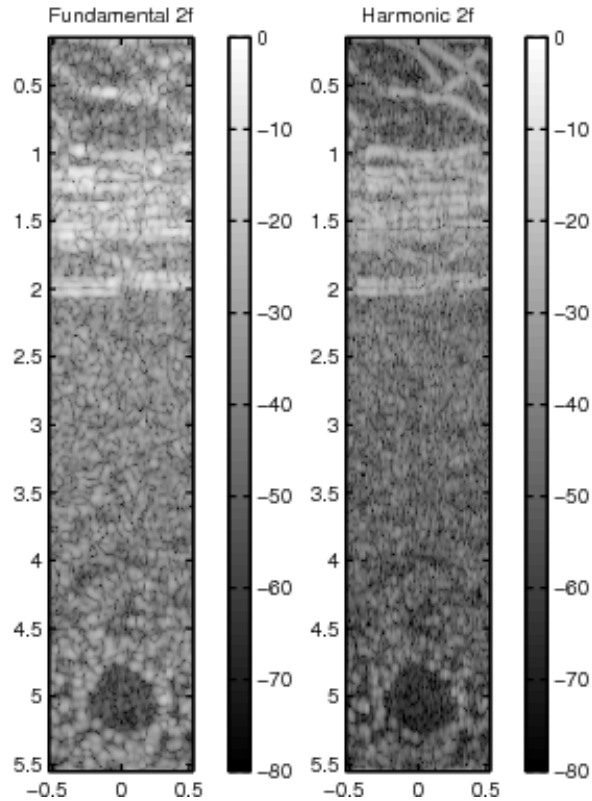


Figure 7.5: Simulated fundamental (left) and harmonic (right) ultrasound images of an anechoic region, visible below the abdomen at 5 cm. The source pressure is 1 MPa, the aperture is $F/1$, and the transmit frequency has been doubled to 4.2 MHz. Note the increase in dynamic range to 80 dB.

Figures 7.6-7.9 display the PSFs shown in Figs. 7.2-7.5. They can be described as having three distinct regions of interest: the “X” shaped portion spanning the image, representing a conventional PSF; the lateral regions within the isochronous volume to the left and right of the “X”; the region above, that precedes the pulse temporally; and the region below, that trails it. Note that the scales for the x and y axes are not geometrically proportional.

Figure 7.6 shows the fundamental (left) and harmonic (right) PSFs for the 1 MPa transmit pressure and F/1 aperture, which corresponds to the images shown in Fig. 7.2. The harmonic PSF has significantly lower clutter levels, especially in the preceding region where, according to Tab. 7.3, the average dB levels for the harmonic are 22.2 dB lower, and to a lesser extent in the trailing region where the difference is 7.6 dB.

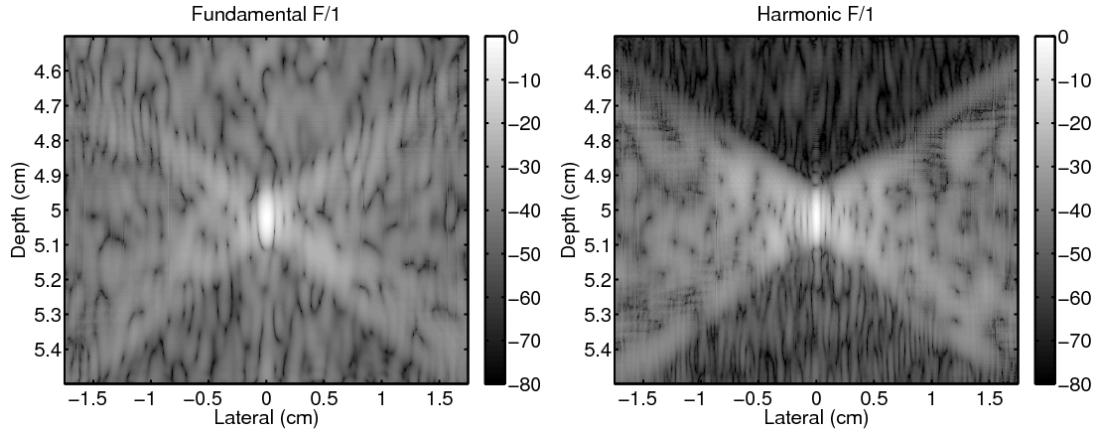


Figure 7.6: Fundamental (left) and harmonic (right) point spread functions from propagation through a representation of the abdominal wall. The source pressure is 1 MPa and the aperture is F/1. Note that the axes are not geometrically proportional.

	Isochronous		Preceding		Trailing	
	Fund.	Harm.	Fund.	Harm.	Fund.	Harm.
F/1	-39.8	-41.6	-42.7	-64.9	-47.0	-54.6
P/5	-40.2	-41.3	-44.5	-63.0	-48.3	-54.2
F/3	-32.1	-36.8	-29.8	-50.9	-34.0	-49.9
2f	-44.4	-40.8	-57.0	-58.7	-56.2	-52.0

Table 7.3: Mean dB values for three regions of PSFs

Just like Figs. 7.2 and 7.3 the PSFs for the reduced pressure, shown in Fig. 7.7, are practically indistinguishable from the PSFs shown in Fig. 7.6. Even minor details of the clutter speckle exhibit a close correspondence.

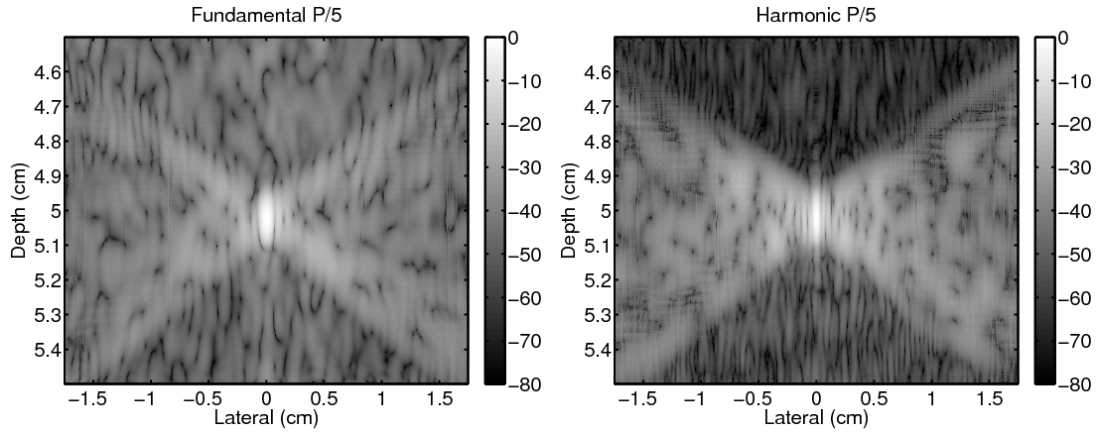


Figure 7.7: Fundamental and harmonic point spread functions from propagation through a representation of the abdominal wall. The source pressure is reduced to 0.2 MPa and the aperture is F/1.

In the plots of the PSFs for the reduced aperture, shown in Fig. 7.8 there is a characteristic narrowing of the isochronous volume and visible widening of the mainlobe, consistent with the enlarged speckle size shown in Fig. 7.4. The isochronous volume of the fundamental image is hardly visible through the clutter. The harmonic image shows a considerable improvement in almost equal measure in the trailing and preceding regions where the average dB levels are within 1 dB of each other. Compared to the F/1 harmonic PSF, in Fig. 7.6, the average dB levels in the preceding region are 14 dB higher and in the trailing region they are 4.7 dB higher indicating that the relative improvement is larger in the trailing region.

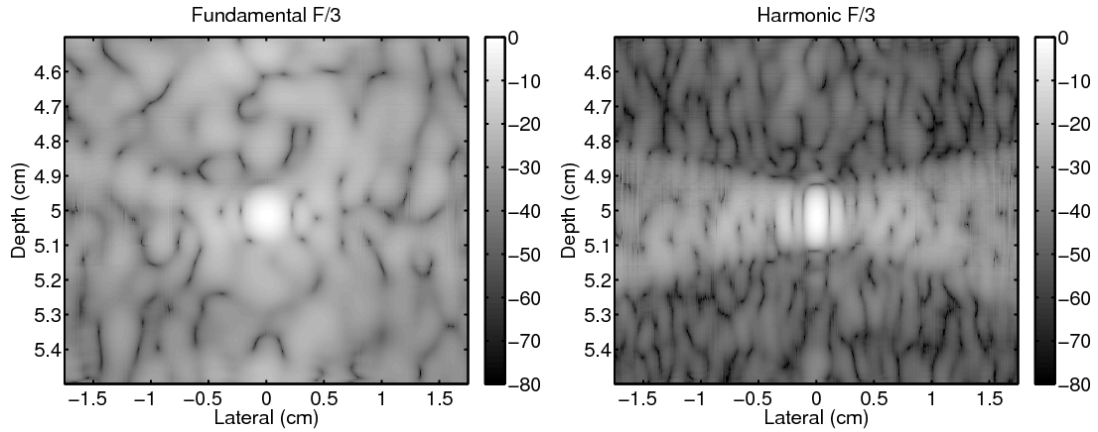


Figure 7.8: Fundamental and harmonic point spread functions from propagation through a representation of the abdominal wall. The source pressure is 3 MPa and the aperture is reduced to $F/3$.

The PSFs for the doubled frequency, in Fig. 7.9 have similar dB levels in all three regions of the PSF. According to Tab. 7.3 the harmonic PSF is approximately 4 dB worse primarily in the isochronous and trailing region.

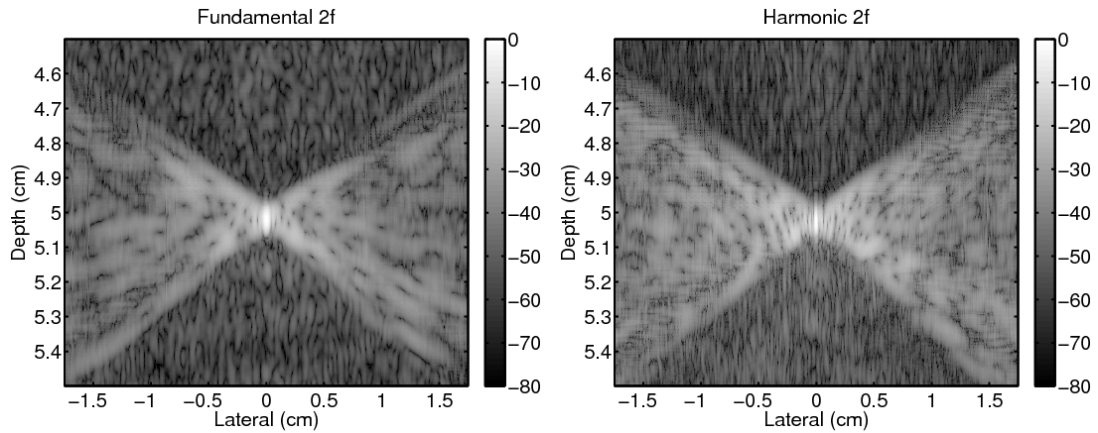


Figure 7.9: Fundamental and harmonic point spread functions from propagation through a representation of the abdominal wall. The source pressure is 1 MPa, the aperture is $F/1$, and the transmit frequency was doubled to 4.2 MHz.

7.4 Discussion

There are a number of competing physical effects that have a different impact on fundamental and harmonic image formation. The backscattered energy from a point target has a quartic dependence on the frequency of the incident pulse [106] so energy from the harmonic component is preferentially reflected. Competing with this effect is frequency dependent attenuation, which has a linear dependence. Also, the generation of the harmonic component is dependent on the pressure intensity so that a larger surface pressure or a more strongly focused transducer translates into a larger amplitude at the harmonic frequency.

This last effect does not have a significant impact on the image quality. When the pressure is reduced by a factor of five there is practically no difference between the fundamental and harmonic images or the associated PSFs. This suggests that the sources of image degradation observed in the subsequent images are due entirely to other effects.

When the aperture is reduced by a factor of three there is a strong reduction in the CNR for the fundamental image but a weaker degradation for the harmonic. A comparison of the fundamental PSFs for the F/3 and F/1 apertures shows that there is a substantial degradation in all three regions of the PSF indicating that the primary mechanism of clutter related image degradation is from reverberation clutter. For the harmonic PSF there is relatively larger improvement of the PSF in the trailing region suggesting that the mechanism for image improvement is a comparatively reduced effect from pulse lengthening. Equivalently, phase aberration and reverberation clutter play a more significant role in image degradation for the low F/# transducer.

A doubling of the transmit frequency yields a reduction in lesion contrast for

the harmonic image, which is the opposite of what is observed at lower frequencies. The harmonic PSF is degraded primarily in the isochronous volume and the trailing region, indicating that phase aberration and pulse lengthening are worse compared to the fundamental.

7.5 Conclusion

Simulations of nonlinear propagation were used to generate fundamental and harmonic diagnostic ultrasound images of an anechoic lesion beneath an abdominal layer. It was shown that a decrease in the transmit pressure by a factor of five had no discernible effect of the fundamental or harmonic image quality. When the aperture was decreased from $F/1$ to $F/3$ there was a significant reduction in the lesion CNR for the fundamental image but the effect was less pronounced for the harmonic image. Plots of the point spread function suggest that the primary mechanism for image degradation with a reduction in aperture size is due to the increased effect of reverberation clutter and phase aberration, but not pulse lengthening. At the original frequency the CNR for the lesion in the harmonic image was significantly better than the CNR for the fundamental image in all considered cases. However, when the transmit frequency was doubled, the contrast of the lesion in the harmonic image was worse than the contrast in the fundamental image. The point spread functions showed that phase aberration and pulse lengthening were worse in harmonic propagation.

7.6 Acknowledgments

This work was supported by NIH grants R01-HL075485 and R01-CA114093-02.

Chapter 8

The effects of nonlinearity on displacements induced by acoustic radiation force in tissue

8.1 Introduction

Acoustic Radiation Force Impulse (ARFI) imaging is a radiation force based imaging method that provides information about the local mechanical properties of tissue [75–77]. ARFI imaging uses short duration acoustic radiation forces to generate localized displacements in tissue, and these displacements are tracked using ultrasonic correlation based methods [88, 90]. The tissue response to these forces is monitored both spatially and temporally. The feasibility of using radiation force to image the mechanical properties of tissues has been investigated by several groups [17, 45, 98] and it has been demonstrated in a wide range of clinical applications including vascular, breast, abdominal, and colon imaging [43, 76, 84, 97]. ARFI imaging has also been used to visualize thermally- and chemically-induced lesions in soft tissue [44].

ARFI relies on the acoustic phenomenon whereby the propagation of acoustic waves through an attenuating or reflecting medium transfers momentum from the wave to the medium. This transfer of momentum results in a body force in the direction of propagation and can be described, neglecting reflections, by the equation [79, 113]:

$$\vec{F} = \frac{\vec{W}_{\text{absorbed}}}{c} \approx \frac{2\alpha\vec{I}}{c} \quad (8.1)$$

where F is the acoustic radiation force, W_{absorbed} is the absorbed power, c is the

speed of sound, α is the absorption coefficient, and I is the pulse averaged acoustic intensity. The approximation on the right hand side of Eq. 8.1 can be derived by assuming that the radiation force is caused by a linearly traveling plane wave [80].

Experimental investigations of the enhancement of acoustic streaming in fluids have established a nonlinear increase in streaming velocities with an increase in pressure [78, 100]. These studies support the hypothesis that as the pressure intensity enters the nonlinear regime the frequency spectrum of the acoustic signal migrates to higher frequencies and, because fluids have a frequency squared dependent attenuation that increases with frequency, this translates to a greater overall absorption and therefore a greater force with which streaming is induced [126]. It has been hypothesized that this same effect may have an important role in the radiation forces induced in tissue by elasticity imaging techniques, even though the attenuation in tissue is linear with frequency [96]. The goal of this paper is to quantify the effects of nonlinear acoustic propagation on ARFI imaging induced displacements with three dimensional acoustic and mechanical numerical models.

A full-wave equation that describes nonlinear propagation in a heterogeneous attenuating medium is solved numerically with a novel method that uses finite differences in the time domain (FDTD). Three dimensional solutions of the equation have been previously verified with water tank measurements of a commercial diagnostic ultrasound transducer and have been shown to be in excellent agreement in terms of the fundamental and harmonic acoustic fields, and the power spectrum at the focus. The linear and nonlinear components of the algorithm have also been verified independently. In the linear non-attenuating regime, solutions match results from Field II, a well established software package used in transducer modeling [60, 61], to within 0.3 dB. Nonlinear plane wave propagation has been shown to closely match results from the Galerkin method up to four times the fundamental frequency. In addition

to thermoviscous attenuation the method calculates the numerical solution of the relaxation attenuation laws that allows modeling of arbitrary frequency dependent attenuation, such as that observed in tissue.

The intensity calculated by the acoustic model is used as an input to the mechanical model. This finite element method (FEM) model accurately simulates the dynamic response of homogeneous tissue to an impulsive radiation force excitation [83]. This paper examines four different acoustic configurations of the transducer. A control with a typical ARFI pushing pulse, a reduced intensity pulse, a medium without nonlinearity, and a variation of the $F/\#$. The spatial distribution of the intensities and absorption losses are compared in the lateral axial plane and their relative magnitudes are examined axially. The differences in the acoustic fields are related to the differences in the calculated displacements.

8.2 Methods

The nonlinear full-wave equation describes acoustic fields in a nonlinear thermoviscous medium [52, 127]. It incorporates the effects of nonlinearity, attenuation, and all wave effects, such as multiple scattering, reflection, and refraction. It can be written as

$$\nabla^2 p - \frac{1}{c_0^2} \frac{\partial^2 p}{\partial t^2} + \frac{\delta}{c_0^4} \frac{\partial^3 p}{\partial t^3} + \frac{\beta}{\rho c_0^4} \frac{\partial^2 p^2}{\partial t^2} + \frac{1}{\rho} \nabla p \cdot \nabla \rho - \sum_{m=1}^v \xi_m = 0 \quad (8.2)$$

where ξ_m satisfies the equation

$$\dot{\xi}_m + \omega_m \xi_m = a_m \omega_m \frac{\Delta c}{c_0} \nabla^2 p \quad (8.3)$$

The first two terms in Eq. 8.2 represent the linear wave equation, the third term

accounts for thermoviscous diffusivity, followed by nonlinearity, variations in density, and v relaxation mechanisms. Here p is the acoustic pressure, c_0 and ρ are the equilibrium speed of sound and density, δ is the acoustic diffusivity, and β is the nonlinearity parameter. The nonlinear parameter B/A is related to the coefficient, β , by $\beta = 1 + B/2A$ and the diffusivity δ can be expressed as a function of the absorption coefficient α with the equation $\delta = 2\alpha c_0^3/\omega^2$ (where ω is the angular frequency). The material parameters c_0 , δ , ρ and β can be functions of space. The relaxation equation (Eq. 8.3) has v peaks at characteristic frequencies ω_m with weight a_m that depend on the particular frequency dependent attenuation law being modeled.

This equation was solved using finite differences in the time domain and solutions have been extensively verified with water tank measurements of a commercial diagnostic ultrasound transducer, comparisons with a Field II [60, 61], and solutions of Burgers' equation. Perfectly matched layers are used at the simulation boundaries to reduce reflections by approximately 80 dB [13, 21, 70]. Full details of the numerical methods and their verification can be found in Pinton et. al [87].

The FEM model used to calculate the dynamic tissue response from the acoustic intensity fields has been validated with calibrated tissue mimicking phantoms. It has shown good agreement in the calculation of shear wave speed, and therefore elasticity. For a full discussion of the model, its validation, and applications the reader is referred to the references [82, 83]. The FEM models of elastic soft tissues were used to compare the dynamic displacement fields generated in response to a 400 cycle (182 μ s) excitation in a $\mu = 2$ kPa material. The Poisson's ratio was 0.499 and the density was 1.0 g/cm³. Single point quadrature was utilized over a mesh consisting of 1.3e6 elements with Flanagan-Belytschko stiffness form hourglass control. The models were solved using LS-DYNA3D (Livermore Software Technology Corporation) using an explicit, time-domain algorithm.

Typical acoustic radiation force magnitudes were computed using the time-domain pressure waveforms solved using the full nonlinear wave equation for a source pressure of 3.5 MPa at 2.2 MHz, focused at 3.75 cm using an F/2 focal configuration without apodization, which will be referred to as the control. For a second simulation the surface pressure was reduced to 1 MPa. In the third simulation the acoustic propagation was through a linear medium so that the spatial distribution of intensity and absorption loss is independent of pressure. The final simulation reduces the aperture from F/2 to F/3 and increases the surface pressure by a factor 3/2 to maintain the same approximate intensity at the focus.

Acoustic radiation forces, \vec{F} , were computed as point loads at each node in the mesh using Eq. 8.1 where $\alpha = 0.7$ dB/cm/MHz and $c = 1540$ m/s. Displacement fields and energy quantities were extracted from the model using LS-PREPOST2 (Livermore Software Technology Corporation).

8.3 Results

8.3.1 Acoustic simulations

The lateral-axial intensity plane at the focus is shown in Fig. 8.1 for (from left to right) the 3.5 MPa control, the surface pressure reduced by a factor of 3.5 to 1 MPa, a linear medium, and an F/3 configuration instead of F/2. The intensities represent the pulse average, each plot is normalized relative to its own peak, and the color map shows large intensities as red and low intensities as blue. The overall spatial distribution of the intensities is similar, though with an increase in the nonlinear propagation or surface pressure the intensity is larger in the near-field. A comparison of the control with zero nonlinearity plot, for example, shows visibly less energy at the

3.75 cm focus and the lobes between 1.75 and 3 cm. The reduced aperture plot, on the far right, has an even more pronounced accumulation of energy in the near-field.

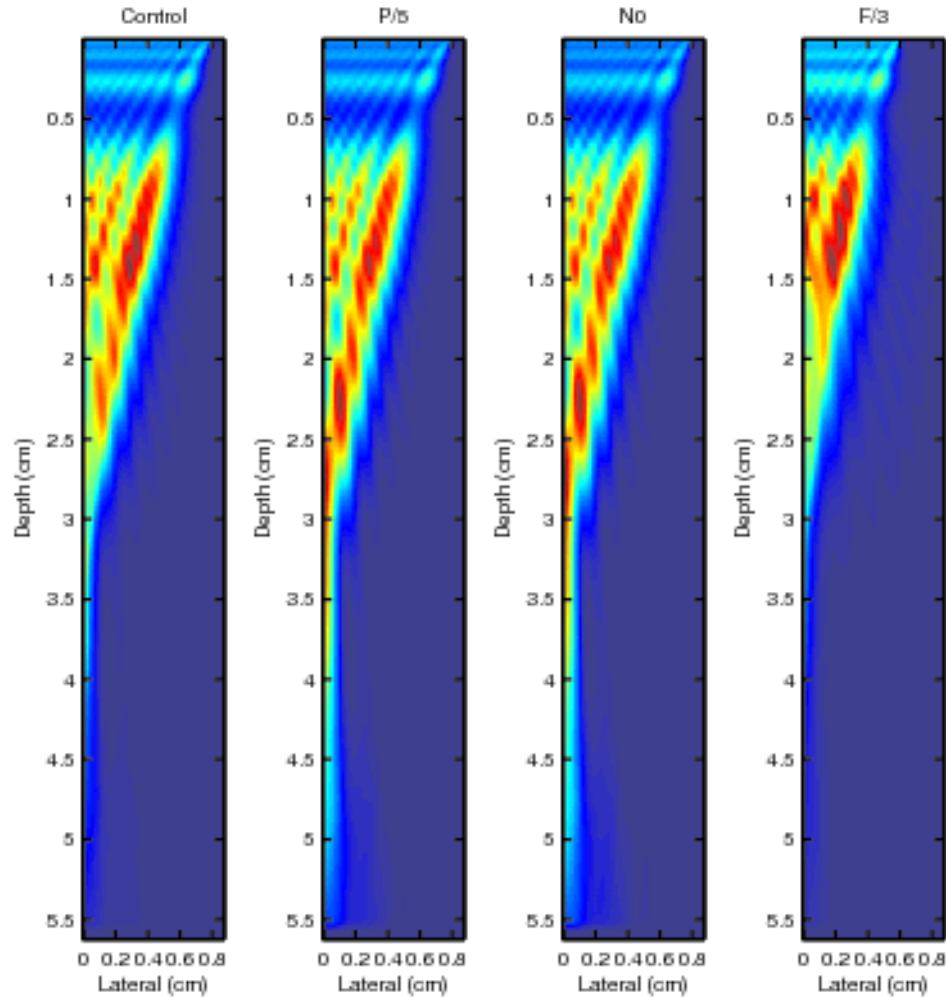


Figure 8.1: Normalized intensity in the lateral axial plane for (from left to right) the ARFI control, the surface pressure reduced by a factor of 3.5 to 1 MPa, a linear medium, and an F/3 configuration instead of F/2. The intensities are normalized relative to their peak and the color map shows large intensities as red and low intensities as blue.

Figure 8.2 plots the loss intensity on the same lateral-axial plane. The loss intensity was calculated by integrating the pulse averaged intensity of the absorbed pressure. Each plot is normalized relative to its peak. In contrast to the previous

intensity plots (Fig. 8.1) the spatial distribution of the loss is markedly different. As the nonlinearity decreases, from the 3.5 MPa control to 1 MPa to the linear medium, there is a substantial shift of the energy distribution into the near-field. For the nonlinear plot the greatest loss clearly occurs at the focus, whereas in the intensity field in Fig. 8.1 the geometric focus did not appear to have significantly higher intensity than the near-field. This effect is also visible in the F/3 plot but it loses more energy away from the focus when compared to the equivalent F/2 control (on the left). The spatial distribution of the intensity in the linear medium is identical to the loss intensity, as predicted by theory.

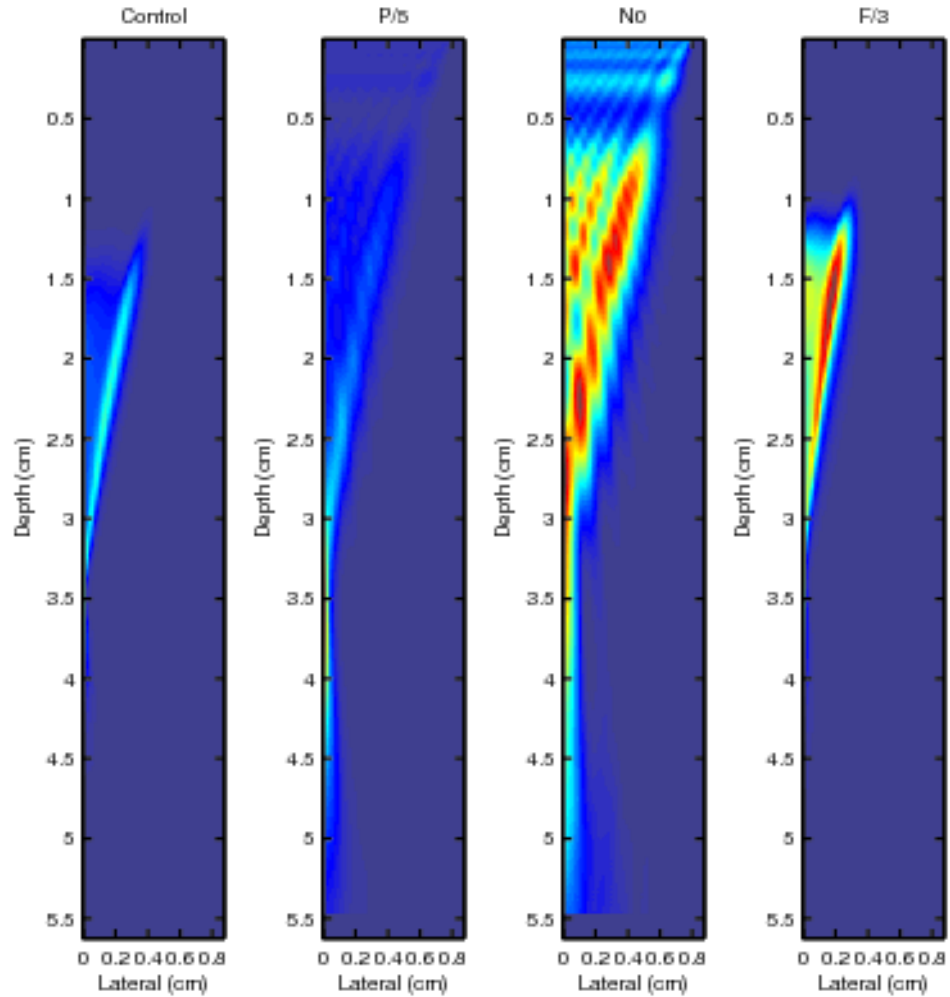


Figure 8.2: Normalized loss calculated as the intensity of the absorbed acoustic pressure in the lateral axial plane for (from left to right) the ARFI control, the surface pressure reduced by a factor of 3.5 to 1 MPa, a linear medium, and an F/3 configuration instead of F/2. The loss intensities are normalized relative to their peak.

A plot of the intensity along the axis normalized by values at the transducer face is shown on the left of Fig. 8.3 and the equivalent plot is shown for the loss on the right. The 1 MPa (red) and linear (blue) curves are very similar throughout the considered depth. With an increase of the surface pressure to 3.5 MPa (blue) the near-field remains similar but the curves diverge significantly starting at 2 cm. Note

that the geometric focus does not necessarily match the highest intensity. The curves of intensity of the loss, shown on the right side of the figure, are significantly different. The loss at the focus for the nonlinear control simulation is approximately 20 times larger than the equivalent linear loss and eight times larger than the 1 MPa case. Compared to the intensity, the loss for the two nonlinear curves is more strongly concentrated at the focus. The peak intensity for the 1 MPa simulation is at 2.7 cm but the peak loss is at 3.5 cm, which is much closer to the 3.75 cm focus.

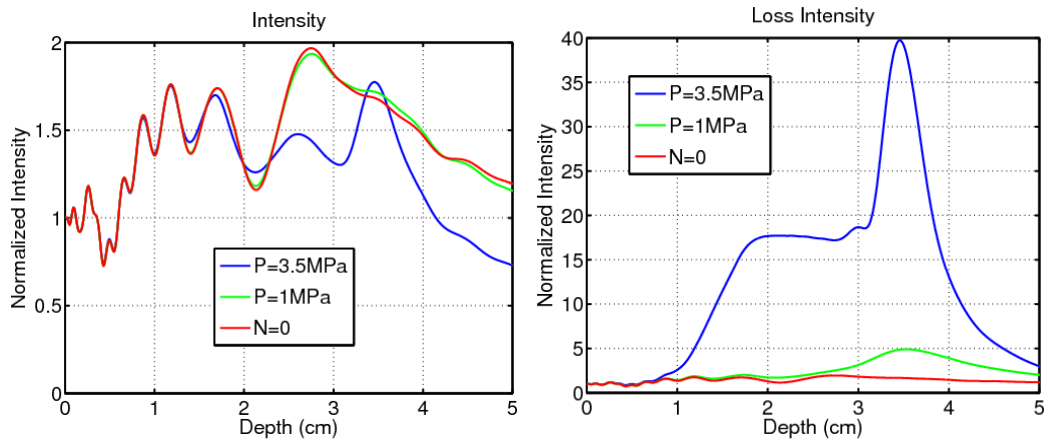


Figure 8.3: Relative intensity (left) and loss intensity (right) for the control (3.5 MPa, blue), the reduced intensity (1 MPa, green), and linear propagation ($N=0$, red) along the axis calculated from pressures normalized by values at the transducer face.

The normalized axial intensity (blue) and loss intensity (dashed red) are plotted on the same axes in Fig. 8.4 to verify that they are equivalent when scaled. There is no discernible difference between the curves.

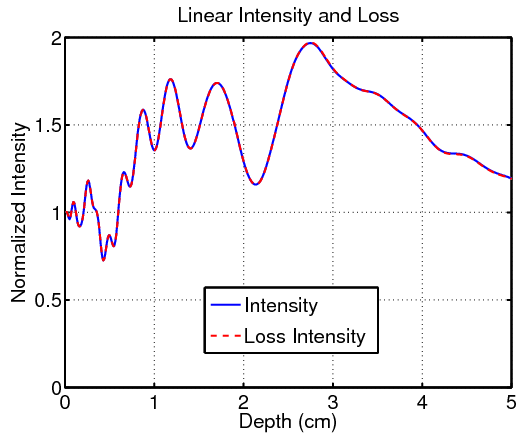


Figure 8.4: Relative intensity (blue) and loss intensity (dashed red) for the linear propagation ($N=0$) along the axis calculated from pressures normalized by values at the transducer face. As predicted by theory, the curves are scaled versions of each other.

The axial intensity and loss intensity are also plotted for the F/2 control (blue) and a reduced F/3 aperture (magenta) in Fig. 8.5. As would be expected of a more strongly focused transducer, the axial intensity is relatively larger for the F/2 aperture near the focus. The loss intensity plots for the F/3 show less loss at the focus but more loss in the region preceding the focus.

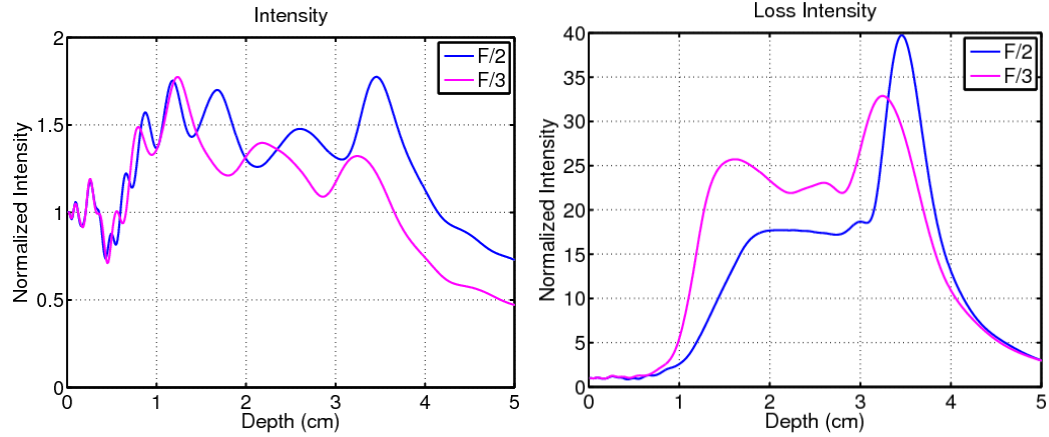


Figure 8.5: Relative intensity (left) and loss intensity (right) for the control (F/2, blue) and the decreased aperture (F/3, magenta) along the axis calculated from pressures normalized by values at the transducer face.

8.3.2 FEM model

Shown in Fig. 8.6 are the axial displacement profiles over the three dimensional quarter symmetry model, 1.2 ms after the cessation of the radiation force excitation by the linear (left) and nonlinear (right) intensities. Both images use a color bar with a maximum of $15 \mu\text{m}$ of displacement (red). It is clear from these images that the displacement calculated with the linear intensity is greater in the focal region, indicating better penetration. The displacement in the nearfield is similar in both cases.

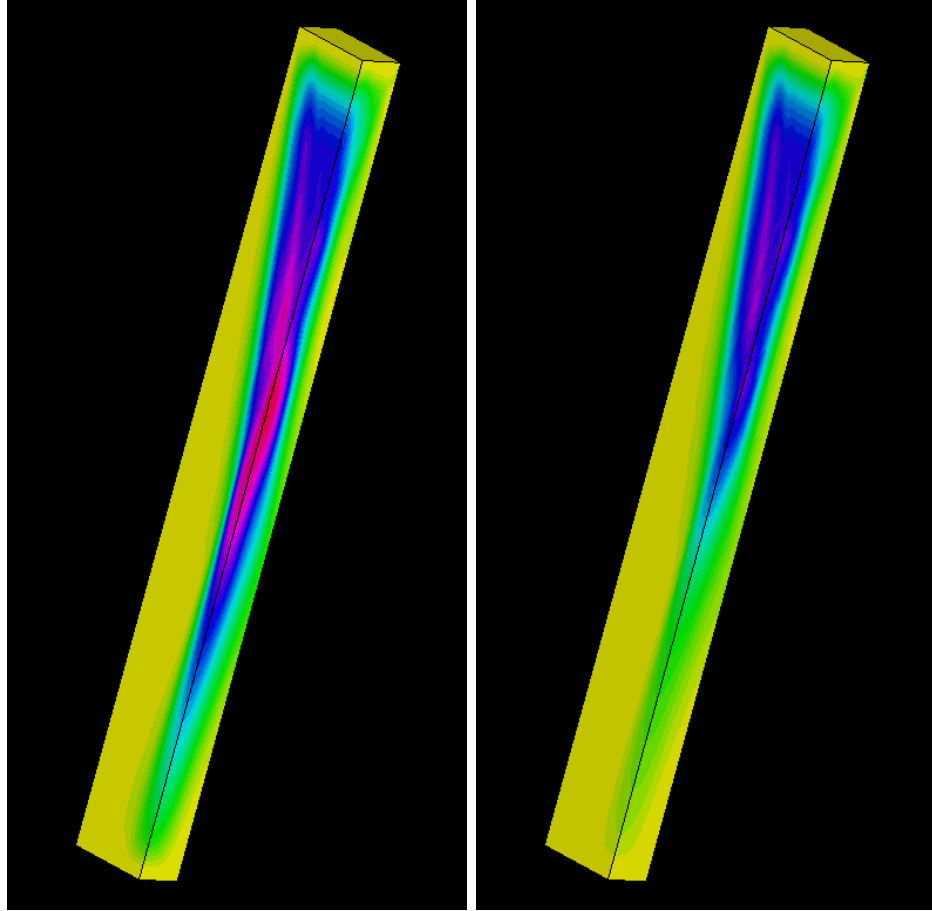


Figure 8.6: The axial displacement profiles over the 3D quarter symmetry model, 1.2 ms after the cessation of the radiation force excitation as calculated from the linear (left) and nonlinear (right) intensities. Both images use a color bar with a maximum of $15 \mu\text{m}$ of displacement (red)

The plot in Fig. 8.7 shows the axial displacement profiles in the center of the region of excitation for the (blue) and nonlinear (red) acoustic intensity fields. At the focal depth, the pulse average intensity (I_{sppa}) is 1000 W/cm^2 for the linear ($\beta = 0$) simulation and 784 W/cm^2 for the nonlinear ($\beta = 5$) simulation. Peak axial displacement in the center of the region of excitation occurs at 2.4 cm for the linear simulation and is 1.15 cm shallower for the nonlinear simulation at 1.25 cm in depth. The peak positive displacement for the linear curve is 43% larger.

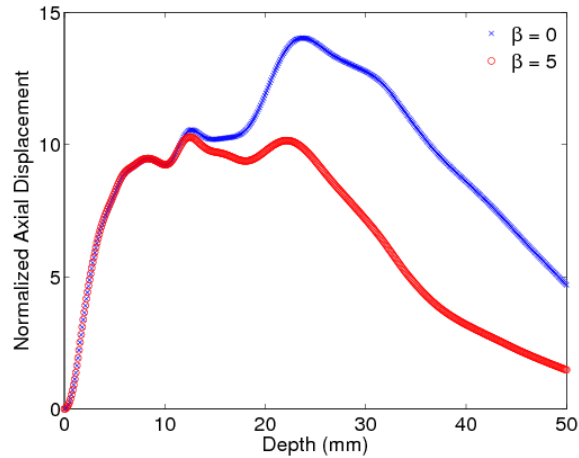


Figure 8.7: The axial displacement profiles in the center of the region of excitation for the linear ($\beta = 0$) and nonlinear ($\beta = 5$) control acoustic intensity fields.

Normalized plots of the lateral (left) and elevation (right) displacements are shown in Fig. 8.8. In the lateral plot, the nonlinear curve has a wider distribution of its displacement in the region between 0.5 and 1.5 cm but for large lateral displacements it is similar to the linear case. This effect is observable to a reduced extent in the elevation plane. In both cases there is almost no difference in the full width at half of the maximum (FWHM).

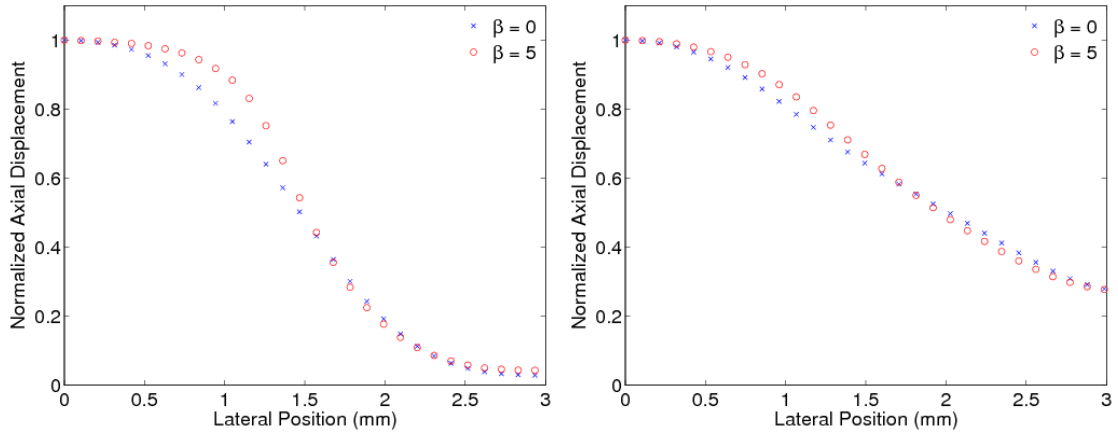


Figure 8.8: Normalized lateral (left) and elevation (right) displacement profiles at the focal depth for the linear ($\beta = 0$) and nonlinear ($\beta = 5$) control acoustic intensity fields.

8.4 Discussion

Differences in the intensities and losses are consistent with the understanding that larger pressures transfer energy to higher frequencies which are in turn preferentially absorbed by frequency dependent attenuation. As can be observed in Fig. 8.1 an increase in the surface pressure is associated with a relative decrease of energy at the focus. The increased pressure leads to the nonlinear distortion of the wave at a shallower depth so it is more attenuated compared to a linear wave. For the 3.5 MPa simulation, the absorption shown in Fig. 8.3 is nine times larger in the 2-3 cm region and 20 times larger at the focus, corroborating this explanation.

Even though the intensity is lower at the focus for the nonlinear simulations, the absorbed energy is much larger. As the pulse reaches the focus there is an accumulation of energy at the higher frequencies from propagation. The energy content of the acoustic signal at the focus is therefore at a much higher frequency and the associated absorption is large, which more than compensates for the reduced

intensity.

The loss distribution shown in Fig. 8.2 is more strongly concentrated about the focus for the nonlinear simulations. Plots of the loss in Fig. 8.3 are along the axis where the pressure is largest and the effects of nonlinearity are strongest. However the overall area where the absorption is enhanced by nonlinearity is small compared to the region in the linear regime suggesting that the radiation force may be much larger in a subset of theinsonified region but on average it may not be dissimilar from the linear case.

A three dimensional visualization of the FEM model in Fig. 8.6 shows that the displacements in the focal region, where the effects of nonlinearity are strongest, are significantly larger than that for the linear simulation. The FEM simulation also indicates that nonlinearity plays an important role in determining the penetration of ARFI. The on-axis displacement are up to 43% larger for the displacements calculated from the linear intensity. The displacement magnitude has a significant effect on the signal to noise ratio (SNR) of ARFI imaging.

The extent of the displacement in the lateral and elevation dimensions is related to the resolution of the ARFI imaging system. As shown in Fig. 8.8 there is practically no difference in the FWHM indicating the benefits in penetration and SNR are not offset by losses in lateral or elevation resolution.

8.5 Conclusion

Nonlinear acoustic propagation has an important effect on acoustic radiation force and the displacements it induces. The acoustic models presented in this paper characterized the nonlinear acoustic intensities and associated absorption losses for various ultrasonic transducer configurations. Nonlinearity has a moderate effect on the inten-

sity of an ARFI push pulse, which is observable primarily as a reduction in intensity in the focal region. However, nonlinearity has a large effect on the absorption loss, which determines the amount of radiation force. For a typical ARFI pulse the absorption loss was 20 times larger for the nonlinear field compared to the linear field at the focus.

The acoustic loss was used as an input to an FEM model of the mechanical tissue properties to characterize and quantify how differences between the linear and nonlinear acoustic fields affect displacement induced by radiation force. By including the effects of nonlinearity a displacement field that is up to 43% larger was predicted. The largest differences occurred at the focus, where the effects of nonlinear acoustic propagation are strongest. The nonlinear model derived from the intensity field predicted significantly smaller penetration but there was no reduction in the lateral or elevation resolution.

8.6 Acknowledgments

This work was supported by NIH grants R01-HL075485 and 1R01-CA114093-02.

Chapter 9

Conclusions and Future Work

9.1 Conclusions

Describing discontinuities with numerical methods presents particular challenges. Flux conserving numerical methods perform better than implicit solution based methods when applied to the KZK equation because they do not require grid refinement with a reduction in attenuation. These schemes satisfy the Rankine-Hugoniot relation at all attenuation values with no changes in the grid size. Implicit solution based methods, on the other hand require a number of grid points that is six orders of magnitude larger than an equivalent Godunov or MUSCL based simulation for a typical lithotripsy simulation.

A new numerical method for highly nonlinear ultrasonic wave propagation was presented. The numerical investigation demonstrated that the KZK equation augmented with cubic nonlinearity has an important effect at pressure amplitudes such as those encountered in shock wave lithotripsy, especially for the peak positive pressure.

The KZK equation relies on the paraxial approximation to describe the diffraction which is not a valid assumption for many ultrasonic transducers. When compared to numerical solutions of the full-wave equation, the parabolic equation has significant error in the focus and lateral beamplots. Since these two metrics are crucial in describing the imaging characteristics of ultrasound scanners a nonlinear version of the full-wave equation was pursued.

A finite difference time domain algorithm that solves the nonlinear attenuating full-wave equation in three spatial dimensions was established. The numerical method

propagates nonlinear diagnostic ultrasound waves in an heterogeneous attenuating medium with boundary conditions that reduce reflections to negligible levels. The entire acoustic field is simulated so the effects of reflection, reverberation, multiple scattering, and clutter can be accurately modeled and an arbitrary acoustic source can be placed anywhere in the three dimensional simulated field.

The numerical solutions were verified extensively and were shown to have excellent agreement with theory and experiment. Diffraction, or the linear wave term, was verified with Field II. Comparisons of the measured and simulated focal plane of a diagnostic ultrasound transducer exhibited the same primary and secondary features with respect to the position and amplitude of the mainlobe and sidelobes for both the fundamental and harmonic components. A comparison of the power spectrum at the focus also showed excellent agreement. The nonlinear propagation was also verified numerically with results from the Galerkin method for a propagating plane wave and were shown to be in good agreement.

We demonstrated the code's ability to propagate sound through heterogeneous media by transmitting an ultrasound pulse through a measured representation of human abdominal wall.

A numerical method that solves the nonlinear attenuating wave equation in heterogeneous media was used to determine, for the first time, the primary sources of clutter in fundamental and harmonic imaging. A new framework for describing and understanding the sources of image degradation was presented. There are three distinct conclusions that can be drawn from the presented clutter data.

First the primary source of image degradation in the fundamental PSF comes from reverberation in the near-field abdominal structures. Second phase aberration is the largest source of clutter in the harmonic PSF. Finally clutter in the PSFs occurs primarily from low level contributions distributed over a large area.

It was shown that a decrease in the transmit pressure by a factor of five had no discernible effect of the fundamental or harmonic image quality. When the aperture was decreased from F/1 to F/3 there was a significant reduction in the lesion CNR for the fundamental image but the effect was less pronounced for the harmonic image. The primary mechanism for image degradation with a reduction in aperture size is due to the increased effect of reverberation clutter and phase aberration, but not pulse lengthening. Increasing the frequency causes an increase in phase aberration and pulse lengthening in the harmonic PSF compared to the fundamental PSF.

Nonlinear acoustic propagation has an important effect on acoustic radiation force and the displacements it induces. Nonlinearity has a moderate effect on the intensity of an ARFI push pulse which is observable primarily as a reduction in intensity in the focal region. However nonlinearity has a large effect on the absorption loss, which determines the amount of radiation force.

The acoustic intensity was used as an input to an FEM model of the mechanical tissue properties to characterize and quantify how differences between the linear and nonlinear acoustic fields affect displacement induced by radiation force. By including the effects of nonlinearity a displacement field significantly smaller was predicted. The largest differences occurred at the focus, where the effects of nonlinear acoustic propagation are strongest. The nonlinear model predicted significantly smaller penetration but there was no reduction in the lateral or elevation resolution.

9.2 Future Work

9.2.1 Three dimensional PSFs

Due to computational constraints the ultrasound images and PSFs presented in this dissertation are based on two dimensional heterogeneous models. Incorporating the third dimension would allow a more realistic simulation of physical models and would also elevation focusing in the transducer. The position of the elevation focus can be tuned to optimize harmonic imaging and simulations would be able to quantify characterize and optimize improvements for heterogeneous media.

9.2.2 Effect of scatterer brightness and non-Rayleigh distribution

Tissue is known not to follow lower power laws than f^4 for backscatter. This difference has the potential to affect image quality estimates for harmonic imaging because it would lower the amount of reflected energy at the harmonic frequency compared to the fundamental.

9.2.3 The effects of nonlinearity on tissue heating

It was shown in this dissertation that the inclusion of nonlinearity can induce highly localized regions of very intense acoustic loss. Although the studies were performed in the context of tissue displacement the same losses can be used to calculate tissue heating. The factor of 20 increase in loss due to nonlinearity is remarkably high and is difficult to verify experimentally.

Appendix A

Derivation of B/A

The Taylor series expansion of the equation of state $P = P(\rho, s)$ yields

$$P - P_0 = \left(\frac{\partial P}{\partial \rho} \right)_{s,0} (\rho - \rho_0) + \frac{1}{2!} \left(\frac{\partial^2 P}{\partial \rho^2} \right)_{s,0} (\rho - \rho_0)^2 + \dots \quad (\text{A.1})$$

where P and ρ are the pressure and density, P_0 and ρ_0 are the equilibrium values, and s is the specific entropy. This equation can be rearranged to obtain

$$p = A \left(\frac{\rho'}{\rho_0} \right) + \frac{B}{2!} \left(\frac{\rho'}{\rho_0} \right)^2 + \frac{C}{3!} \left(\frac{\rho'}{\rho_0} \right)^3 + \dots \quad (\text{A.2})$$

where $p = P - P_0$ is the excess pressure (or sound), $\rho' = \rho - \rho_0$ is the excess density, and

$$A = \rho_0 \left(\frac{\partial P}{\partial \rho} \right)_{s,0} \equiv \rho_0 c_0^2 \quad (\text{A.3})$$

$$B = \rho_0^2 \left(\frac{\partial^2 P}{\partial \rho^2} \right)_{s,0} \quad (\text{A.4})$$

$$C = \rho_0^3 \left(\frac{\partial^3 P}{\partial \rho^3} \right)_{s,0} \quad (\text{A.5})$$

Note that the small signal speed of sound, c_0 is defined in eqn. A.3. The parameter B/A as defined above can then be written as

$$\frac{B}{A} = \frac{\rho_0}{c_0^2} \left(\frac{\partial^2 P}{\partial \rho^2} \right)_{s,0} \quad (\text{A.6})$$

Measuring B/A according to this definition would require varying the density adiabatically. Since liquids have a low compressibility such a measurement would be impractical. Other definitions of B/A rely on variations of the speed of sound c , defined as

$$c^2 = 2\rho_0 c_0 \left(\frac{\partial c}{\partial P} \right)_{s,0} \quad (\text{A.7})$$

from which, using eqn. A.2, we can obtain

$$\frac{c^2}{c_0^2} = 1 + \frac{B}{A} \left(\frac{\partial \rho'}{\partial \rho_0} \right) + \frac{C}{2A} \left(\frac{\partial \rho'}{\partial \rho_0} \right)^2 + \dots \quad (\text{A.8})$$

By taking the square root and performing a binomial expansion we obtain

$$\frac{c}{c_0} = 1 + \frac{B}{2A} \left(\frac{\partial \rho'}{\partial \rho_0} \right) + \frac{1}{4} \left[\frac{C}{A} - \frac{1}{2} \left(\frac{B}{A} \right)^2 \right] \left(\frac{\partial \rho'}{\partial \rho_0} \right)^2 + \dots \quad (\text{A.9})$$

Appendix B

Derivation of the KZK equation

The Westervelt equation is an approximation of the second order wave equation and it is valid when the cumulative nonlinear effects dominate the local nonlinear effects, which become small when the propagation length is greater than a few wavelengths.

$$\left(\nabla^2 - \frac{1}{c_0^2} \frac{\partial}{\partial t}\right) p = -\frac{\delta}{c_0^4} \frac{\partial^3 p}{\partial t^3} - \frac{\beta}{\rho_0 c_0^4} \frac{\partial^2 p^2}{\partial t^2} \quad (\text{B.1})$$

The term on the left hand side is the 3D wave equation and the terms on the right hand side are diffusion and nonlinearity. The KZK equation can be derived from the Westervelt equation by picking the correct slow scale.

$$p = p(x_1, y_1, z_1, t'), \quad (x_1, y_1, z_1) = (\epsilon^{1/2}x, \epsilon^{1/2}y, \epsilon z), \quad t' = t - z/c_0 \quad (\text{B.2})$$

This scaling indicates that spatial variations along the axis of the beam occur more slowly than variations across it. The length scale associated for axial variations is the Rayleigh distance $\frac{1}{2}ka^2$ which is greater than a , the transverse length scale, because $ka \gg 1$. To $O(\epsilon^2)$ the Laplacian can be written as

$$\nabla^2 = \epsilon \left(\frac{\partial^2}{\partial x_1^2} + \frac{\partial^2}{\partial y_1^2} \right) + \epsilon^2 \frac{\partial^2}{\partial z_1^2} - \epsilon \frac{2}{c_0} \frac{\partial^2}{\partial z_1 \partial t'} + \frac{1}{c_0^2} \frac{\partial^2}{\partial t'^2} \quad (\text{B.3})$$

The parabolic approximation can be obtained by discarding the $O(\epsilon^2)$ term. This nomenclature comes from the classifications of PDE's—the hyperbolic wave equation (two z derivatives) is approximated by a parabolic equation (one z derivative). Upon

substitution into Eq. B.1 we obtain

$$\epsilon \left(\frac{\partial^2}{\partial x_1^2} + \frac{\partial^2}{\partial y_1^2} \right) - \epsilon \frac{2}{c_0} \frac{\partial^2}{\partial z_1 \partial t'} + \frac{1}{c_0^2} \frac{\partial^2}{\partial t'^2} = -\frac{\delta}{c_0^4} \frac{\partial^3 p}{\partial t'^3} - \frac{\beta}{\rho_0 c_0^4} \frac{\partial^2 p^2}{\partial t'^2} \quad (\text{B.4})$$

Transformation back to the original (x,y,z) spatial coordinates yields the KZK equation

$$\frac{\partial^2 p}{\partial z \partial t'} - \frac{c_0}{2} \nabla_{\perp}^2 p = \frac{\delta}{2c_0^3} \frac{\partial^3 p}{\partial t'^3} + \frac{\beta}{2\rho_0 c_0^3} \frac{\partial^2 p^2}{\partial t'^2} \quad (\text{B.5})$$

Note: this discussion follows the treatment in [52].

Appendix C

Cole-Hopf Transformation

Write Burgers' equation ($p_t + pp_x = \nu p_{xx}$) in conservation law form:

$$\boxed{p_t + (u^2 - \nu p_x)_x = 0} \quad (\text{C.1})$$

Let $p = \Psi_x$ and $\nu p_x - \frac{1}{2}p^2 = \Psi_t$ then substitute former into latter to obtain $\nu\Psi_{xx} - \frac{1}{2}\Psi_x^2 = \Psi_t$.

Also let $\Psi = -2\nu \log \phi$ so that $p = \Psi_x = -2\nu \frac{\phi_x}{\phi}$ (differentiate)

$$\boxed{\Psi_{xx} = 2\nu \left(\frac{\phi_x}{\phi} \right)^2 - \frac{2\nu}{\phi} \phi_{xx}, \quad \Psi_t = -2\nu \frac{\phi_t}{\phi}} \quad (\text{C.2})$$

Burgers' equation reduces to the linear diffusion equation!

$$\boxed{\phi_t = \nu \phi_{xx}} \quad (\text{C.3})$$

For an initial value problem

$$p(x, 0) = F(x) \quad (\text{C.4})$$

$$\phi(x, 0) = \exp \left[-\frac{1}{2\nu} \int_0^x F(\alpha) d\alpha \right] \quad (\text{C.5})$$

Appendix D

Spectral methods

Q: How do you solve Burgers' equation?

A: Consider only periodic disturbances so time dependence can be factored out through a Fourier series representation

$$\boxed{P(\sigma, \theta) = \frac{1}{2} \sum_{n=-\infty}^{\infty} P_n(\sigma) e^{jn\theta}} \quad \text{Trial solution} \quad (\text{D.1})$$

Substitute into Burgers' equation, $\frac{\partial P}{\partial \sigma} = P \frac{\partial P}{\partial \theta} + A \frac{\partial^2 P}{\partial \theta^2}$

$$\sum_{n=-\infty}^{\infty} \left(\frac{dP_n}{d\sigma} + n^2 A P_n \right) e^{jn\theta} = \frac{1}{4} \frac{\partial}{\partial \theta} \sum_{l=-\infty}^{\infty} \sum_{m=-\infty}^{\infty} P_l P_m e^{j(l+m)\theta} \quad (\text{D.2})$$

Let $n' = l + m$ and taking the derivative with respect to θ :

$$= \sum_{n'=-\infty}^{\infty} \left(j \frac{n'}{4} \sum_{m=-\infty}^{\infty} P_m P_{n'-m} \right) e^{jn'\theta} \quad (\text{D.3})$$

The terms in parentheses are equal

$$\frac{dP_n}{d\sigma} + n^2 A P_n = j \frac{n}{4} \sum_{m=-\infty}^{\infty} P_m P_{n-m} \quad (\text{D.4})$$

$$\frac{dP_n}{d\sigma} + n^2 A P_n = j \frac{n}{4} \sum_{m=-\infty}^{\infty} P_m P_{n-m} \quad (\text{D.5})$$

The convolution on the right hand side can be expressed as

$$\sum_{m=-\infty}^{\infty} P_m P_{n-m} = \sum_{m=1}^{n-1} P_m P_{n-m} + 2 \sum_{m=n=1}^{\infty} P_m P_{m-n}^* \quad (\text{D.6})$$

$\boxed{P_m P_{n-m}}$ sum frequency generation

$\boxed{P_m P_{m-n}^*}$ difference frequency generation

Fourier series can be truncated for numerical implementation

$$\boxed{\frac{dP_n}{d\sigma} = -n^2 A P_n + j \frac{n}{4} \left(\sum_{m=1}^{n-1} P_m P_{n-m} + 2 \sum_{m=n=1}^M P_m P_{m-n}^* \right)} \quad (\text{D.7})$$

System of M ODE's, implemented in Matlab

$$\boxed{n^2 A \rightarrow A_n + j D_n} \quad \text{Arbitrary absorption and dispersion} \quad (\text{D.8})$$

Appendix E

Kramers-Krönig Relation

The Kramers-Krönig relates variations in the speed of sound to the absorption law [125]

$$\frac{1}{c(\omega)} = \frac{2}{\pi} \int_0^\infty [\alpha(\omega') - \alpha(\omega)] \frac{d\omega'}{\omega'^2 - \omega^2} \quad (\text{E.1})$$

Bibliography

- [1] Sigurd Ivar Aanonsen, Tor Barkve, Jacqueline Naze Tjøtta, and Sigve Tjøtta. Distortion and harmonic generation in the nearfield of a finite amplitude sound beam. *J. Acoust. Soc. Am.*, 75(3):749–768, March 1984.
- [2] M. A. Averkiou. Tissue harmonic imaging. *IEEE Ultrasonics Symposium*, pages 1563–1572, 2000.
- [3] M. A. Averkiou and R. O. Cleveland. Modeling of an electrohydraulic lithotripter with the KZK equation. *J. Acoust. Soc. Am.*, 106(1):102–112, Jul 1999.
- [4] M. A. Averkiou and M. F. Hamilton. Nonlinear distortion of short pulses radiated by plane and focused circular pistons. *J. Acoust. Soc. Am.*, 102(5):2539–2548, June 1997.
- [5] Michalakis Averkiou and Mark Hamilton. Measurements of harmonic generation in a focused finite-amplitude sound beam. *J. Acoust. Soc. Am.*, 98(6):3439–3442, Dec 1995.
- [6] Michael R. Bailey, Lisa N. Couret, Oleg A. Sapozhnikov, Vera A. Khokhlova, Gail ter Haar, Shahram Vaezy and Xuegong Shi, Roy Martin, and Lawrence A. Crum. Use of overpressure to assess the role of bubbles in focused ultrasound lesion shape in vitro. *Ultrasound Med Biol.*, 27(5):695–708, 2001.
- [7] A. C. Baker. Prediction of non-linear propagation in water due to diagnostic medical ultrasound equipment. *Phys. Med. Biol.*, 36(11):1457–1464, Jun 1991.
- [8] A. C. Baker. Nonlinear pressure fields due to focused circular apertures. *J. Acoust. Soc. Am.*, 91(2):713–717, Feb 1992.
- [9] A. C. Baker, A. M. Berg, Sahin A, and J. N. Tjøtta. The nonlinear pressure field of plane, rectangular apertures - experimental and theoretical results. *J. Acoust. Soc. Am.*, 97(6):3510–3517, Jun 1995.
- [10] A. C. Baker and V. F. Humphrey. Distortion and high-frequency generation due to nonlinear propagation of short ultrasonic pulses from a plane circular piston. *J. Acoust. Soc. Am.*, 92(3):1699–1705, Sep 1992.
- [11] A. C. Baker and V. F. Humphrey K. Anastasiadis. The nonlinear pressure field of a plane circular piston - theory and experiment. *J. Acoust. Soc. Am.*, 84(4):1483–1487, Oct 1988.
- [12] N. S. Bakhvalov, Y. M. Zhileikin, and E. A. Zabolotskaya. *Nonlinear Theory of Sound Beams*. American Institute of Physics, New York, 1987.

- [13] J.-P. Berenger. A perfectly matched layer for the absorption of electromagnetic waves. *J. Comp. Phys.*, 114:185–200, 1994.
- [14] J. Bernsten. Numerical calculations of finite amplitude sound beams. in: M. Hamilton, D. Blackstock, eds. *frontiers of nonlinear acoustics*. London: Elsevier, pages 191–196, 1990.
- [15] L. S. Blackford, J. Choi, A. Cleary, E. D’Azevedo, J. Demmel, I. Dhillon, J. Dongarra, S. Hammarling, G. Henry, A. Petitet, K. Stanley, D. Walker, and R. C. Whaley. *ScaLAPACK Users’ Guide*. Society for Industrial and Applied Mathematics, Philadelphia, PA, 1997.
- [16] Charles Bradley. Mechanisms of image quality improvement in tissue harmonic imaging. volume 838, pages 247–254. AIP, 2006.
- [17] S. Catheline, F. Wu, and M. Fink. A solution to diffraction biases in sonoelasticity: The acoustic impulse technique. *J. Acoust. Soc. Am.*, 105:2941–2950, 1999.
- [18] C. G. Chaussy and G. J. Fuchs. Current state and future developments of noninvasive treatment of human urinary stones with extracorporeal shock wave lithotripsy. *J. Urol.*, 141(3):782–789, 1989.
- [19] C. Schmiedt Chaussy, D. Brendel E. Jocham, B. W. Forssmann, and V Walther. First clinical experience with extracorporeally induced destruction of kidney stones by shock waves. *Journal of Urology*, 167:1957–1960, 1982.
- [20] Lili Chen, Gail ter Haar, and Christopher R. Hill. Influence of ablated tissue on the formation of high-intensity focused ultrasound lesions. *Ultrasound Med Biol.*, 23(6):921–931, 1997.
- [21] W. C. Chew and Q. H. Liu. Perfectly matched layers for elastodynamics: A new absorbing boundary condition. *J. Comput. Acoust.*, 4(4):72–79, 1996.
- [22] W. C. Chew and W. H. Wheedon. A 3D perfectly matched medium from modified maxwell’s equations with stretched coordinates. *Microw. Opt. Technol. Lett.*, 7:599–604, 1994.
- [23] Sabina Choudhry, Brian Gorman, J. William Charboneau, Donald J. Tradup, Rebecca J. Beck, James M. Kofler, and Debra S. Groth. Comparison of tissue harmonic imaging with conventional us in abdominal disease. *RadioGraphics*, 20:1127–1135, 2000.
- [24] Douglas Christensen. *Ultrasonic Bioinstrumentation*. John Wiley and Sons, 1988.

- [25] T. Christopher. Modeling the Dornier-HM3-lithotripter. *J. Acoust. Soc. Am.*, 96(5):3088–3095, Nov 1994.
- [26] T. Christopher. Finite amplitude distortion and its relationship to linear derating formulae for diagnostic ultrasound systems. *Ultrasound in Medicine and Biology*, 22(8):1103–1116, 1996.
- [27] T. Christopher. Finite amplitude distortion-based inhomogeneous pulse echo ultrasonic imaging. *IEEE Transactions on Ultrasonics Ferroelectrics and Frequency Control*, 44(1):125–139, 1997.
- [28] T. Christopher. Experimental investigation of finite amplitude distortion-based, second harmonic pulse echo ultrasonic imaging. *IEEE Transactions on Ultrasonics Ferroelectrics and Frequency Control*, 45(1):158–162, 1998.
- [29] T. Christopher. Computing the mechanical index. *Journal of Ultrasound in Medicine*, 18(1):63–68, 1999.
- [30] Ted Christopher and Kevin J. Parker. New approaches to nonlinear diffractive field propagation. *J. Acoust. Soc. Am.*, 90(1):488–499, Jul 1991.
- [31] Ted Christopher and Kevin J. Parker. New approaches to the linear propagation of acoustic fields. *J. Acoust. Soc. Am.*, 90(1):507–521, Jul 1991.
- [32] R. O. Cleveland, M. F. Hamilton, and D. T. Blackstock. Time-domain modeling of finite-amplitude sound in relaxing fluids. *J. Acoust. Soc. Am.*, 99(6):3312–3318, Jun 1996.
- [33] R. O. Cleveland, D. A. Lifshitz, B. A. Connors, A. P. Evan, L. R. Willis, and L. A. Crum. In vivo pressure measurements of lithotripsy shock waves in pigs. *Ultrasound in Medicine and Biology*, 24(2):293–306, Feb 1998.
- [34] R. H. Cole. *Underwater Explosions*. Princeton University Press, Princeton, 1948.
- [35] A. J. Coleman, J. E. Saunders, L. A. Crum, and M. Dyson. Acoustic cavitation generated by an extracorporeal shockwave lithotripter. *Ultrasound Med Biol.*, 13(2):69–76, Feb 1987.
- [36] L. A. Crum. Cavitation jets as a contributory mechanism for renal calculi disintegration in ESWL. *Journal of Urology*, 140:1587–1590, 1988.
- [37] Terry S. Desser, R. Brooke Jeffrey, Michael J. Lane, and Philip W. Ralls. Pictorial essay: Tissue harmonic imaging: Utility in abdominal and pelvic sonography. *Journal of Clinical Ultrasound*, 27(3):135–142, March/April 1999.

- [38] FA Duck. Nonlinear acoustics in diagnostic ultrasound. *Ultrasound in Medicine and Biology*, 28(1):1–18, Jan 2002.
- [39] H. W. Durgin, P. D. Freiburger, D. C. Sullivan, and G. E. Trahey. Large aperture phase error measurement and effects. volume 1, pages 623–627, 1992.
- [40] Helga Emmerich and Michael Korn. Incorporation of attenuation into time-domain computations of seismic waves. *Geophys.*, 52(9):1252–1264, 1987.
- [41] Bjorn Engquist and Andrew Majda. Absorbing boundary conditions for the numerical simulation of waves. *Mathematics of Computation*, 31(139):629–651, Jul. 1977.
- [42] Andrew P. Evan, Lynn R. Willis, James E. Lingeman, and James A. McAteer. Renal trauma and the risk of long-term complications in shock wave lithotripsy. *Nephron*, 78(1):1–8, 1998.
- [43] B.J. Fahey, K.R. Nightingale, R.C. Nelson, M.L. Palmeri, and G.E. Trahey. Acoustic radiation force impulse imaging of the abdomen: demonstration of feasibility and utility. *Ultrasound Med. Biol.*, 31(9):1185–1198, Sep 2005.
- [44] B.J. Fahey, K.R. Nightingale, D.L. Stutz, and G.E. Trahey. Acoustic radiation force impulse imaging of thermally- and chemically-induced lesions in soft tissues: preliminary ex vivo results. *Ultrasound Med. Biol.*, 30(3):321–328, 2004.
- [45] M. Fatemi and J. F. Greenleaf. Application of radiation force in noncontact measurement of the elastic parameters. *Ultrasonic Imaging*, 21:147–154, 1999.
- [46] Matteo Frigo and Steven G. Johnson. The design and implementation of FFTW3. *Proceedings of the IEEE*, 93(2):216–231, 2005. special issue on Program Generation, Optimization, and Platform Adaptation.
- [47] Francis J. Fry, Narendra T. Sanghvi, Richard S. Foster, Richard Bihrlé, and Carl Hennige. Ultrasound and microbubbles: Their generation, detection and potential utilization in tissue and organ therapy—experimental. *Ultrasound Med Biol.*, 21(9):1227–1237, 1995,.
- [48] S. K. Godunov. A finite difference method for the numerical computation and discontinuous solutions of the equations of fluid dynamics. *Mat. Sb.*, 47:271–306, 1959.
- [49] S. A. Goss, R. L. Johnston, and F. Dunn. Compilation of empirical ultrasonic properties of mammalian tissues. 64(2):423–457, 1978.
- [50] S. A. Goss, R. L. Johnston, and F. Dunn. Compilation of empirical ultrasonic properties of mammalian tissues, II. 68(1):93–108, 1980.

- [51] Ibrahim M. Hallaj and Robin O. Cleveland. Fdtd simulation of finite-amplitude pressure and temperature fields for biomedical ultrasound. *J. Acoust. Soc. Am.*, 105(5):L7–L12, May 1999.
- [52] M. F. Hamilton and D. T. Blackstock. *Nonlinear Acoustics*. Academic Press, San Diego, 1997.
- [53] Mark F. Hamilton, Jacqueline Naze Tjøtta, and Sigve Tjøtta. Nonlinear effects in the farfield of a directive sound source. *J. Acoust. Soc. Am.*, 78(1):202–216, July 1985.
- [54] D. Hassler, W. Härer, G. Temme, E. Schmidt, P. Wegener, and P. Krämmer. Degradation of image quality by sound velocity fluctuations and its dependence on the aperture size. volume 2, pages 935–938, 1987.
- [55] Karl F. Herzfeld and Theodore A. Litovitz. *Absorption and Dispersion of Ultrasonic Waves*. Academic Press, New York, 1959.
- [56] L. M. Hinkelman, D. Liu, L. A. Metlay, and R. C. Waag. Measurements of ultrasonic pulse arrival time and energy level variations produced by propagation through abdominal wall. *J. Acoust. Soc. Am.*, 95:530–541, 1994.
- [57] S. A. V. Holmes and H. N. Whitfield. The current status of lithotripsy. *British Journal of Urology*, 68(4):337–344, Oct 1991.
- [58] Danny Howard and Bradford Sturtevant. In vitro study of the mechanical effects of shock-wave lithotripsy. *Ultrasound in Medicine & Biology*, 23(7):1107–1122, 1997.
- [59] V. F. Humphrey. Nonlinear propagation in ultrasonic fields: Measurements, modelling, and harmonic imaging. *Ultrasonics*, 38:267–272, 2000.
- [60] J. A. Jensen. Field: A program for simulating ultrasound systems. *Med. Biol. Eng. Comp.*, col. 10th Nordic-Baltic Conference on Biomedical Imaging, 4(1):351–353, 1996.
- [61] J. A. Jensen and N. B. Svendsen. Calculation of pressure fields from arbitrarily shaped, apodized, and excited ultrasound transducers. *IEEE Trans. Ultrason., Ferroelec., Freq. Contr.*, 39(2):262–267, 1992.
- [62] J. E. Kennedy, G. R. ter Haar, and D. Cranston. High intensity focused ultrasound: surgery of the future? *Brit. J. Rad.*, 76:590–599, 2003.
- [63] VA Khokhlova, R Souchon, J Tavakkoli, OA Sapozhnikov, and D Cathignol. Numerical modeling of finite-amplitude sound beams: Shock formation in the near field of a cw plane piston source. *J. Acoust. Soc. Am.*, 110(1):95–108, 2001.

- [64] Vera A. Khokhlova and Oleg A. Sapozhnikov. Modification of the spectral method for describing nonlinear acoustic waves containing shocks. *J. Acoust. Soc. Am.*, 96(5):3321, 1994.
- [65] Lawrence Kinsler, Austin Frey, Alan Coppens, and James Sanders. *Fundamentals of Acoustics*. John Wiley and Sons, 2000.
- [66] Murray Kornbluth, David H. Liang, Allan Paloma, and Ingela Schnittger. Native tissue harmonic imaging improves endocardial border definition and visualization of cardiac structures. *Journal of the American Society of Echocardiography*, 11:693–701, July 1998.
- [67] V. P. Kuznetsov. Equations of nonlinear acoustics. *Soviet Physical Acoustics*, 16:467–470, 1971.
- [68] Yang-Sub Lee and Mark F. Hamilton. Time-domain modeling of pulsed finite-amplitude sound beams. *J. Acoust. Soc. Am.*, 97(2):906–917, February 1995.
- [69] Y. D. Li and J. A. Zagzebski. Computer model for harmonic ultrasound imaging. *IEEE Transactions on Ultrasonics Ferroelectrics and Frequency Control*, 47(5):1259–1272, Sep 2000.
- [70] Qing-Huo Liu and Jianping Tao. The perfectly matched layer for acoustic waves in absorbtive media. *J. Acoust. Soc. Am.*, 102(4):2072–2082, 1997.
- [71] T. Douglas Mast. Two- and three-dimensional simulations of ultrasonic propagation through human breast tissue. *Acoustics Research Letters Online*, 3(2):53–58, 2002.
- [72] T. Douglas Mast, Laura M. Hinkelman, Michael J. Orr, Victor W. Sparrow, and Robert C. Waag. Simulation of ultrasonic pulse propagation through the abdominal wall. *Journal of the Acoustical Society of America*, 102(2):1177–1190, Aug 1997.
- [73] Philip M. Morse and K. Uno Ingard. *Theoretical Acoustics*. Princeton University Press, 1986.
- [74] Sylvain Nacheff, Dominique Cathignol, Jacqueline Naze Tjøtta, Aina M. Berg, and Sigve Tjøtta. Investigation of a high intensity sound beam from a plane transducer. experimental and theoretical results. *J. Acoust. Soc. Am.*, 98(4):2303–2323, October 1995.
- [75] K. R. Nightingale, R. W. Nightingale, M. L. Palmeri, and G. E. Trahey. A finite element model of remote palpation of breast lesions using radiation force: Factors affecting tissue displacement. *Ultrasonic Imaging*, 22(1):35–54, 2000.

- [76] K. R. Nightingale, M. L. Palmeri, R. W. Nightingale, and G. E. Trahey. On the feasibility of remote palpation using acoustic radiation force. *J. Acoust. Soc. Am.*, 110(1):625–634, 2001.
- [77] K. R. Nightingale, M. S. Soo, R. W. Nightingale, and G. E. Trahey. Acoustic radiation force impulse imaging: In vivo demonstration of clinical feasibility. *Ultrasound Med. Biol.*, 28(2):227–235, 2002.
- [78] Kathryn Nightingale. *Ultrasonic generation and detection of acoustic streaming to differentiate between fluid-filled and solid lesions in the breast*. PhD thesis, Duke University, 1997.
- [79] W.L.M. Nyborg. *Acoustic Streaming*, volume IIB. Academic Press Inc, New York, 1965.
- [80] W.L.M. Nyborg. Solutions of the bio-heat transfer equation. *Phys. Med. Biol.*, 33:785–792, 1988.
- [81] M. O’Donnell. Quantitative ultrasonic backscatter measurements in the presence of phase distortion. 72(6):1719–1725, 1982.
- [82] M. L. Palmeri, K. D. Frinkley, and K. R. Nightingale. Experimental studies of the thermal effects associated with radiation force imaging of soft tissue. *Ultrasonic Imaging*, 26:100–114, 2004.
- [83] M. L. Palmeri, A. C. Sharma, R. R. Bouchard, R.W. Nightingale, and K.R. Nightingale. A finite-element method model of soft tissue response to impulsive acoustic radiation force. 52(10):1699–1712, 2005.
- [84] M.L. Palmeri, K.D. Frinkley, L. Zhai, R. Bentley, K. Ludwig, M. Gottfried, and K.R. Nightingale. Acoustic radiation force impulse imaging of the gastrointestinal tract. In *Proceedings of the 2004 IEEE Ultrasonics Symposium*, volume 1, pages 744–747, 2004.
- [85] Roger Peyret. *Spectral Methods for Incompressible Viscous Flow*. Springer-Verlag, 2000.
- [86] Allan D. Pierce. *Acoustics: An Introduction to Its Physical Principles and Applications*. Acoustical Society of America, 1989.
- [87] Gianmarco Pinton, Jeremy Dahl, Stephen Rosenzweig, and Gregg Trahey. A heterogeneous nonlinear attenuating full-wave model of ultrasound. *IEEE Trans. Ultrason., Ferroelec., Freq. Contr.*, 2007, (Submitted).
- [88] Gianmarco F. Pinton, Jeremy J. Dahl, and Gregg E. Trahey. Rapid tracking of small displacements in ultrasound. *IEEE Trans. Ultrason., Ferroelec., Freq. Contr.*, June 2006.

- [89] Gianmarco F. Pinton and Gregg E. Trahey. Numerical methods for axisymmetric and 3D nonlinear beams. *Proceedings of SPIE Medical Imaging 2005: Ultrasonic Imaging and Signal Processing*, 5750:388–396, April 2005.
- [90] Gianmarco F. Pinton and Gregg E. Trahey. Continuous delay estimation with polynomial splines. *IEEE Trans. Ultrason., Ferroelec., Freq. Contr., In Press*, 2006.
- [91] Gianmarco F. Pinton and Gregg E. Trahey. Numerical nonlinear ultrasonic imaging in heterogeneous media. *IEEE Trans. Ultrason., Ferroelec., Freq. Contr.*, 2007 (In Prepration).
- [92] Gianmarco F. Pinton and Gregg E. Trahey. Sources of image degradation in fundamental and harmonic ultrasound imaging. *IEEE Trans. Ultrason., Ferroelec., Freq. Contr.*, 2007 (In Prepration).
- [93] Gianmarco F. Pinton and Gregg E. Trahey. A comparison of time domain solutions for the full-wave equation and the parabolic wave equation for diagnostic ultrasound transducers. *IEEE Trans. Ultrason., Ferroelec., Freq. Contr.*, 2007 (In Press).
- [94] Gianmarco F. Pinton and Gregg E. Trahey. Numerical solutions of the khokhlov-zabolotskaya-kuznetsov equation satisfying the rankine-hugoniot condition. *Ultrasonic Imaging*, 2007 (In Press).
- [95] Gianmarco F. Pinton and Gregg E. Trahey. Numerical solution of the parabolic wave equation with cubic nonlinearity. *IEEE Trans. Ultrason., Ferroelec., Freq. Contr.*, 2007 (Submitted).
- [96] A. Sarvazyan, O. Rudenko, S. Swanson, J. Fowlkes, and S. Emelianov. Shear wave elasticity imaging: A new ultrasonic technology of medical diagnostics. 24(9):1419–1435, 1998.
- [97] A.C. Sharma, M.S. Soo, G.E. Trahey, and K.R. Nightingale. Acoustic radiation force impulse imaging of in vivo breast masses. In *Proceedings of the 2004 IEEE Ultrasonics Symposium*, volume 1, pages 728–731, 2004.
- [98] A. R. Skovoroda, S. Y. Emilanov, and M. O’Donnell. Tissue elasticity reconstruction based on ultrasonic displacement and strain images. *IEEE Trans. Ultrason., Ferroelect., Freq. Contr.*, 42:746–765, 1995.
- [99] K. T. Spencer, J. Bednarz, P. G. Rafter, C. Korcarz, and R. M. Lang. Use of harmonic imaging without echocardiographic contrast to improve two-dimensional image quality. *Am J Cardiol.*, 82(6):794–9, Sep 1998.

- [100] H.C. Starritt, F.A. Duck, and V.F. Humphrey. An experimental investigation of streaming in pulsed diagnostic ultrasound beams. *Ultrasound Med. Biol.*, 15:363–373, 1989.
- [101] P. R. Stepanishen. The time-dependent force and radiation impedance on a piston in a rigid infinite planar baffle. *J. Acoust. Soc. Am.*, 49(3):841–849, 1971.
- [102] P. R. Stepanishen. Transient radiation from pistons in a infinite planar baffle. *J. Acoust. Soc. Am.*, 49:1627–1638, 1971.
- [103] John C. Strickwerda. *Finite Difference Schemes and Partial Differential Equations*. Wadsworth and Brooks/Cole, 1989.
- [104] B. Surtevant. *Shock Wave Physics of Lithotripters*. In: *Smith AD. Smith's Textbook of Endourology*. Quality Medical Publishing, 2006.
- [105] Thomas L. Szabo. Time domain wave equations for lossy media obeying a frequency power law. *J. Acoust. Soc. Am.*, 96(1):491–500, 1994.
- [106] Thomas L. Szabo. *Diagnostic ultrasound imaging*. Elsevier Academic Press, 2004.
- [107] F. Tappert. The parabolic approximation method in wave propagation and underwater acoustics. *Lectures in Physics. J. B. Keller and J. S. Papadakis, New York: Springer*, pages 224–287, 1977.
- [108] J Tavakkoli, D Cathignol, R Souchon, and OA Sapozhnikov. Modeling of pulsed finite-amplitude focused sound beams in time domain. *J. Acoust. Soc. Am.*, 104(4):2061–2072, Oct 1998.
- [109] James A. TenCate. An experimental investigation of the nonlinear pressure field produced by a plane circular piston. *J. Acoust. Soc. Am.*, 94(2):1084–1089, Aug 1993.
- [110] James D. Thomas and David N. Rubin. Tissue harmonic imaging: Why does it work? *Journal of the American Society of Echocardiography*, 11(8):803–808, August 1998.
- [111] J. N. Tjøtta and S. Tjøtta. An analytical model for the nearfield of a baffled piston transducer. *J. Acoust. Soc. Am.*, 68:334–339, 1980.
- [112] J. N. Tjøtta and S. Tjøtta. Finite amplitude ultrasound beams. *Proceedings Ultrasonics Symposium*, 2:709–714, Nov 1994.
- [113] G. R. Torr. The acoustic radiation force. *Am. J. Phys.*, 52:402–408, 1984.

- [114] G. E. Trahey, P. D. Freiburger, L. F. Nock, and D. C. Sullivan. *In Vivo* measurements of ultrasonic beam distortion in the breast. 13(1):71–90, 1991.
- [115] J. A. Trangenstein. *Numerical Solution of Partial Differential Equations*. Cambridge University Press, In Press.
- [116] F. Tranquart, N. Grenier, V. Eder, and L. Pourcelot. Clinical use of ultrasound tissue harmonic imaging. *Ultrasound in Medicine and Biology*, 25(6):889–894, July 1999.
- [117] G. E. Topholme. Generation of acoustic pulses by baffled plane pistons. *Mathematika*, 16:209–224, 1969.
- [118] D. H. Turnbull and F. S. Foster. Simulation of b-scan images from two-dimensional transducer arrays: Part II - comparisons between linear and two-dimensional phased arrays. 14(4):344–353, 1992.
- [119] B. van Leer. Towards the ultimate conservative difference scheme, v. a second order sequel to godunov’s method. *J. Comp. Phys.*, 32(101-136), 1979.
- [120] T. Varslot and G Taraldsen. Computer simulation of forward wave propagation in soft tissue. *IEEE Transactions on Ultrasonics Ferroelectrics and Frequency Control*, 52(9):1473– 1482, Sep. 2005.
- [121] Trond Varslot, Svein-Erik Masoy, and Tonni F. Johansenand Bjorn Angelsen. Aberration in nonlinear acoustic wave propagation. *IEEE Transactions on Ultrasonics Ferroelectrics and Frequency Control*, 54(3):470–479, Mar. 2007.
- [122] A. Vogel and W. Lauterborn. Acoustic transient generation by laser-produced cavitation bubbles near solid boundaries. *J. Acoust. Soc. Am.*, 84(2):719–731, Aug 1988.
- [123] K. D. Wallace, B. S. Robinson, M. R. Holland, M. R. Rielly, and J. G. Miller. Experimental comparisons of the impact of abdominal wall aberrators on linear and nonlinear beam patterns. *2004 IEEE Ultrasonics Symposium*, 2:866– 869, Aug 2004.
- [124] Kirk D. Wallace, Mark R. Holland, and James G. Mille. Improved description of shock wave evolution in media with frequency power law dependent attenuation. *J. Acoust. Soc. Am.*, 109(5):2263–2265, 2001.
- [125] Kendall R. Waters, Michael S. Hughes, Joel Mobley, Gary H. Brandenburger, and James G. Miller. On the applicability of kramers-krnig relations for ultrasonic attenuation obeying a frequency power law. *J. Acoust. Soc. Am.*, 108(2):556–563.

- [126] P. N. T. Wells. *Biomedical Ultrasonics*. Academic Press Inc., New York, New York, 1 edition, 1977.
- [127] P. J. Westervelt. Parametric acoustic array. *J. Acoust. Soc. Am.*, 35:535–537, 1963.
- [128] G. B. Whitham. *Linear and nonlinear waves*. Wiley-Interscience Series of Texts, Monographs and Tracts, 1974.
- [129] X. C. Xu, F. Mao, X. F. Gong, and D. Zhang. Theoretical calculation and experimental study on the third-order nonlinearity parameter c/a for organic liquids and biological fluids. *J. Acoust. Soc. Am.*, 113(3):1743–1748, Mar 2003.
- [130] Xinmai Yang and Robin O. Cleveland. Time domain simulation of nonlinear acoustic beams generated by rectangular pistons with application to harmonic imaging. *J. Acoust. Soc. Am.*, 117(1):113–123, 2005.
- [131] E. A. Zabolotskaya and R. V. Khokhlov. Quasi-plane waves in the nonlinear acoustics of confined beams. *Soviet Physical Acoustics*, 15:35–40, 1969.
- [132] R. J. Zemp, J. Tavakkoli, and R. Cobbold. Modeling of nonlinear ultrasound propagation in tissue from array transducers. *J. Acoust. Soc. Am.*, 113(1):139–152, Jan 2003.
- [133] Pei Zhong, Iulian Cioanta, Franklin H. Cocks, and Glenn M. Preminger. Inertial cavitation and associated acoustic emission produced during electrohydraulic shock wave lithotripsy. *J. Acoust. Soc. Am.*, 101(5):2940–2950, 1997.
- [134] Y. Zhou and P. Zhong. The effect of reflector geometry on the acoustic field and bubble dynamics produced by an electrohydraulic shock wave lithotripter. *J. Acoust. Soc. Am.*, 119(6):3625–3636, June 2006.
- [135] Q. Zhu and B. D. Steinberg. Large-transducer measurements of wavefront distortion in the female breast. *J. Acoust. Soc. Am.*, 14(3):276–299, 1992.
- [136] S. Zhu, F. H. Cocks, Glenn M. Preminger, and Pei Zhong. The role of stress waves and cavitation in stone comminution in shock wave lithotripsy. *Ultrasound in Medicine and Biology*, 28(5):661–671, 2002.

Biography

Gianmarco Francesco Pinton

Date of Birth: November 19, 1979

Place of Birth: Milan, Italy

Graduate Education *Duke University*, Durham, NC.

Ph.D. in Biomedical Engineering, 2007.

Dissertation topic: “Numerical modeling of nonlinear wave propagation in ultrasound.”

Advisor: Gregg E. Trahey, Ph.D. (Biomedical Engineering)

M.Phil. in Mathematics, 2007.

Topics: Scientific Computing, Ordinary Differential Equations

Advisor: John Trangenstein, Ph.D. (Mathematics)

Undergraduate Education *Duke University*, Durham, NC.

May 2001 (with distinction)

B.S.E. in Biomedical Engineering

Thesis topic: “Three-dimensional motion tracking in volumetric ultrasound”

B.S. in Physics

Minor in Mathematics

Refereed Publications

[1] **Gianmarco Pinton**, Jeremy Dahl, and Gregg Trahey, “Numerical nonlinear ultrasonic imaging in heterogeneous media.,” *IEEE Trans. Ultrason. Ferroelectr. Freq. Control*. (*In preparation*)

[2] **Gianmarco Pinton**, Mark Palmeri, and Gregg Trahey, “Effects of nonlinear propagation on acoustic radiation force in ultrasound.,” *IEEE Trans. Ultrason. Ferroelectr. Freq. Control*. (*In preparation*)

[3] **Gianmarco Pinton** and Gregg Trahey, “Sources of image degradation in fundamental and harmonic ultrasound imaging.,” *J. Acoust. Soc. Am.* (*In preparation*)

[4] **Gianmarco Pinton** and Gregg Trahey, “Numerical solution of the parabolic wave equation with cubic nonlinearity.,” *IEEE Trans. Ultrason. Ferroelectr. Freq. Control*. (*Submitted, 2007*)

[5] **Gianmarco Pinton**, Jeremy Dahl, and Gregg Trahey, “Full-wave modeling of finite-amplitude waves in diagnostic ultrasound.,” *IEEE Trans. Ultrason. Ferroelectr. Freq. Control.* (Submitted, 2007)

[6] **Gianmarco Pinton** and Gregg Trahey, “Numerical methods satisfying the Rankine-Hugoniot condition for the KZK equation.,” *Ultrasonic Imaging (In Press, 2007)*.

[7] **Gianmarco Pinton** and Gregg Trahey, “A comparison of time domain solutions for the full-wave equation and the parabolic wave equation for diagnostic ultrasound transducers.,” *IEEE Trans. Ultrason. Ferroelectr. Freq. Control.* (In Press, 2007)

[8] Jeremy Dahl, **Gianmarco Pinton**, Mark Palmeri, Vineet Agrawal, Kathy Nightingale, and Gregg Trahey, “A Parallel Tracking Method for Acoustic Radiation Force Impulse Imaging.,” *IEEE Trans. Ultrason. Ferroelectr. Freq. Control.* Volume 54, Issue 2, February 2007 Pages:301 - 312

[9] Jeremy Dahl, Stephen McAleavey, **Gianmarco Pinton**, Mary-Scott Soo, and Gregg Trahey, “Adaptive Imaging on a Diagnostic Ultrasound Scanner at Quasi Real-Time Rates.,” *IEEE Trans. Ultrason. Ferroelectr. Freq. Control.* Volume 53, Issue 10, October 2006 Page(s):1832 - 1843.

[10] **Gianmarco Pinton** and Gregg Trahey, “Continuous delay estimation with polynomial splines.,” *IEEE Trans. Ultrason. Ferroelectr. Freq. Control.* Volume 53, Issue 11, November 2006 Pages:2026 - 2035.

[11] **Gianmarco Pinton**, Jeremy Dahl, and Gregg Trahey, “Rapid tracking of small displacements with ultrasound.,” *IEEE Trans. Ultrason. Ferroelectr. Freq. Control.* Volume 53, Issue 6, June 2006 Page(s):1103 - 1117.

Conference Presentations

[1] **Gianmarco Pinton**, Mark Palmeri and Gregg Trahey, “Effects of nonlinear propagation on acoustic radiation force in ultrasound.,” *International Conference on the Ultrasonic Measurement and Imaging of Tissue Elasticity*, 2007.

[2] **Gianmarco Pinton** and Gregg Trahey, “Cubic nonlinearity in the thermoviscous paraxial wave equation.,” *IEEE Symposium on Ultrasonics*, 2007.

[3] **Gianmarco Pinton** and Gregg Trahey, “Full-wave simulation of finite-amplitude ultrasound in heterogenous media.,” *IEEE Symposium on Ultrasonics*, 2007.

- [4] **Gianmarco Pinton** and Gregg Trahey, “Clutter from multiple scattering and aberration in a nonlinear medium.,” *IEEE Symposium on Ultrasonics*, 2007.
- [5] Kathy Nightingale, Brian Fahey, Stephen Hsu, Kristin Frinkley, Jeremy Dahl, Mark Palmeri, Liang Zhai, **Gianmarco Pinton**, Gregg Trahey “On the potential for guidance of ablation therapy using acoustic radiation force impulse imaging” *Biomedical Imaging: From Nano to Macro*, 2007. ISBI 2007. 4th IEEE International Symposium on April 2007 Page(s):1116 - 1119
- [6] **Gianmarco Pinton** and Gregg Trahey, “Numerical solutions of the KZK equation satisfying the Rankine-Hugoniot condition.,” *Meeting of the Acoustical Society of America*, 2006
- [7] **Gianmarco Pinton** and Gregg Trahey, “Continuous delay estimation with polynomial splines.,” *Meeting of the Acoustical Society of America*, 2006
- [8] **Gianmarco Pinton** and Gregg Trahey, “Shock Wave Propagation with the KZK Equation.,” *IEEE Symposium on Ultrasonics*, 2006.
- [9] **Gianmarco Pinton** and Gregg Trahey, “Continuous Delay Estimation with Polynomial Splines.,” *IEEE Symposium on Ultrasonics*, 2006.
- [10] Matt Fronheiser, Jeremy Dahl, **Gianmarco Pinton**, Zubair Chao, and Stephen Smith, “3D Acoustic Radiation Force Impulse (ARFI) Imaging using a 2D Matrix Array.,” *IEEE Symposium on Ultrasonics*, 2006.
- [11] **Gianmarco Pinton** and Gregg Trahey, “Numerical methods for axisymmetric and 3D nonlinear beams.,” *IEEE Symposium on Ultrasonics*, 2005.
- [12] **Gianmarco Pinton** and Gregg Trahey, “Rapid tracking of small displacements using ultrasound.,” *IEEE Symposium on Ultrasonics*, 2005.
- [13] **Gianmarco Pinton**, Stephen McAleavey, Jeremy Dahl, Kathryn Nightingale, and Gregg E. Trahey, “Real-time acoustic radiation force impulse imaging.,” *SPIE Medical Imaging 2005*.
- [14] **Gianmarco Pinton** and Gregg Trahey, “Numerical methods for axisymmetric and 3D nonlinear beams.,” *SPIE Medical Imaging*, 2005.
- [15] Stephen Hsu, Patrick Wolf, Brian Fahey, **Gianmarco Pinton**, Douglas Dumont and Gregg Trahey, “In vivo acoustic radiation force impulse imaging of cardiac

ablations.,” *IEEE Symposium on Ultrasonics*, 2005.

[16] Stephen McAleavey, Jeremy Dahl, Mary-Scott Soo, **Gianmarco Pinton** and Gregg Trahey, “Resolution improvement of point targets by real-time phase aberration correction: in vivo results.,” *IEEE Symposium on Ultrasonics*, 2004.

[17] Stephen McAleavey, Jeremy Dahl, **Gianmarco Pinton** and Gregg E. Trahey, “Real time adaptive imaging with 1.75D, high frequency arrays.,” *IEEE Symposium on Ultrasonics*, 2003.

[18] **Gianmarco Pinton**, Mark Palmeri, Stephen McAleavey, Kathy Nightingale, and Gregg Trahey, “ARFI imaging of the cardiovascular system.,” *IEEE Symposium on Ultrasonics*, 2003.